Formation of Planetary Atmospheres

Signatures of amorphous water ice delivery

Renger Dotinga

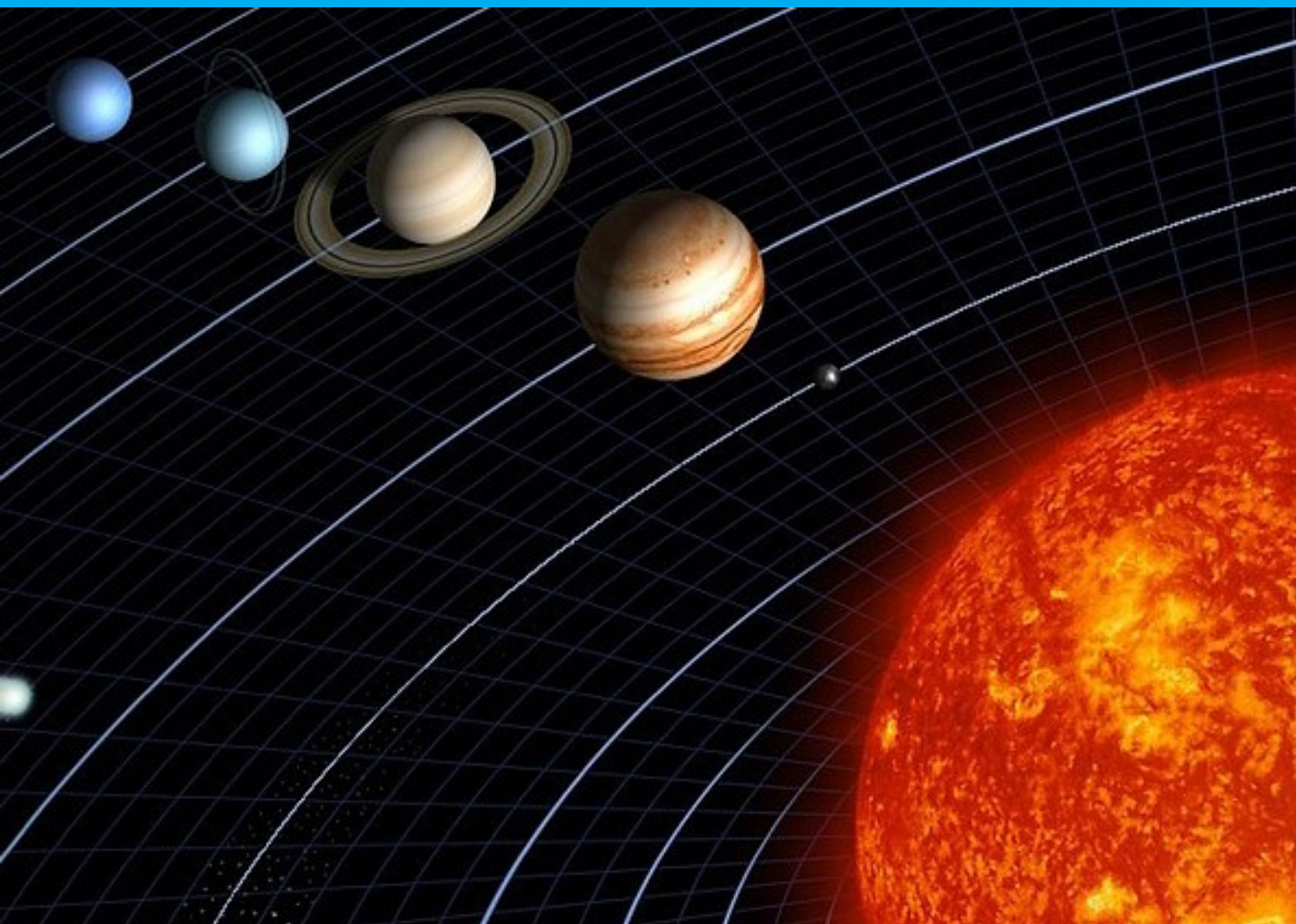

Formation of Planetary Atmospheres

Signatures of amorphous water ice delivery

by

Renger Dotinga

to obtain the degree of Master of Science
at the Delft University of Technology,
to be defended publicly on Friday September 25, 2020 at 14:00.

Student number:	4287983	
Project duration:	February 1, 2020 – September 25, 2020	
Thesis committee:	Prof. Dr. L. L. A. Vermeersen,	TU Delft, chairman
	Dr. S. Cazaux,	TU Delft, supervisor
	Prof. F. Dulieu,	Cergy-Pontoise University
	Dr. A. Menicucci,	TU Delft

This thesis is confidential and cannot be made public until September 25, 2021.

Preface

With this thesis I end my time at the Delft University of Technology. It was perhaps inevitable that I complete this journey studying the planets that fascinated me as a young boy. I can only humbly thank my parents for providing me with the encouragement, safety, and freedom to pursue this and my other endeavours.

This report would not have been possible without my supervisor, Dr. Stephanie Cazaux. Her true passion for the field of planetary science, combined with a down-to-Earth mentality, made this project an enjoyable conclusion of my student years. In addition, I extend my gratitude to Prof. Francois Dulieu of the University Cergy-Pontoise, whose insights provided valuable guidance. It is a shame the laboratory work we initially envisaged could not be conducted.

For those that come accross this report for professional reasons, I hope this work contributes a piece of the grand puzzle that is the history of our Sun, neighbour planets, and own Earth. For those that are simply passing by, I hope that reading this report will have you looking up at the next night sky in awe. That sense of wonder is, after all, all that sets us apart from regular stardust.

Renger Dotinga

Delft, September 2020

Summary

The delivery of enriched icy grains has been proposed as a mechanism to explain the enrichment of Jupiter with noble gases measured by the Galileo mission. The enrichment with noble gases imposes constraints on the formation temperature of these grains, with some species only adsorbing to amorphous ice at temperatures below 30K. While significant consideration has been given to the formation conditions of the ices, the release of species as the grain migrates inward toward the forming planets has been given less thought. The desorption of the noble gases Ar, Kr and Xe trapped in amorphous ice occurs largely below 80K, while Jupiter formed at a temperature of 130K. The composition of the icy grains thus changes from formation to deposition.

The accretion and subsequent desorption of noble gas species alongside water into an enriched icy grain has been simulated using a Monte Carlo model. Particles are deposited onto a predefined grid at temperatures sufficiently low to retain Ar. The temperature is subsequently increased up to 150K, capturing the temperature range relevant for giant planet formation. Previously reported experimental measurements of desorption rates are used to benchmark the model and constrain the diffusion and desorption rates of each noble gas species. The desorption of each species from the ice is tracked during heating, and used to compute the temperature-dependent enrichment profile of the grain.

Our simulations show that the composition of an amorphous water ice is dependent on the formation temperature of the ice. For temperatures below 25K, the ratios Ar/Kr and Ar/Xe are equal to the ratio of their accretion rates. As the formation temperature increases, Ar begins to desorb during formation. Both ratios thus decrease as the formation temperature increases between 25K and 30K. As the ice is heated after formation to 130K, the noble gas species are observed to desorb from the ice. This desorption occurs mostly from the top layers of the ice; the effect of desorption on the ice composition is thus less for thicker ices.

In our simulations, the final composition at 130K of the ice in terms of Ar:Kr:Xe is comparable to the composition at formation. However, the temperatures at which the desorption of each species peaks differs, as was also observed in previous experimental work. Ar is the most volatile species and readily desorbs between 30K to 50K. Kr and Xe are less volatile and largely remain in the ice in this temperature range. The Ar/Kr ratio and, more notably, the Ar/Xe ratio thus show a dip at 50K.

Our simulations show that the delivery of amorphous water ice, under different formation conditions, could have provided the observed noble gas enrichment ratios of Jupiter. Similar Ar/Kr and Ar/Xe ratios are expected to be observed on Saturn and Uranus, which were located at temperatures of $\sim$ 95K and $\sim$ 70K respectively. If the enrichment was delivered in amorphous water ices with thickness $<$ 100Å, an Ar/Xe atmospheric signature lower than the one observed on Jupiter is expected for Neptune, which was located at a temperature of 50K. This finding can be considered during the interpretation of future probe measurements of the ice giant planets, and Neptune in particular. If the Ar/Xe ratio is measured to be lower than on Jupiter, the delivery of enriched amorphous ice is a very possible scenario for the delivery of noble gases in gas giants planets.

Contents

Summary v

List of Figures ix

List of Tables xiii

1 Introduction 1

2 Scientific Background 3
- 2.1 Origin of the solar system . . . 3
  - 2.1.1 From a molecular cloud to a stable planetary system . . . 3
  - 2.1.2 The Galileo Mission: Jupiter's enrichment . . . 6
- 2.2 Enrichment mechanisms . . . 8
  - 2.2.1 Water ice as a species carrier . . . 8
  - 2.2.2 Amorphous solid water . . . 8
  - 2.2.3 The budget of water vapour . . . 10
- 2.3 Enrichment of amorphous water ice . . . 12
  - 2.3.1 Porosity . . . 13
  - 2.3.2 Release of trapped species . . . 13
- 2.4 Knowledge gap . . . 15

3 Laboratory Data 17
- 3.1 Introduction . . . 17
- 3.2 Pure noble gas ice . . . 17
- 3.3 Codeposited Ar and H_2O . . . 18
- 3.4 Codeposited Kr and H_2O . . . 19

4 Monte Carlo Approach 21
- 4.1 Methodology . . . 21
  - 4.1.1 Processes in ice formation . . . 21
  - 4.1.2 Simulation parameters . . . 24
  - 4.1.3 Movement on the grid . . . 25
- 4.2 Validation . . . 26
  - 4.2.1 Parameters study . . . 27
  - 4.2.2 Desorption mechanics . . . 30
- 4.3 Summary . . . 34

5 Astrophysical Application 35
- 5.1 Introduction . . . 35
- 5.2 Simulation parameters . . . 35
  - 5.2.1 Ice thickness . . . 35
  - 5.2.2 Species ratios . . . 37
  - 5.2.3 Temperature conditions . . . 37

5.3 Results . . . 38
5.4 Extension to solar system conditions . . . 42
5.4.1 Heating rate . . . 42
5.4.2 Ice thickness . . . 44
5.4.3 Jupiter . . . 47
5.4.4 Saturn, Uranus and Neptune . . . 50
5.5 Contribution to body of knowledge . . . 51
5.6 Summary . . . 53

6 Recommendations 55
6.1 Introduction . . . 55
6.2 Limitations . . . 55
6.3 Future work . . . 56
6.3.1 Experimental approach . . . 56
6.3.2 Inclusion of CO . . . 57
6.3.3 Isotopic differentiation of noble gases . . . 58

7 Conclusions 61

Bibliography 63

List of Figures

2.1 Visualisation of the phases of star formation. Clockwise from top left: (1) initial molecular cloud, (2) formation of a denser cloud, (3) collapse of the cloud and initial fusion, (4) primitive star with protoplanetary disk, (5) stable planetary system. Source: Bill Saxton, NRAO/AUI/NSF 4
2.2 Overview of dynamics and forces acting on the protoplanetary disk [1]. The snow line indicates the region outside of which ices can form. 5
2.3 Enrichment of Jupiter with noble gases. Enrichment is computed as molar abundance of the species to the molar abundance of H, divided by the same molar abundance ratio in the Sun [2]. 8
2.4 Phase diagram of H_2O. The amorphous to crystalline transition temperature shown in purple has been added to the original [3]. 10
2.5 Relevant conditions in the protoplanetary disk. From top to bottom: Temperature, H_2O vapour concentration, H_2O ice concentration. Concentrations are expressed relative to H [4]. 11
2.6 Different regimes of argon desorption from amorphous water ice. The H_2O flux at $\sim$30K is loosely bound water molecules evaporating with the frozen Ar. The last peak (g) corresponds to the remaining trapped Ar released only when the water ice itself desorbs [5]. 14
2.7 Visualisation of the mono- and multilayers of noble gas on amorphous water ice. 15
2.8 Overview of the amorphous ice delivery mechanism proposed to explain Jupiter's noble gas enrichment. 16

3.1 TPD of Ar, Kr and Xe deposited on a sample of amorphous water ice [6]. . . . 18
3.2 TPD of Ar codeposited with H_2O [5]. 19
3.3 Experimental TPD of codeposited Kr and H_2O. 20

4.1 The two-phase process simulated numerically, showing water (blue) and noble gas atoms (orange). The composition of the gas reservoir as depicted remains constant during the accretion phase. The key processes of accretion (1), diffusion (2) and desorption (3) are indicated. 22
4.2 Energy barrier that must be overcome for diffusion both if the initial energy is higher (left panel) or lower (right panel) than the final energy. 23
4.3 Visual representation of the lattice onto which molecules adsorb. In the left panel a unit cell is displayed, along with the relevant lengths used to compute e.g. the surface area and volume of pores. In the right panel the four possible directions of diffusion are shown [7]. 24
4.4 Flow-chart of how the model determines the next event. 26

4.5 Output of the Monte Carlo model under the variation of different parameters: diffusion parameter α (top row), deposition temperature T_d (second row), H_2O:CH_4 ratio (third row), heating rate h (fourth row) and grid size g (bottom row). The flux of evaporating methane molecules (left panels) from the ice and the area to volume ratio (right panels) of the remaining ice is presented for each set of simulations. All simulations used a Δt of 10s. The standard simulation, indicated in violet on each figure, has a $\alpha = 0.4$, $T_d = 10$K, $r = 10:1$, $h = 6$K min^{-1}, and $g = 60$. The dashed grey lines indicate the expected multilayer and monolayer desorption peaks at 35K and 45K respectively. . . . 28
4.6 Different regimes of argon release from amorphous water ice. Original figure by Bar-Nun et al. [5] relabelled for the purpose of this study. . . . 32
4.7 Desorption of Ar from amorphous water ice, accreted from an evenly mixed gas, heated at 3K min^{-1}. The regimes in order of appearance are marked with A, B and C. . . . 32
4.8 Experimental TPD of codeposited Kr and H_2O, with labelled monolayer (B) and codesorption (D) regimes. . . . 33
4.9 TPD of codeposited Kr and H_2O, with labelled monolayer (B) and codesorption (D) regimes. . . . 33

5.1 Evolution of the noble gas ratios as different ice samples are heated. Each row shows the results of adjusting one input parameter, as listed in Table 5.2. Top row: formation temperature [K], second row: water to noble gas ratio r, third row: heating rate h [K min^{-1}]. . . . 39
5.2 Noble gas ratios upon formation, at 50K (approximate temperature of Neptune formation) and at 130K (approximate temperature of Jupiter formation) for different ice formation temperatures. The values measured by Galileo on Jupiter is shown as a dotted line. . . . 40
5.3 Evaluation of the effect of the heating rate h in K min^{-1} on the number of particles desorbed in the creeping regime c. . . . 43
5.4 Different cases of particle size and ice thickness 44
5.5 Fraction of Ar desorbed F as a function of the numbers of layers n, fitted with a least-squares fit. . . . 45
5.6 Noble gas ratios at 50K for the simulated 75Å ice (red line). The initial composition is shown by the blue line. The composition of thicker ices at 50K is extrapolated and shown with dashed lines. The values measured by Galileo on Jupiter is shown as a dotted line. . . . 46
5.7 Evolution of the Ar/Kr (top) and Ar/Xe (bottom) ratio during heating of an ice formed at 25K (red line) and 27K (blue line). The formation temperatures of Neptune, Uranus, Saturn and Jupiter are indicated. The Galileo probe measurement at Jupiter is circled in green. . . . 49
5.8 Evolution of the Ar/Xe ratio during heating of an ice formed at 25K (red line) and 27K (blue line). The evolution is compared to the initial ratio, shown as a dashed line. The grey arrows indicate the dampening of the features as the ice thickness is increased. . . . 51
5.9 Enrichment patterns expected for different delivery mechanisms. Original figure by Atreya et al. [8]; purple enrichment pattern has been added based on the findings of this work. . . . 52

6.1 Schematic of the FORMOLISM apparatus [9]. 57
6.2 Isotopic composition of different solar system bodies [10]. The purple arrow has been added to the original by Rubin et al. 59

List of Tables

2.1 Gas-phase abundancies of several elements and compounds [11]. Abundances are expressed in terms of H_2, the most abundant molecule in the solar nebula [12]. 7
2.2 Overview of enrichment mechanisms involving water ice. 9

4.1 Desorption energies used to model the noble gas-water interaction. 25
4.2 Desorption energies and ranges considered for the noble gas-water interaction. 27
4.3 List of simulations conducted to verify the influence of different model parameters. 27

5.1 Values used to derive the ice thickness. 36
5.2 List of simulations conducted to study planetary enrichment signatures. . . . 41
5.3 Computed mass (in $m_\oplus$) of icy material needed for the observed Jupiter enrichment, for different water abundances and average ice thicknesses, in $m_\oplus$. 50

1

Introduction

The Galileo mission to Jupiter delivered vast insight into the solar system's second largest body and largest planet. Together with the later Cassini mission, it provided perhaps the largest contribution to the current understanding of the origin of the gas giant planets. The formation of the solar system from an initial nebular cloud remains an active field of scientific research. Measurement of Jupiter's composition showed several notable deviations from the Sun's composition, despite both bodies having formed from the same nebular cloud. The measurement of interest which will be studied in this work is the enrichment of Jupiter with the noble gases argon (Ar), krypton (Kr) and xenon (Xe). The abundance of these noble gases in Jupiter's atmosphere is a factor 3 higher than the abundance measured in the Sun. This enrichment, both by this factor 3 and its approximate uniformity across the different species, is an active field of study which will be addressed in this work.

Various mechanisms have been proposed for accounting for the delivery of enriched material to Jupiter as it was forming in the protoplanetary disk. Such mechanisms are all dependent on density, temperature, and pressure conditions throughout the protoplanetary disk. This, in combination with the long time scales of planetary formation, complicate the translation of experimental results to theoretical models. The processes which form and alter the composition of material in the disk are an interplay of the accretion of matter, the movement of matter and angular momentum through the disk, and the sublimation behaviour of different species. In this work, the mechanism studied is the accretion of the noble gases in amorphous water ice. This ice would have formed on small dust grains in distant, cold regions of the solar systems. As the ices drifted inward towards the planets due to gas drag and collisions, their temperature would have increased.

A near-uniform enrichment suggests that the noble gases were captured in their initial proportions, but more readily than the lighter elements relative to which their abundance is measured. In addition, these ratios would have to be preserved over any subsequent heating. Given the different volatility of the noble gases this may impose constraints on the ice formation conditions. These constraints are in turn dependent on the formation conditions of the amorphous ice, namely the abundance of water vapour available for freezing. This work seeks to refine the current constraints imposed on the contribution of amorphous water ices to Jupiter's composition, by testing the preservation of noble gas enrichment uniformity under different formation and heating conditions.

This report is structured as follows. Chapter 2 provides the current relevant state of the art on the research theme of planetary formation. The formation scenarios of gas giants

from an initial disk of grains and gas are presented. The enrichment of Jupiter with noble gases, based on the measurements of the Galileo mission, is also presented here. The role of amorphous water ice as a possible mechanism for this enrichment is then discussed. In Chapter 3, previous laboratory measurements of species desorbing from amorphous water ice are presented. These laboratory measurements provide insights into the conditions at which different species are trapped in, and released from, amorphous water ice. In Chapter 4, a model for simulating the formation and desorption of enriched amorphous water ice is introduced. The effectiveness of the model is benchmarked by reproducing the previously presented laboratory results. In Chapter 5, the model is applied to the topic of the enrichment of the gas giant planets. Mixtures of water and noble gas are simulated. The ices are first formed at low temperatures, and then heated to replicate the heating which the grains would undergo during their inward drift. The composition of the ice during this heating process is tracked. The astrophysical implications of these results are then discussed. Chapter 6 is a thorough reflection of the conducted work. Consideration is given to the limitations of the numerical approach used. Recommendations for future study are then provided. The report is concluded in Chapter 7.

2

Scientific Background

This study investigates how the delivery of amorphous water ice could have contributed to a uniform noble gas enrichment of Jupiter. This chapter will provide relevant background knowledge on the topics of solar system formation from a molecular cloud, different enrichment mechanisms, and amorphous water ice. Section 2.1 is dedicated to our understanding of the solar system formation process from a molecular cloud. NASA's Galileo mission contributed significantly to our understanding of this formation process. The section includes the results of this mission's probe mass spectrometer study of Jupiter; specifically the uniform enrichment of the planet with the noble gases argon (Ar), krypton (Kr) and xenon (Xe) compared to the Sun's composition. Since the Sun and planets formed from the same molecular cloud, this enrichment provides a significant reference point for models of planetary formation. Section 2.2 presents the various mechanisms through which water ice could have contributed to this noble gas enrichment of Jupiter. Water ice forming in the cold outer regions of the solar system is believed to have carried noble gases and other volatiles inward, while leaving lighter species such as hydrogen and helium behind. The conditions under which an ice formed affects the ability of the ice to trap these species. The amount of water vapour available for condensation is another determinant of how much noble gas can be captured, and in what proportion. An overview of the constraints imposed by each of these mechanisms on planetary atmosphere composition is presented here. Section 2.3 is devoted to amorphous water ice. Experimental measurements of different species desorbing from ice deposited at low temperatures are discussed. The different noble gases desorb from amorphous water ice at different temperatures, constraining the conditions in which a uniform enrichment is preserved. In the summary of this chapter, Section 2.4, the knowledge gap in our current understanding of this noble gas enrichment is presented. More specifically, the temperature and water abundance constraints which will be tested and refined in this report are described in detail. The research questions to be addressed in this work are defined to conclude the chapter.

2.1. Origin of the solar system

2.1.1. From a molecular cloud to a stable planetary system

The Sun like other stars is believed to have formed in a molecular cloud, a relatively dense region in a galaxy consisting mostly of helium and hydrogen gas [13]. Observation of the

Milky Way galaxy has revealed many such molecular clouds [14]. These clouds are typically stable; the inward force of gravity and pressure from gases in the interstellar medium is balanced by the internal pressure. However, a region of the molecular cloud could be triggered into a collapse. There are broadly two scenarios in which a molecular cloud will collapse due to self-gravity. The first is the case in which the physical conditions in the cloud, such as a low temperature or high density, are such that there is enough gravitational energy in the cloud to induce a collapse. The second possibility is that the cloud is stable but disturbed by a nearby event such as a passing or exploding star [15]. Such an event could cause temporary pressure or temperature variations in the cloud, large enough to destabilise the cloud and trigger a collapse. The star system formation process is visualised in Figure 2.1, starting with an initial molecular cloud (1). As a portion of the molecular cloud collapses (2), the gravitational energy stored is converted into kinetic energy. As collisions become more frequent in the core, kinetic energy is converted into thermal energy. The formation of a dense envelope prevents this thermal energy from being radiated away, causing temperatures in the core to rise (3). When a temperature of the order of 10^6 K is reached nuclear reactions start. If there is sufficient further mass to accrete, the star will eventually begin to fuse hydrogen. If the star is stable, the high temperatures generate enough internal pressure to counteract the inward gravity of the star. The cloud matter which is not drawn into the star forms a disk around the protostar (4). Accretion of grains and planetesimals can eventually form planets (5). It should be noted that not all of the collapsing cloud collapses

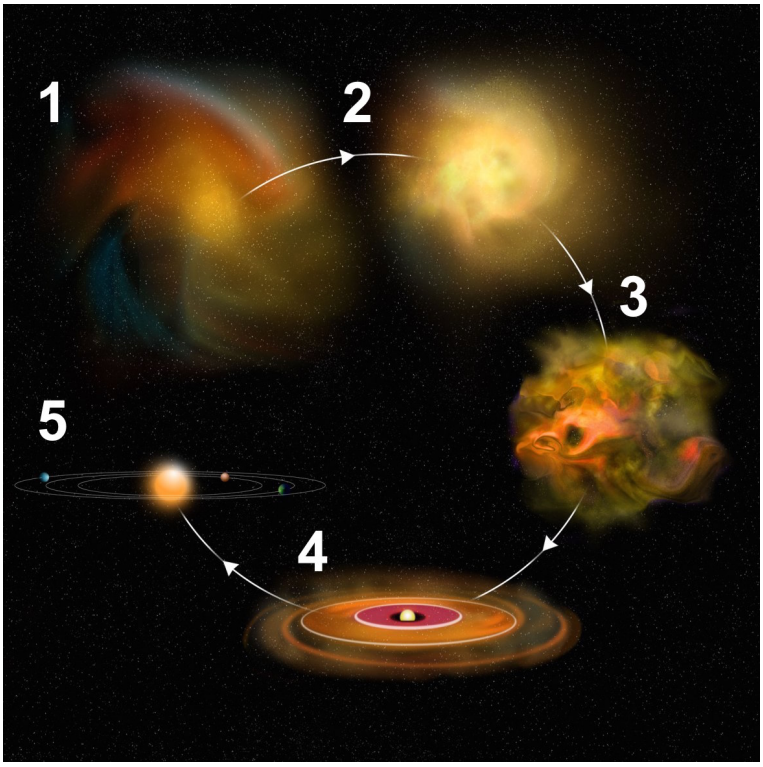

Figure 2.1: Visualisation of the phases of star formation. Clockwise from top left: (1) initial molecular cloud, (2) formation of a denser cloud, (3) collapse of the cloud and initial fusion, (4) primitive star with protoplanetary disk, (5) stable planetary system. Source: Bill Saxton, NRAO/AUI/NSF

.

to a star. In a single molecular cloud, local collapses occur and a single molecular cloud

can thus produce more than one star. When a collapse occurs, only around 8% of the initial collapsing cloud mass will end up as stellar mass [16]. This is partly due to the conservation of angular momentum, which would be violated if the outer particles of the cloud would collapse into a 'slowly' rotating star. This physical law explains why most primitive stellar systems also contain a disk of material around their star, holding the majority of the angular momentum in the system. This disk is shown in phase 4 of Figure 2.1 and is referred to as the protoplanetary disk.

The particles in the inner regions of the protoplanetary disk have relatively little angular momentum and will accrete towards the star core, but particles on the edge are restricted by the outward centrifugal force [17]. Particles falling towards the equatorial plane of the disk are met by particles from the other direction, causing dissipation of velocity in the direction perpendicular to the equatorial plane, as indicated by the dust settling in Figure 2.2. Figure 2.2 displays the dynamic processes and materials present in the protoplanetary disk [1]. A snowline marks the midplane radius at which a species freezes out from the gas phase into solid ice form. The snow line for water around 150K is shown in this figure. Below this temperature, water vapour condenses, potentially trapping noble gases and volatiles in the process. It is noted that the location of the snowline, in terms of radial distance, changes as the disk evolves.

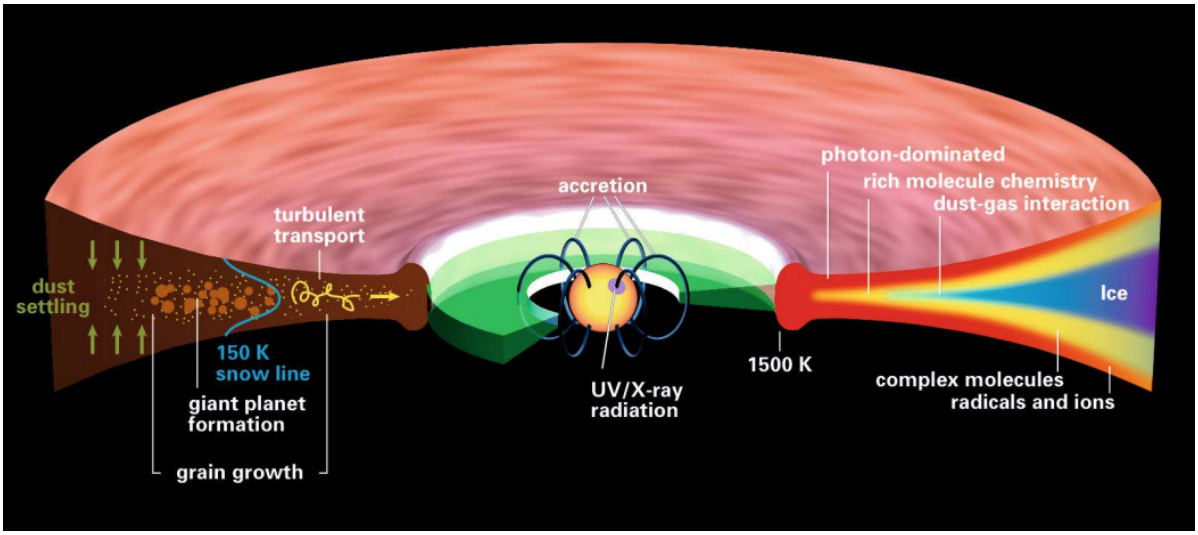

Figure 2.2: Overview of dynamics and forces acting on the protoplanetary disk [1]. The snow line indicates the region outside of which ices can form.

The formation of planets from this protoplanetary disk could have occurred in a number of ways. The widely accepted hypothesis is the core accretion model, which suggests the gas giants started out similar to the terrestrial planets: through the accretion of solid planetesimals. In the core accretion scenario [18], planets form by attracting a gaseous envelope onto a core of rock and ice. This theory is supported by the large amount of heavy elements found in the giant planets in our solar system [19]. The condensation of gas into microscopic dust particles is the first step towards the formation of planets. Interactions between the grains and their environment can affect their orbital parameters. The microscopic grains are most influenced by the following three forces:

1. **Drag** from the surrounding gas cloud. This is both in the direction of motion as well as due to inward falling gases [20].

2. **Gravity** from the Sun and nearby grains. Gravity of bodies other than the Sun become more relevant as planetesimals begin to gain mass [21].

3. **Mechanical** forces due to collisions with other planetesimals.

These forces drive and perturb the motion of the grains, and on long time scales lead to collisions between them. If after a collision the grains are close enough to be captured by their gravity fields, they will combine to form a larger body. This process is called accretion. The accretion process sees microscopic grains coalesce into objects on the kilometre scale. Bodies that have accumulated sufficient mass, typically at a size of $\sim 10^3$ km [22] will clear their orbital path of matter. The paths of these planetary embryos are not stable on longer times scales [15]. The infall of material during this phase drags the body inward and the possible intersection of planetary orbits make gravity interactions more relevant.

As the rocky and icy cores became massive enough they started to capture the nearby gas in the nebula, further increasing the mass and increasing the temperature of the core. Jupiter and Saturn are both believed to have captured a large amount of gas during this phase. The ice giants Uranus and Neptune are envisioned to remain smaller, because the protoplanetary gas disk dissipates while the gas envelopes are growing [18]. The dissipation of the gases of the protoplanetary disk in a relatively short time constrains the period of this enveloping phase [23]. During the heating of the core noble gases which were trapped in the solid ice planetesimals could have been released, but remained within the planet's atmosphere due to gravity.

2.1.2. The Galileo Mission: Jupiter's enrichment

In its present form, the solar system contains eight planets, many with moons, as well as thousands of smaller bodies. All these bodies formed from the same molecular cloud, however differ considerably in their composition and properties. Jupiter, which orbits the Sun at approximately 5AU, is the largest and heaviest of these planets. In the below discussion, the Sun's composition, believed to closely resemble that of the molecular cloud, is compared to Jupiter's, as measured by the Galileo mission probe.

The elemental abundances in the solar nebula have been estimated using different datasets. The elemental composition of the Sun and its ejections have been measured using different spectroscopy techniques, as well as sample analysis of meteorites and asteroids [12]. Often the ratio between abundances is determined, rather than a raw percentage of mass total. A common ratio of abundances can indicate a common origin. Solar spectroscopy has been used to determine the composition of the solar nebula: the portion of the cloud that collapsed to form the Sun system. This is based on the assumption that the Sun formed from only material in this initial solar nebula and thus has the same elemental composition. The technique is limited because of the occurence of heavy-element fractionation in the Sun. The abundances of the noble gases He, Ne, Ar, Kr, and Xe cannot be derived from the photospheric spectrum [12]. Certain noble gas abundances (Ne and Ar) can be derived from coronal sources such as direct particle measurement of coronae or solar winds. The effect of solar wind on lunar soil has been used to deduce the abundance of Ar [24]. No solar abundance data is available for Kr and Xe, however their abundances have been derived theoretically [12] [25]. Table 2.1 provides the estimated abundances in the initial solar nebula, i.e. the portion of the molecular cloud that collapsed to form the solar system. The abundances are expressed in terms of H_2 [12]. Some of these values, i.e. for

Ar [24], have not been directly measured but are a compilation of estimates from different data sources.

Species X	**X/H_2**
C	5.82×10^{-4}
CO	1.94×10^{-4}
CH_4	1.94×10^{-4}
H_2O	5.78×10^{-4}
Ar	8.43×10^{-6}
Kr	4.54×10^{-9}
Xe	4.44×10^{-10}

Table 2.1: Gas-phase abundancies of several elements and compounds [11]. Abundances are expressed in terms of H_2, the most abundant molecule in the solar nebula [12].

The 1995 Galileo mission to Jupiter was the first to place a satellite in orbit around the planet. It provided extensive data on the composition of the gas giant through its mass spectrometry probe measurements. Such data of bulk composition cannot be attained through remote observation. Most volatile species have not yet been succesfully detected through remote sensing. Noble gases are completely undetectable, as they do not readily bond to other species, to form molecules which can be detected by e.g. infrared measurements. The measurements of noble gases can be compared with solar abundances, which are expected to closely reflect the abundances of the protoplanetary disk [26]. Abundances are measured with respect to a more abundant element or molecule, in this case hydrogen. The abundance distribution in the atmosphere of Jupiter provides insight into the formation rate and location of the planet. A relative enrichment of noble gases indicates that the gases froze onto grains or were trapped in growing ices, which can only have occurred beyond the snowline of the respective ice. Differences in the noble gas isotope ratios between the Sun and Jupiter suggest a fractionation process in the formation of the grains and planetesimals that accreted to form Jupiter [26]. These fractionation processes are not expected to influence the total amount of the species carried by the grains.

A direct accretion of material in the nebula through gravity only would result in a ratio of 1:1 for noble gas abundances in Jupiter and the Sun. The Galileo probe measured enrichment of 3.30, 2.61 and 2.56 for Ar, Kr and Xe respectively in Jupiter's atmosphere. These abundancy ratios, and their uncertainties, relative to the solar composition are shown in Table 2.3. The abundance of helium and neon are significantly lower, however these noble gases are believed to be depleted from the atmosphere through atmospheric processes on Jupiter [27]. Since Jupiter carries relatively large amounts of noble gas it must have accreted enriched materials during its formation. This imposes a significant constraint on planetary formation models, since the delivery of enriched materials requires (1) their initial trapping in the carrier and (2) their retention during any physical processes undergone during the inward drift. The possible delivery of noble gases in different forms of water ice are presented in the next section.

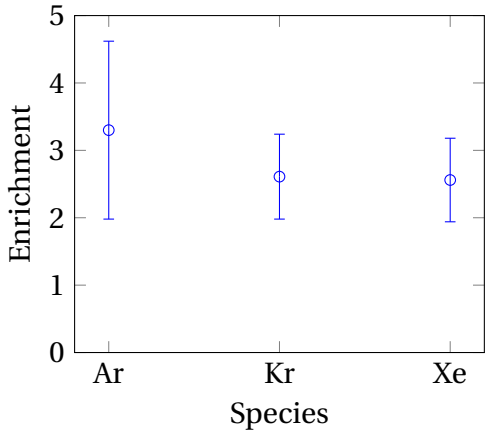

Figure 2.3: Enrichment of Jupiter with noble gases. Enrichment is computed as molar abundance of the species to the molar abundance of H, divided by the same molar abundance ratio in the Sun [2].

2.2. Enrichment mechanisms

2.2.1. Water ice as a species carrier

The core accretion model as described in the previous section proposes planets grow through the accretion of grains. A dust grain will initially consist of a silicate or carbonaceous core. Ice layers can accrete onto this core, and desorption and reaction processes can turn this ice into a complex mantle containing species other than the base ice. The nature of these reservoirs could leave pronounced signatures in the planets onto which they accreted, as different types of ice capture and retain species at different rates. Figure 2.2 gives an overview of the mechanisms through which water ice could have contributed to the enrichment of Jupiter. The expected atmospheric signatures differ between these mechanisms. The enrichment signatures which are studied in this work are highlighted in red. This includes the dependence of the signatures on the formation conditions, as well as any heating the ice would undergo after formation. Amorphous water ice, the focus of this study, is discussed in more detail in the next section, and discussed further in Section 2.3.

2.2.2. Amorphous solid water

In amorphous water ice or amorphous solid water (ASW) the molecules are not ordered. The formation conditions for amorphous ice are less specific as a consequence. Amorphous ices are formed temperatures below 135K. Ices formed at higher temperatures take on an ordered crystalline structure. Ices formed at lower temperatures but heated to this temperature reorder themselves to become crystalline. This transition temperature is shown on the H_2O phase diagram in Figure 2.4. Amorphous ices have no long-range molecular order, and in that sense resemble liquids [28]. Most ices in the universe are amorphous, though large clumps of ice may contain both crystalline and amorphous portions. If the ice accretes at temperatures below 30K all relevant noble gases would adsorb to the ice grains [29]. Such low temperatures would only have been found at large distances from the Sun, in the region of the Kuiper Belt. The inward migration of such particles at those temperatures would then deliver a uniform enrichment. However, if the ice grains were heated upon their inward migration a depletion of the more volatile species is expected.

Source ice type	Amorphous	Crystalline		
Material accreted	Enriched amorphous pebbles	Condensated, pure noble gas and volatile ice	Enriched clathrates	Gaseous volatiles and noble gases, no water vapour
Constraints	• Low formation temperatures (<30K) required to trap e.g. Ar, N_2 • Accretion occurring before the transformation to crystalline ice at 135K	• Water ice must have reached a temperature of 135K to release trapped volatiles during the crystallisation process • Condensation of the noble gas species after their release at 135K+, occurring at different, lower temperatures	• Minimum temperature of 135K to release trapped volatiles • Sufficient water budget to encage species; preferential trapping occurs if the water budget is limited • Presence of the physical conditions that allow for clathrate formation, which has not been conclusively observed experimentally under disk conditions	• Minimum temperature of 135K to release trapped volatiles • Maximum temperature of 150K, at which water ice would vapourise • Sufficient Jupiter mass to reach the *pebble isolation mass*, at which gas is captured but larger pebbles do not fall into the planet
Atmospheric signatures	• Uniform enrichment if accreted at low temperatures, non-uniform if heated during inward motion • Significant enrichment with water molecules	• Non-uniform enrichment of noble gases • Variable enrichment depending on formation and accretion location	• Non-uniform enrichment of noble gases • Significant water enrichment with water molecules	• Uniform enrichment of noble gases • Minimal enrichment with water molecules

Table 2.2: Overview of enrichment mechanisms involving water ice.

The conditions for preserving a uniform enrichment are studied in this report.

At around 135K, amorphous ice rearranges itself into a crystalline arrangement. During this process, trapped species are released into the gas phase. The crystalline ice structure is more stable, and released gases may recondense onto the grain. Because the equilibrium temperatures of the noble gases differ, they are expected to condense at different temperatures and thus at different times in the protosolar nebula evolution. The abundance ratio of species A to species B on the solid grain should be higher than the one in the initial released gas phase if species A condensates at a higher temperature (and thus *earlier* as the disk cools down) than species B. It could also be the case that the particles drift inward at a sufficiently high rate that the desorbed gas is left behind. This gas would then be highly enriched with noble gases, but not with water vapour which would be carried inward in its crystalline form. This does however constrain the forming area of Jupiter. A temperature of 135K is required to initiate crystalisation and thus release of trapped species. However at 150K the water ice itself will begin to desorb, leading to both volatile and water enrichment in the gas left behind. In addition to this temperature constraint, Jupiter must have reached the so-called pebble isolation mass [30]. At this mass, the gas disk around Jupiter would be sufficiently perturbed to prevent the depleted icy pebbles from falling into the planet, enriching it with water.

A variant of crystalline ice is the clathrate, which are cage-like structures around guest molecules. Clathrate formation is a non-chemical process which can influence the abundancies of heavy elements on solar system bodies. A clathrate is a cage of ice molecules around another molecule. The formation of these clathrates in low-pressure environments

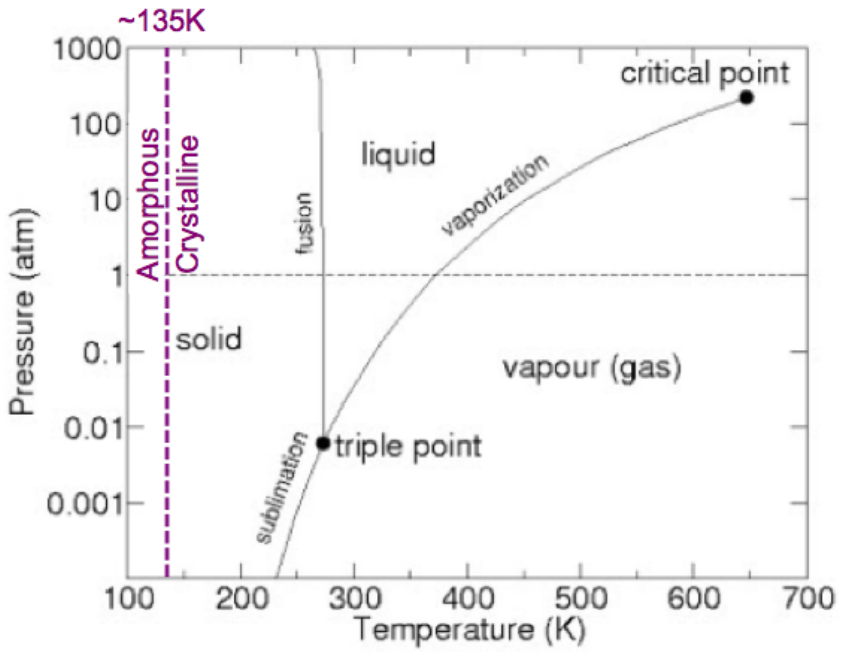

Figure 2.4: Phase diagram of H_2O. The amorphous to crystalline transition temperature shown in purple has been added to the original [3].

such as interstellar space is believed to occur during the warming of amorphous ices which have experienced vapor deposition. In these environments clathrates form by rearrangements in the solid state [31]. The role of clathrates has drawn more attention since the Huygens probe measured the composition of Titan, a moon of Saturn. The atmosphere is depleted in primordial noble gases other than certain Ar isotopes [32]. These observations suggest deviations from the widespread abundance of noble gases in other places in the solar system [33]. Thermophysical models of clathrates predict a relatively efficient trapping of CO, H_2S, Kr and Xe in clathrates originating in low temperature zones, at the expense of N_2 and Ar [34]. Unless a sufficient budget of water vapour was available to encage all the present gas, a clathrate dominated grain would thus carry a non-uniform enrichment of noble gases, and contribute significant water to the planet.

2.2.3. The budget of water vapour

As discussed above, the availability of water vapour is necessary for the formation of any type of ice capable of carrying species towards the inner regions of the solar system. It is essential that these water molecules are present in vapour form rather than accreted ices, as an solid ice could capture at most a single monolayer of adsorbed noble gases. Another constraint is imposed by the high volatility of Ar in particular, which requires temperatures below 30K to accrete [5].

A selection of relevant conditions in the protoplanetary disk are shown in Figure 2.5, based on the work of Woitke et al. [4]. In the top row, the temperature profile of the disk is shown, showing the <30K region in the midplane of the disk beyond 30AU. In the second and bottom panel the H_2O vapour and ice concentrations are shown, respectively. These concentrations are relative to the H concentration. Most of the H_2O in this region is in ice

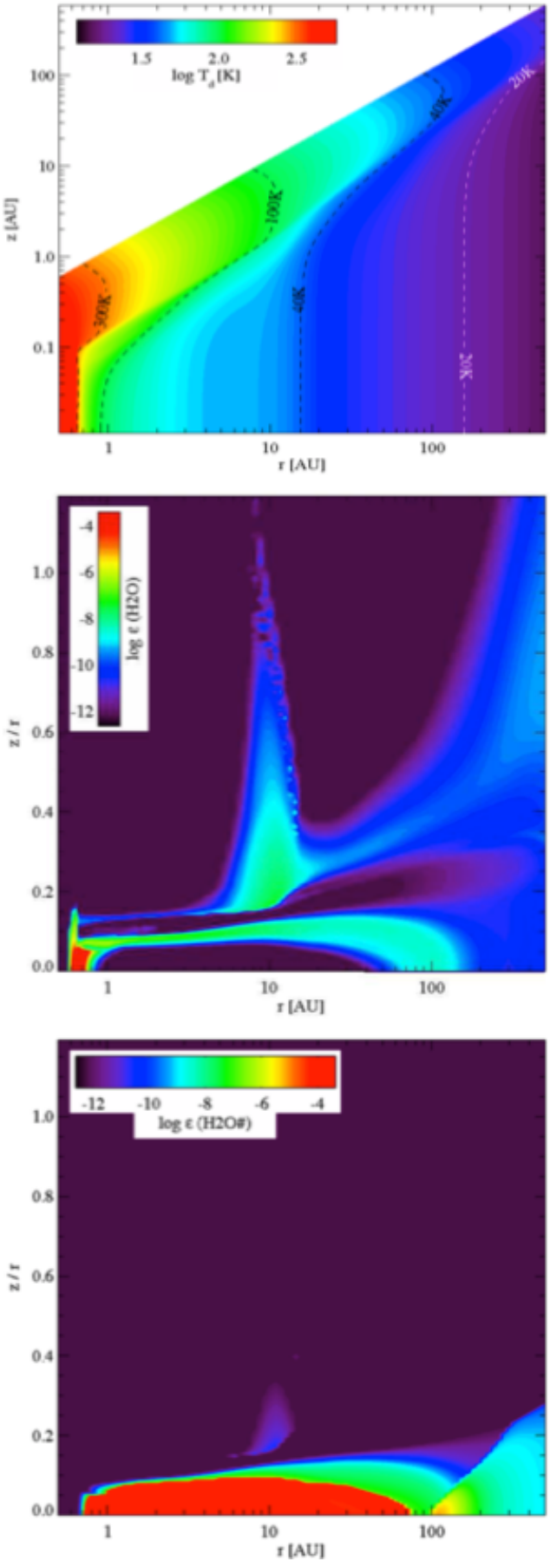

Figure 2.5: Relevant conditions in the protoplanetary disk. From top to bottom: Temperature, H_2O vapour concentration, H_2O ice concentration. Concentrations are expressed relative to H [4].

form, with a concentration of 10^{-4} relative to H. In this model, the concentration of H_2O is $\sim 10^{-10}$. The infall of UV flux generated by nearby stars onto the protoplanetary disk has been invoked to derive a mechanism which generated additional water vapour in the colder areas of the disk [17]. This mechanism would cause a more even balance of H_2O ice and vapour. This process is qualitatively described below.

In addition to the interstellar radiative field that permeates space, the early Solar system is believed to have been exposed to UV flux from nearby stars. This stems from the observation of the birth of stars in relatively dense clusters, making encounters more likely. This UV flux would have been several orders of magnitude larger than the interstellar flux if a sufficiently large star had passed the disk at a distance of around 12 lightyears. This UV flux impinges on the outer regions of the protoplanetary disk, where the optical depth is lower and temperatures are higher than in the midplane as is shown in Figure 2.2. The flux can trigger the photodesorption of water molecules from icy grains found in these regions, creating a reservoir of water vapour. Vertically, the disk is mixed by turbulence, and this vapour will over time thus cross through the cooler midplane. At the midplane it encounter the temperatures needed to recondense, as well as trap other species. As the condensed grains grow large enough, they start to fall inward due to gas drag. The enriched water ice grains move inward against the outward flow of lighter gasses occuring in the midplane. The grains leaving the region of the disk of interest thus carry a net enrichment with noble gases. The region of interest is confined by the temperature criterion of 30K at around 30AU and the edge of the protoplanetary disk at around 70AU. Figure 2.2 shows the widening of the disk in outer regions; the temperature limit of 30K is found at a height of approximately 6.5AU above the midplane in this region [17].

The ability of this water vapour generation mechanism to deliver enriched materials is dependent on a handful of assumptions, which are mentioned here to conclude the section. These assumptions are a component of the knowledge gap which is discussed in Section 2.4. The first assumption is the presence of another stellar body in the vicinity of the solar system shortly after its initial formation. The second is this body's UV flux being capable of generating sufficient water vapour to trap all the heavier gas species. The need to trap all gasses has been disregarded in previous works, but Ar's higher volatility in combination with the uniform enrichment measured requires this. Lastly, assuming there is sufficient water vapour to trap all these species, the uniform enrichment must then be assumed to be preserved after the ice grains have left the formation zone outside 30AU. Due to the different desorption temperatures of the different noble gases, initial entrapment in a given ratio does not guarantee delivery to a forming Jupiter in those same ratios. These amorphous ice desorption mechanics are presented in more detail in the next section.

2.3. Enrichment of amorphous water ice

In this section, amorphous water ice will be discussed in more detail. First, the porosity which makes amorphous water ice an effective carrier of trapped species is explained. The release of trapped species as amorphous water ice is heated is then discussed, based on experimental observations.

2.3.1. Porosity

In this section the properties of amorphous water ice that make it an effective trapper of gas species are described. The ice that forms in the region of the protoplanetary disk of interest, with temperatures below 30K, is amorphous.

Amorphous ice requires less specific conditions to form than crystalline ice. In amorphous ice the molecules are not ordered. Amorphous ices have no long-range molecular order, and in that sense resemble liquids [28]. Crucially, amorphous ice can also be highly porous, with large voids able to form in the ice as molecules adsorb and desorb from the surface. Crystalline ices can also be porous on the surface, but are unlikely to carry voids in their deeper layers. Formation of porous ices can occur as a result of the adsorption of water molecules released by photodesorption, as explained in the previous section. Water vapour can also be released from the ices via sputtering. Sputtering is the removal of attached molecules by the impact of high energy particles. These particles are then redistributed on the cold surfaces, leaving behind pores. The porosity is the volume of voids or pores in an ice as a fraction of the total volume. In terms of average and bulk density the porisity is written as [35]:

$$p = 1 - \frac{\rho_{average}}{\rho_{bulk}} \tag{2.1}$$

The porosity of ices plays an important role in the physical and chemical processes that occur around the ice. A highly porous ice has a higher surface area to volume ratio, allowing for the easier capture of molecules. Ice porosity thus plays an important role in the ability of an icy planetesimal to trap noble gases. The porosity is a physical parameter which is difficult to measure remotely. However remote measurements have provided the inventory of interstellar ices, and optical constants could allow for the abundances to be deduced in the future. Recent studies have identified the influence of porosity on optical constants, and thus allow for deduction of the porosity of interstellar ices [36].

Open pores left behind by desorbing molecules, or naturally formed by the non-uniform accretion of an ice layer, can be filled by noble gases. Noble gas molecules reside in the pore for a time that depends on their interaction with the surrounding ice molecules. The length of the stay is dependent on the sublimation temperature of the gas, the size of the particle and the pore, its polarizability, the strength of the interaction with the dangling OH bonds [37], as well as the mass of the molecule or atom [38]. Different noble gases and also different isotopes of the same noble gas are thus expected to be captured and retained at different rates.

The unorganised structure of amorphous ice allows for the formation of pores. If a noble gas were to fall into this pore while water continues to accrete on top of it, the noble gas can be trapped in the ice. The differing residence times of these noble gas atoms in the pore pose a challenge to the delivery of a uniform enrichment. Given the low sublimation temperature of Ar, it is expected to be retained less effectively in pores. The release of Ar and other noble gases from amorphous ice is discussed in the next section.

2.3.2. Release of trapped species

The entrapment and release of Ar in amorphous ice has been studied experimentally. The entrapment of Ar was studied, both by flowing gas onto settled ice or the simultaneous deposition of water vapour and the gas [5]. These experiments were conducted at accretion temperatures of $\sim$20K, in line with the formation conditions proposed in previous sections.

The release of the gas was measured as the temperature was increased. This revealed seven regimes of gas desorption, as is shown in Figure 2.6. The flux of Ar and H_2O are shown by seperate curves in this figure. The heating rate in this experiment was 3K min^{-1}.

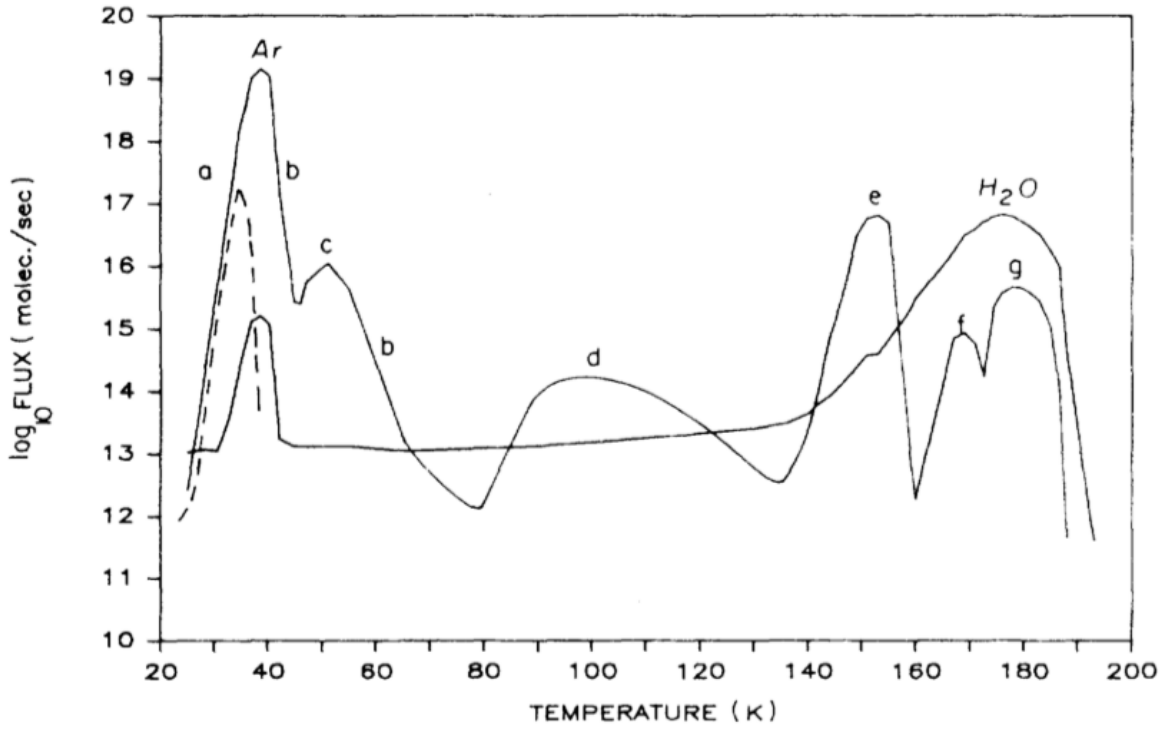

Figure 2.6: Different regimes of argon desorption from amorphous water ice. The H_2O flux at ~30K is loosely bound water molecules evaporating with the frozen Ar. The last peak (g) corresponds to the remaining trapped Ar released only when the water ice itself desorbs [5].

The regimes will be presented in their order of appearance, i.e. from lowest to highest temperature. Regime (a) occuring at ~35K is the desorption of frozen multilayer Ar. Regime (c) occuring at ~45K is the desorption of a monolayer of Ar on the ice surface. It is noted that regime (a) is superimposed on regime (b) and only visible when the volume of desorbing Ar is not too large. Regime (d) is due to the diffusion of the ice molecules and trapped atoms, which allows trapped species to 'creep' to the surface from where they can desorb. The sharp peak (e) starting at ~137K is the transformation of amorphous ice, formed when the ice is deposited at a low temperature, into cubic ice. The movement of water molecules forming the cubic lattice, frees some of the trapped argon and squeezes it out. This transformation does not appear to be dependent on the heating rate [5]. The (f) peak starting at 160K is a gas release associated with the transformation of the cubic-structure ice into hexagonal-structure ice. The final regime (g) coincides with the desorption of the water ice itself, and includes all the remaining trapped Argon gas which was not released by any of the previous mechanisms. It is noted that the flux of water is smaller than the flux of Ar by several factors throughout the heating process.

At sufficiently low temperatures, noble gases can bind to both water molecules and other noble gas atoms. The bonds formed with water ice are stronger than those formed with other noble gases, as will be discussed in Section 4.1. The so-called multilayer noble gas evaporates from the ice at lower temperatures than the so-called monolayer of ice on

top of the water ice. These terms will be used often in this work, and the difference between these two types of noble gas bonds is thus visualised for clarity. Figure 2.7 shows a 2D visualisation of water ice (blue particles) enriched with noble gas (orange particles). The noble gas bound directly to the water ice is referred to as the monolayer of noble gas, and are shown as filled circles. Noble gas bound to other noble gas particles are the multilayer noble gas, and are shown as dashed circles. Deeper in the ice more noble gas atoms are seen. These would not desorb from the ice at any temperature, as they are not on the surface. However, diffusion through the ice or desorption of the water molecules above them could bring them to the surface over time.

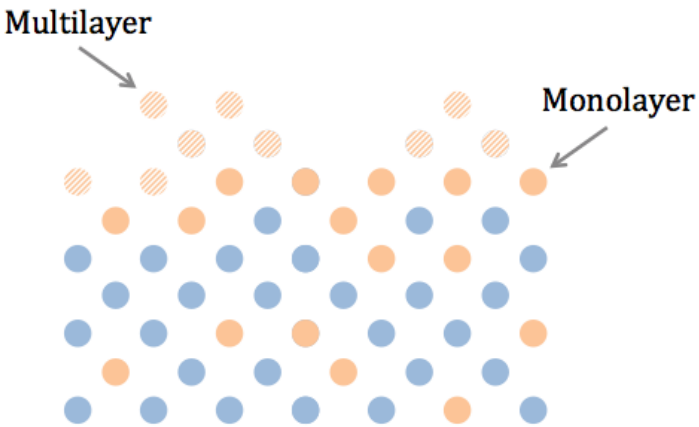

Figure 2.7: Visualisation of the mono- and multilayers of noble gas on amorphous water ice.

The key takeaways from these experiments are the distinct regimes of gas release from amorphous water ice below 100K. The first and second regimes are multilayer and monolayer desorption, respectively. The third is due to the creeping of the ice, which leads to a gradual outflow of Ar from the ice sample. The annealing continuously opens up pores containing the gas. The temperature range at which the different noble gases are released is relevant for the study of Jupiter's noble gas enrichment. This is the temperature range to which enriched amorphous ice particles are subjected to between their formation and arrival at the forming Jupiter. The retention rate of a noble gas in a pore is affected by multiple factors, and the release from said pore differs as a result. As of yet there is no work that conclusively studies the release of different noble gases, and the relative portions of retained material during heating. This knowledge gap and its implications are presented in the next section.

2.4. Knowledge gap

The solar system formed from a molecular cloud, the composition of which can be derived from the Sun's present day composition. While the composition of this cloud was initially uniform, physical and chemical processes drove the non-uniform distribution of species throughout the solar system. In Jupiter, a near-uniform enrichment with noble gases has been measured by the Galileo mission probe. A proposed mechanism explaining this enrichment is the delivery of enriched icy grains from distant, colder regions of the proto-

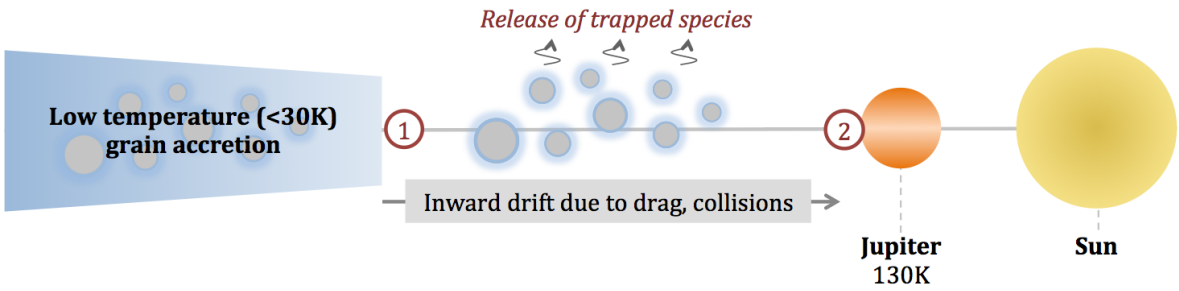

Figure 2.8: Overview of the amorphous ice delivery mechanism proposed to explain Jupiter's noble gas enrichment.

planetary disk to the forming Jupiter. The reservoir of water vapour required to trap noble gases in these grains is proposed to have been generated by the photodesorption of water molecules due to infalling UV radiation. Forming amorphous ice can contain open pores, into which noble gas atoms may settle, and be trapped if more water accretes onto it. An as of yet unaddressed issue, as depicted in Figure 2.8, is the expected non-uniform release of these noble gasses from the grains. Specifically, the assumption of a uniformly enriched particle heading towards Jupiter at point (1) is not expected to by extent yield an uniform enrichment upon delivery at (2). Specifically, the more volatile Ar is expected to be depleted relatively quickly from the ice. The research questions to be addressed in this thesis are thus the following:

1. What are the trapping efficiencies for the different noble gases during the formation of ices in outer solar system or interstellar medium (ISM) conditions?

   (a) What fraction of noble gas is trapped in different temperature conditions?
   (b) How does the ice thickness affect the release of species?
   (c) How does the water abundance affect trapping during formation, as well as retention during heating?

2. What are the conditions for the release of these noble gases from amorphous ice during heating?

   (a) How do the fractions of released gas compare?
   (b) How do these regimes compare to previous measurements?

3. Based on observed entrapment and desorption mechanisms, what contribution could enriched amorphous ice have made to Jupiter?

   (a) What constraints can be placed on grain accretion and heating conditions for the mechanism to remain viable?
   (b) How much enriched amorphous ice would have to be accreted to explain the observed enrichment?
   (c) What are the implications of these mechanisms for the atmospheres of the other giant planets Saturn, Uranus and Neptune?

3

Laboratory Data

3.1. Introduction

This chapter will summarise the relevant experimental work which has been conducted for the study of noble gas desorption from amorphous water ice. All experiments introduced in this chapter involve the deposition of species either simulationeously with water (codeposition) or on top of a layer of amorphous water ice. These experiments are conducted at temperatures at which the species may be bound to the surface of the ice or trapped inside. Subsequently, the samples are heated and the flux evaporating from the sample is measured as the temperature is increased.

The purpose of this chapter is thus two-fold. First, the experimental results provide physical input parameters for the simulations as described in Section 4.1. Second, these will be used to validate the theoretical model in Section 4.2. The model will then be applied to mixtures of noble gases in water ice which has not been studied experimentally.

Throughout this report, the experiments and simulations will be described using 4 key parameters: the deposition temperature, heating rate, ice thickness and water abundance (per trapped noble gas atom). Where relevant additional parameters may be included.

3.2. Pure noble gas ice

Smith et al. studied the desorption behaviour of several astrophysically relevant species from amorphous water ice [6]. These species were studied separately from each other, to isolate their specific desorption properties. The noble gas species were deposited on top of a prepared layer of amorphous water ice; the gases were not codeposited with the water vapour. These peaks are thus indicative of the binding energy of the multilayer binding energy of each species, as the bulk of noble gas atoms would be bound to other noble gas atoms rather than the water layer underneath. As will be seen in the next sections, the binding energy of a noble gas species to the amorphous ice (monolayer) is typically higher than the pure ice (multilayer) binding energy. The difference between these bonds was visualised in Figure 2.7. The desorption spectra of Ar, Kr and Xe deposited on amorphous water ice are shown in Figure 3.1. Different thicknesses up to 3 layers of pure noble gas ice were tested. The samples were deposited at 25K and heated with 1K per second. The colour coding indicates how many layers (ML) of the noble gas were deposited.

The peaks around 31K, 43K, and 60K for Ar, Kr and Xe respectively reveal the different

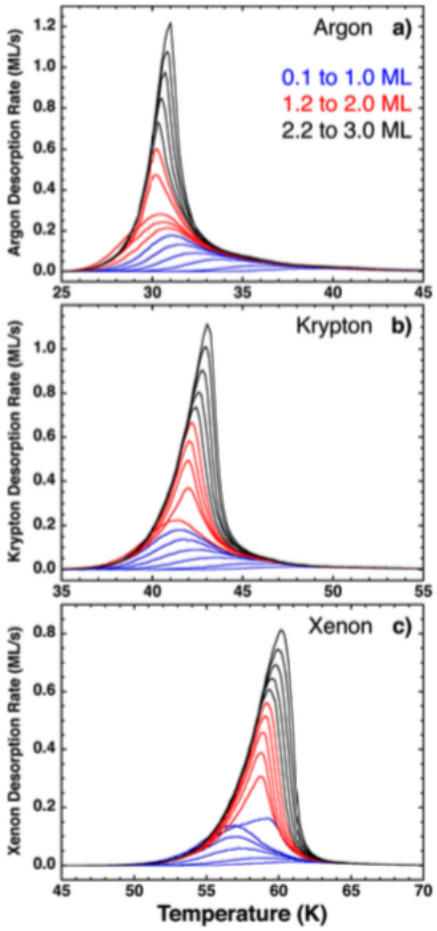

Figure 3.1: TPD of Ar, Kr and Xe deposited on a sample of amorphous water ice [6].

multilayer binding energies of these species. The most probable binding energies were computed to be 7.2, 11.4 and 16.3 kJ/mol for the species respectively. Below a temperature of 30K all these species would thus be expected to bind to an amorphous ice water grain, since the monolayer binding energy to water molecules is higher.

3.3. Codeposited Ar and H_2O

Bar Nun et al. studied the release of Ar from amorphous water ice [5]. The entrapment of Ar was studied, both by flowing Ar onto already deposited ice or by simultaneously depositing water vapour and Ar. These experiments were conducted at accretion temperatures of ~20K. The release of the gas was measured as the temperature was increased. This revealed seven regimes of gas release, as is shown in Figure 2.6. It should be noted that these results were also discussed in 2.3.2 in the context of the present work's research aims.

The regimes will be presented in their order of appearance, i.e. from lowest to highest temperature. Regime (a) occuring at ~35K is the desorption of frozen Ar on the surface. Regime (c) occuring at ~45K is the desorption of a monolayer of Ar on the ice surface. It is noted that regime (a) is superimposed on regime (b) and only visible when the volumes of Ar are not too large. Regime (d) is believed to be due to the slow annealing of the amorphous ice but has not been studied in detail. The sharp peak (e) starting at ~137K is the

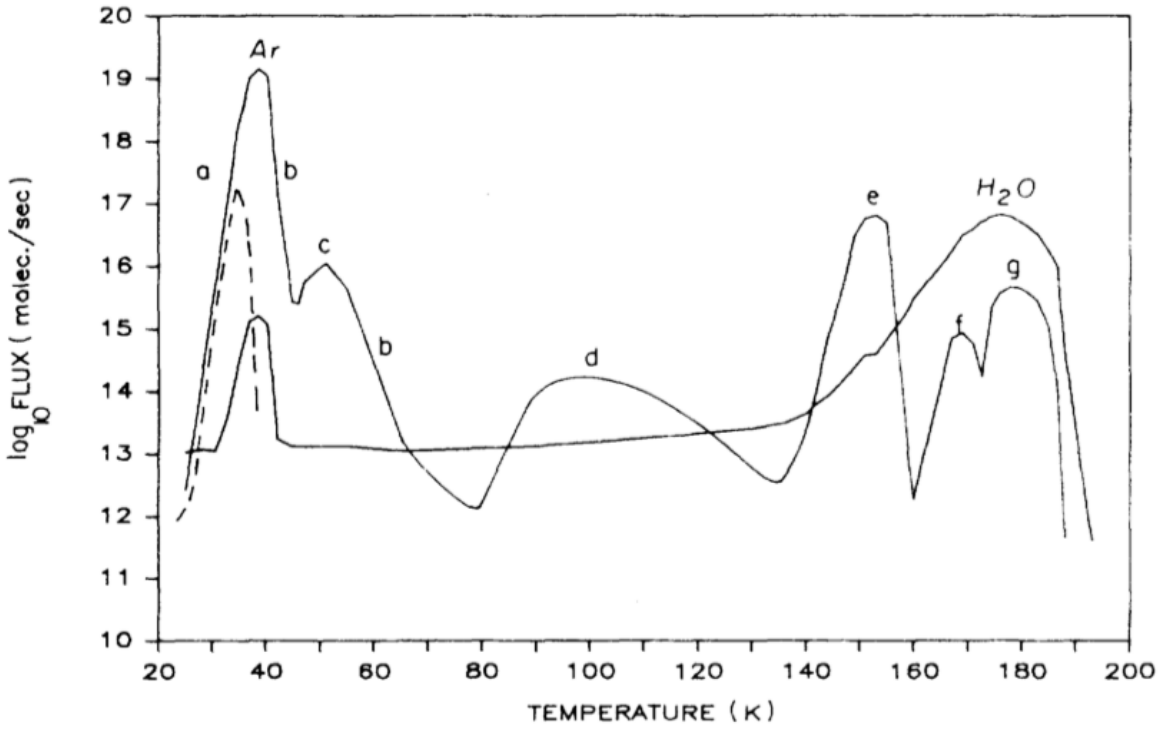

Figure 3.2: TPD of Ar codeposited with H_2O [5].

transformation of amorphous ice, formed when the ice is deposited at a low temperature, into cubic ice. The movement of water molecules forming the cubic lattice, frees some of the trapped Ar and squeezes it out. This transformation does not appear to be dependent on the heating rate [5]. The (f) peak starting at 160K is a gas release associated with the transformation of the cubic-structure ice into hexagonal-structure ice. The final regime (g) coincides with the desorption of the water ice itself, and includes all the remaining trapped Ar which was not released by any of the previous mechanisms. It is noted that the flux of water is smaller than the flux of Ar by several orders of magnitude for the majority of the heating process.

3.4. Codeposited Kr and H_2O

For the study of Krypton, use is made of unpublished experimental data provided by the University of Cergy-Pontoise. One set of experiments focused on capturing the monolayer desorption of Kr from water ice. This is thus the Kr which is bound to the water molecules rather than other Kr atoms. For this purpose a mixture of Kr and H_2O was codeposited at a temperature of 45K. At this temperature, Kr will form only monolayer bonds and not multilayer bonds with other Kr atoms, as this pure Kr desorption was found to occur at a temperature of around 40K (see also Section 3.2). Kr atoms deposited on top of other Kr atoms would thus quickly desorb back into the gas phase. In the experiments, different isotopes of Kr were detected; the Kr gas used for experiments contained more than one Kr isotope. For the purposes of this study these results are consolidated into the total Kr flux. The flux of all Kr isotopes was added together to compute the total flux. The results are shown in Figure 3.3.

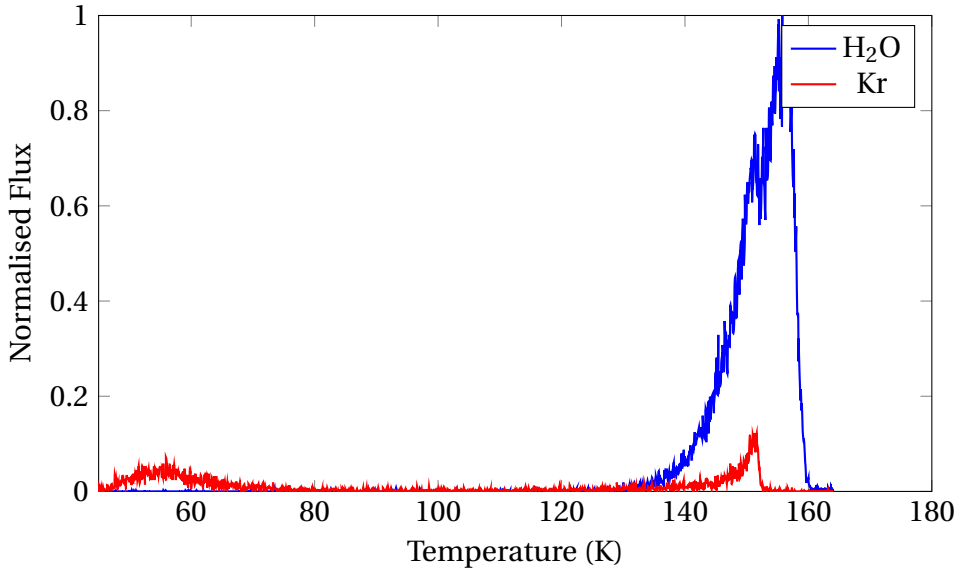

Figure 3.3: Experimental TPD of codeposited Kr and H_2O.

The flux in the figure has been normalised, with the peak water desorption flux measured equated to 1. The reason for this is that the number of molecules detected in experiments is several orders of magnitude larger than what can feasibly be simulated. The absolute number of atoms desorbing is less relevant than the proportional flux in each regime. The monolayer desorption regime is visible shortly after the heating begins, peaking around 55K. A second regime of Kr desorption can be seen at 150K. At this temperature water begins to desorb from the ice. As water desorbs previously trapped Kr is able to move to the surface of the ice and, at this temperature, readily desorbs from the ice. This is codesorption, which is only observed when the atom is trapped sufficiently deep in the ice. This regime is not driven by the binding energy of the Kr atoms to the ice, but by the binding energy of the water molecules. The creeping regime of the ice is not enough to allow these atoms to find a path to the surface. When the water itself begins to evaporate, however, the atoms are able to reach the surface from where they can desorb.

4

Monte Carlo Approach

This chapter covers the theoretical work conducted during this thesis. These simulations serve to provide conceptual indications of noble gas signatures which would be expected in planetary atmospheres enriched by amorphous water ice. Simulations allow for easy adjustment of input parameters, that are difficult or time-consuming to recreate or adjust experimentally. However, the accretion and desorption process from amorphous ice is complex and dependent on a multitude of physical factors. In this study, a Monte Carlo approach is used to simulate the behaviour of amorphous water ice. The methodology of this approach is presented in Section 4.1, alongside the physical constants chosen to describe the different noble gasses. Validation of the model, both from a stability and desorption mechanics viewpoint, is presented in Section 4.2. The chapter is summarised in Section 4.3.

4.1. Methodology

The theoretical work was performed using a Monte Carlo modelled developed at Delft University of Technology [7], amended for the specific purposes of this study. This Monte Carlo model simulates ices on a molecular level. A set number of particles are used to form an ice crystal. The ice then changes based on each individual particle's behaviour. A particle could move through the ice, or desorb from it altogether. The workings of the model are presented below.

4.1.1. Processes in ice formation

The simulation of desorption from amorphous water ice consists of two phases: accretion and heating. These phases are visualised in Figure 4.1. Below, the accretion process will first be discussed. The diffusion and desorption processes that occur during the heating phase are then discussed.

Accretion

In the accretion phase, a set number of water molecules, as well as other species, are deposited on a lattice at a low temperature. This phase is shown on the left side of Figure 4.1.

During deposition the accretion site is selected randomly. Once a particle has been assigned an accretion site, the binding energy at its new location is computed. The accretion

rate, in particles per second, can be computed as follows:

$$R_a = \rho v \sigma S \tag{4.1}$$

Where ρ is the density of the species, v is the thermal velocity proportional to $\sqrt{T_{gas}/m}$ km s^{-1}, where m is the species mass, σ is the cross section of the grain, and S is the sticking coefficient. The sticking efficiency is assumed to be unity at low temperatures. Experiments have shown that this assumption does not hold for hydrogen atoms at higher temperatures [39]. If the particle's velocity is too high, it may be unable to bind to the ice. Wakelam et al. [40] provided an indicative total nebular gas density of 10^5 and dust grain temperatures of 10-50K. Two notes are made regarding the density of the species. The first is that the density primarily affects only the accretion phase of the simulation, particularly the accretion rate. A higher gas phase density does not influence the desorption mechanics. However, since the density affects the accretion rate, a lower gas density means there is more time for the particles in the ice to diffuse or desorb while the ice is forming. The second is that the density in the gas phase is not necessarily the same as the abundance in the accreted ice. Due to different atomic masses, the abundance ratio of species 1 to 2 in the ice grain will scale by $\sqrt{m_2/m_1}$, owing to their accretion rates as described by Equation 4.1 differing by this factor.

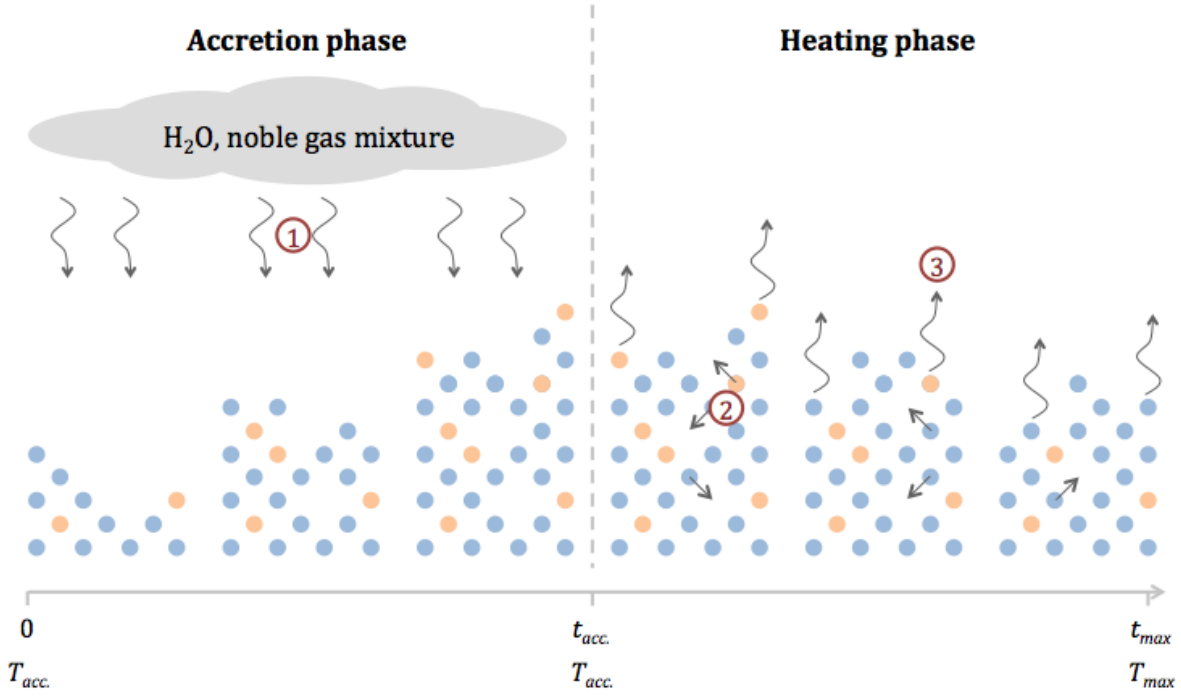

Figure 4.1: The two-phase process simulated numerically, showing water (blue) and noble gas atoms (orange). The composition of the gas reservoir as depicted remains constant during the accretion phase. The key processes of accretion (1), diffusion (2) and desorption (3) are indicated.

Diffusion

After the ice has accreted, the heating phase begins. During this phase, the temperature is increased at regular time intervals. This phase is shown on the right side of Figure 4.1. The

heating rates are 0.3 to 30 Kelvin per minute. During this time the molecules in the ice may move through the ice via diffusion, or leave the surface via desorption. These processes are respectively marked (2) and (3) in Figure 4.1. The water and noble gas atoms are marked blue and orange, respectively. The rate at which the different processes occur is dependent on the species neighbouring a molecule. The diffusion rate is then:

$$\text{Diffusion rate} = 4 \times \frac{\sqrt{\frac{E_f - E_s}{E_i - E_s}}}{\left(1 + \sqrt{\frac{E_f - E_s}{E_i - E_s}}\right)^2} \times \nu \exp\left(-\frac{E_{\text{act}}}{\text{T}}\right) \tag{4.2}$$

The pre-exponential factor ν is the so-called attempt rate; it indicates how often a particular species will attempt to move or desorb from a site per second. As can be inferred from the equation, the diffusion rate is an interplay between binding energy and the attempt rate. The results of experimental thus allow for the computation of the most likely values for both simultaneously, from the same dataset. $E_{b,i}$ and $E_{b,f}$ are the initial and final binding energy, respectively, and T is the current temperature. E_s is the saddle energy, defined as:

$$E_s = (1 - \alpha)\min(E_{b,i}, E_{b,f}) \tag{4.3}$$

E_a is the activation energy; besides the difference in initial and final energy, the particle must overcome an energy barrier. An energy barrier must also be overcome if the final energy is lower than the initial energy. This barrier is visualised for both cases in Figure 4.2. The activation energy is:

$$E_a = \alpha \max(E_{b,i}, E_{b,f}) + \max(E_{b,f} - E_{b,i}, 0) \tag{4.4}$$

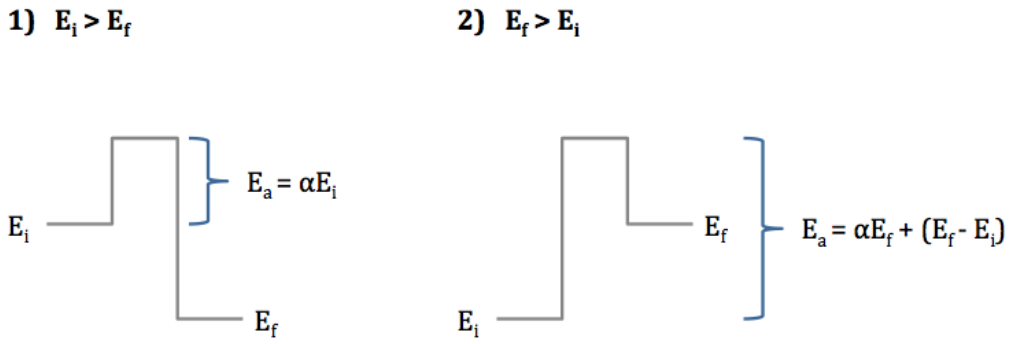

Figure 4.2: Energy barrier that must be overcome for diffusion both if the initial energy is higher (left panel) or lower (right panel) than the final energy.

The parameter α is the scaling parameter of the diffusion barrier to the binding energy. The higher α is, the higher the barrier for diffusion.

An atom may also move through the ice through swapping. Swapping places with a neighbour molecule sees weakly bound occupants to be 'kicked out' by more strongly binding particles. If the atom or molecule attempts to diffuse to a location of the lattice which is already occupied, the binding energy it would have at that site is compared to the binding energy of the current occupant. If the binding energy of the current occupant is larger, the swap does not occur. If the binding energy of the occupant is lower, the swap occurs.

Desorption

Species on a surface can desorb when they are located at the surface of the ice. The desorption rate is:

$$\text{Desorption rate} = \nu \exp\left[-\frac{E_b}{\mathrm{T}}\right] \tag{4.5}$$

The binding energy of a trapped species to the ice is dependent on the number of water neighbours n. A molecule can have at most 4 direct water neighbours as shown in Figure 4.3. The binding energy is taken to be the monolayer (i.e. noble gas to water ice) binding energy if the atom has 3 or more water neighbours. If the atom has less than 3 water neighbours it is only loosely bound to the ice structure and the lower multilayer ice binding energy is assumed. As can be seen in Figure 2.6, even in an evenly mixed water and Ar ice the majority of the Ar desorbs in the initial multilayer regime. This suggests that few of the Ar atoms are bound to the ice with the monolayer binding energy, warranting the relatively strict criterion of $n > 3$.

If a molecule or atom desorbs from the top of the ice, it is removed from consideration for the remainder of the simulation. Desorption within a pore is not possible; if desorption is the chosen event while the atom is not in the top layer of the ice, the simulation assumes diffusion to a neighbouring site instead. The direction of diffusion is random, and the probability for movement in all possible directions is determined entirely by Equation 4.2. As can be inferred from this equation, diffusion to sites with a lower binding energy $E_{b,f}$ occurs at a higher rate and is thus the more likely direction of movement.

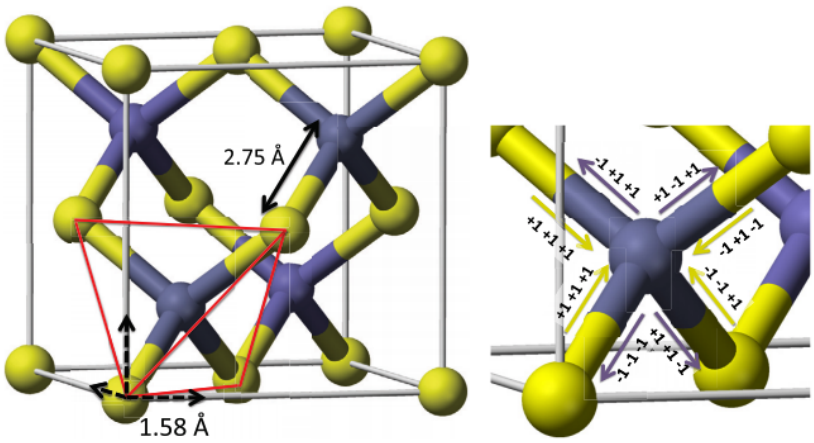

Figure 4.3: Visual representation of the lattice onto which molecules adsorb. In the left panel a unit cell is displayed, along with the relevant lengths used to compute e.g. the surface area and volume of pores. In the right panel the four possible directions of diffusion are shown [7].

4.1.2. Simulation parameters

The binding energy of a species to water is a key driver in the desorption and diffusion processes, as can be inferred from Equation 4.2 and 4.5. It is assumed that the desorption energy and diffusion energy scale linearly, with the diffusion energy 40% of the desorption energy. This is in the middle of a range presented in a study of volatile species on amorphous water ice, which suggested values between 29% and 57% [41]. For pure frozen noble gas, Smith et al. propose a multilayer binding energy of 866K for Ar, 1371K for Kr and 1960K

for Xe [6]. The same work estimates the pre-exponential factor on amorphous ice corresponding to these binding energies, which are listed in Table 4.1. Ar notably has a lower pre-exponential factor than Kr and Xe. Based on the desorption curves proposed by Smith et al. the average monolayer binding energy of Ar to water is set at 1443K. This corresponds to the findings of Bar Nun et al. [5], identifying a desorption peak of ∼50K of a monolayer of Ar from amorphous water ice. The temperature at which the flux of evaporating molecules of a species peaks, T_p, is expected to scale with the binding energy roughly by $E_b \sim 30T_p$ [42]. For Kr, the monolayer binding energy is based on the monolayer desorption peak shown in Figure 3.3 at around 60K. By the scaling relationship this equates to a binding energy of 1800K. For Xe, it is assumed that the multilayer to monolayer binding energy ratio is the same as that for Ar. This yields monolayer binding energy of 2940K for Xe. The binding energy of water is set at 5800K based on the work of Fraser et al [43], which proposed water desorption as a zeroth order process. Since the Monte Carlo assumes a first order process, the pre-exponential factor of 10^{30} molecules $cm^{-2}s^{-1}$ is converted to units of s^{-1}. Based on the grid density visualised in Figure 4.3, the ice has a density of $\sim 4 \times 10^{15}$ molecules per cm^2. The attempt rate is then approximately $2.5 \times 10^{14} s^{-1}$. The effectiveness of this conversion is tested in Section 4.2.

The binding energies for the noble gases used in this work are summarised in Table 4.1.

Table 4.1: Desorption energies used to model the noble gas-water interaction.

Species	Mass [amu]	$E_{b,\text{multi}}$ [kJ mol^{-1}]	$E_{b,\text{multi}}$ [K]	$E_{b,\text{mono}}$ [K]	ν [s^{-1}]
Ar	40	7.2	866	1443	6.2×10^{11}
Kr	84	11.4	1371	1800	1.2×10^{14}
Xe	131	16.3	1960	2940	4.6×10^{14}
H_2O	18			5800	2.5×10^{14}

4.1.3. Movement on the grid

It is assumed the water molecules are arranged tetrahedrally. This arrangement is shown visually in Figure 4.3. The grid of possible positions which a water molecule can occupy is thus predetermined. A water molecule cannot occupy a grid site with no neighbours (i.e. be floating in empty space). The locations where a water molecule can be placed is determined by the hydrogen bonds that holds the water molecules together. However, not every possible site in this arrangement needs to be occupied. Holes may exist in the structure if a site was not filled during the accretion of the ice, or if a species desorbs and leaves behind an empty site. These holes are referred to as pores, which the amorphous water ice on this grid is thus able to form. This porosity is described in detail in Section 2.3.1.

The mechanics of the model that determine the movement of a particle is visualised in Figure 4.4. The next event to occur is determined as follows. For every particle present in the ice, the possible sites of diffusion are identified. It is also checked if the particle is on the surface of the ice, from where it could desorb. The binding energy in the particle's current location is then computed, as well as the binding energy at all the possible destinations after diffusion. The diffusion and desorption rates as described by Equations 4.2 and 4.5 are then computed. Based on these rates, a time t_r required for each event to occur is computed, using a random number generator. The event with the highest rate thus has

the highest probability of being selected as the next event, but will not always be the event to occur. Once an event has been executed, the time is increased by the t_r of the chosen event. The process is then repeated. The heating rate is implemented by increasing the temperature T used in calculations by a certain interval ΔT after a certain time Δt has elapsed. $\Delta T/\Delta t$ is then the heating rate h.

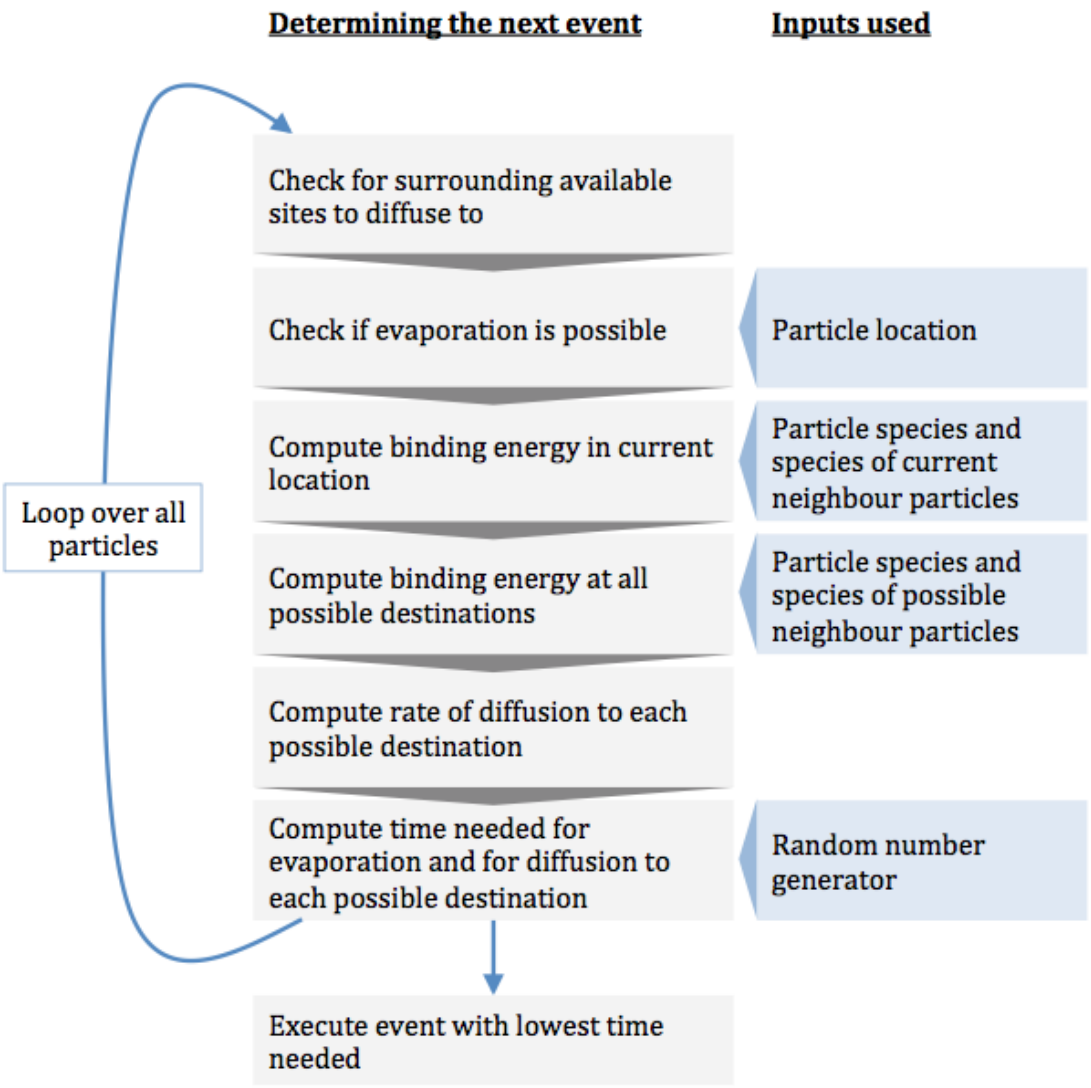

Figure 4.4: Flow-chart of how the model determines the next event.

4.2. Validation

The validation of the model was two-fold. The first set of simulations tested the general stability of the model through the variation of several input parameters. These included both model properties, such as grid size, as well as physical inputs such as the diffusion constant α. These simulations were conducted using a water-methane mixture, and assessed using the desorption pattern of methane from the ice and the change in porosity of the ice during the heating. The second set of simulations focused on ensuring the desorption mechanics

worked as intended. This was done by recreating the experimental conditions, and then comparing the TPD to the desorption regimes which can be seen in Figure 3.2 and 3.3.

4.2.1. Parameters study

To test the simulation model for stability, several test runs were conducted using a mixture of water and methane (CH_4) molecules. Only CH_4 was chosen alongside water so that the influence of different simulation parameters on the desorption can be studied separately. The diffusion parameter α as used in Equations 4.2-4.5, the deposition temperature T_d, the ratio of water to methane density r, the heating rate h, and the grid size g was varied. The variations were compared to a standard simulation with $\alpha = 0.4$, $T_d = 10K$, H_2O:CH_4 = 10:1, $h = 6$ K min^{-1} and $g = 60 \times 60$ grid sites. Table 4.2 lists the properties of CH_4 used in simulation, based on the work of Smith et al. [6] The flux of desorbing CH_4 and the ratio of the ice's surface area to its volume are presented. The latter provides an indication of the size of the pores; the presence or formation of smaller pores would increase this ratio. Based on the range of binding energies for methane to water, the peak desorption is expected to occur between 36K and 53K, following the methodology described in the previous section.

Table 4.2: Desorption energies and ranges considered for the noble gas-water interaction.

Species	Mass [amu]	$E_{\text{monolayer}}$ [K^{-1}]	$E_{\text{multilayer}}$ [K^{-1}]	ν [s^{-1}]
CH_4	16	1420	1050	9.8×10^{14}

The 11 different simulations conducted with the methane-water mixture are displayed in Table 4.3, with those parameters that have been adjusted from the standard case in bold. Included in the final column of this table is the fraction of methane remaining in the ice at the termination of the simulation, F, with a value of 1 indicating full retention of the initial methane. The results of the parameter variation are shown in Figure 4.5. From top to bottom, each row of panels shows the effect of variation in diffusion parameter, deposition temperature, water to methane ratio, heating rates and grid size. In the left panels, the desorption of methane from the ice is shown during the heating of the ice. In the right panels, the surface area to volume ratio of the ice is shown.

Table 4.3: List of simulations conducted to verify the influence of different model parameters.

Simulation	α	T_d [K]	r	h [K min^{-1}]	g	F
Standard	0.4	10	10	6	60	50%
1	**0.2**	10	10	6	60	57%
2	**0.6**	10	10	6	60	62%
3	0.4	**20**	10	6	60	50%
4	0.4	**30**	10	6	60	53%
5	0.4	10	**5**	6	60	45%
6	0.4	10	**1**	6	60	26%
7	0.4	10	10	**3**	60	52%
8	0.4	10	10	**1.5**	60	51%
9	0.4	10	10	6	**80**	52%
10	0.4	10	10	6	**100**	53%

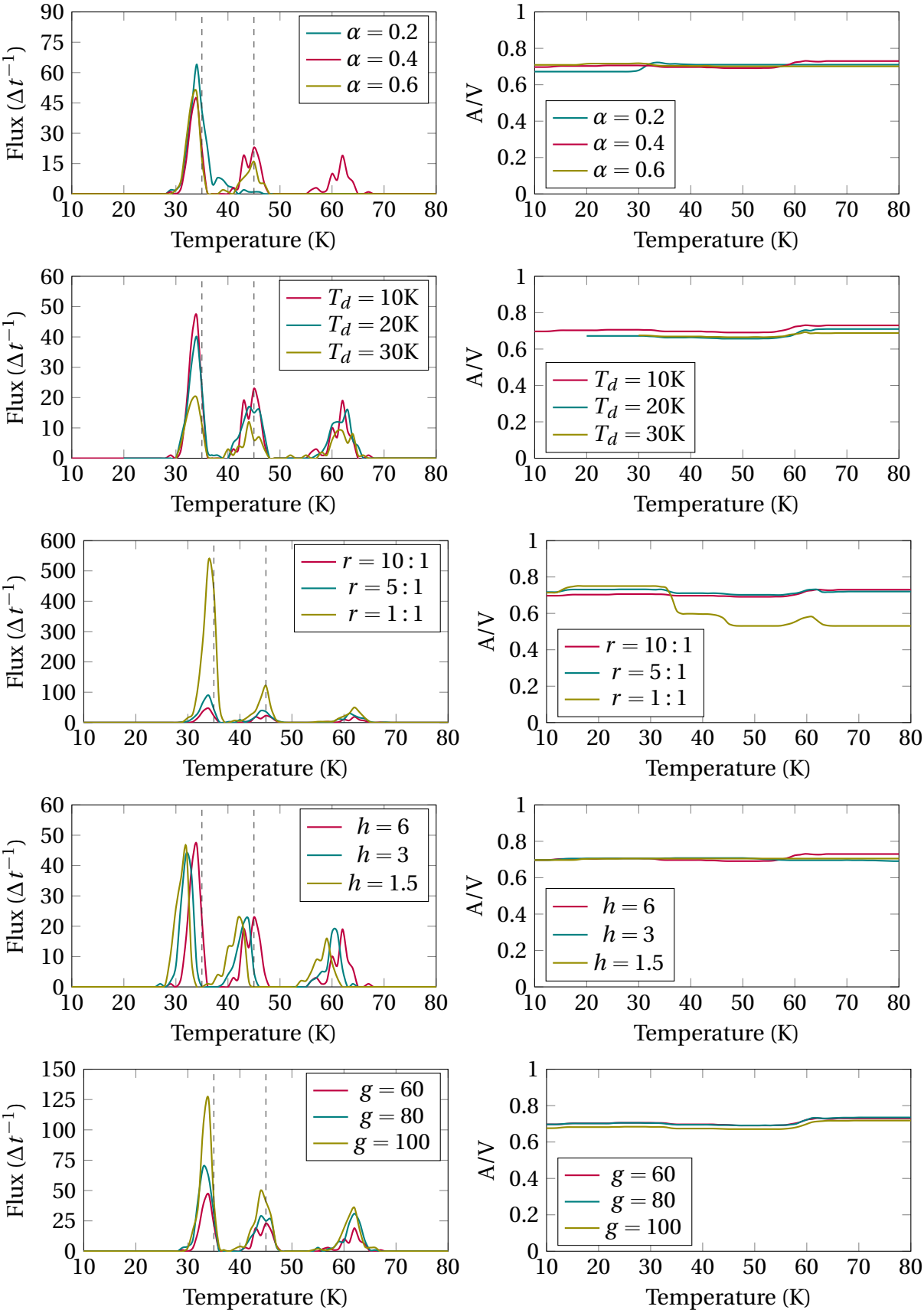

Figure 4.5: Output of the Monte Carlo model under the variation of different parameters: diffusion parameter α (top row), deposition temperature T_d (second row), H_2O:CH_4 ratio (third row), heating rate h (fourth row) and grid size g (bottom row). The flux of evaporating methane molecules (left panels) from the ice and the area to volume ratio (right panels) of the remaining ice is presented for each set of simulations. All simulations used a Δt of 10s. The standard simulation, indicated in violet on each figure, has a $\alpha = 0.4$, $T_d = 10$K, $r = 10:1$, $h = 6$K min^{-1}, and $g = 60$. The dashed grey lines indicate the expected multilayer and monolayer desorption peaks at 35K and 45K respectively.

The findings from the variation of each parameter are summarised below. The simulations in Table 4.3 will be referred to below by their number.

Diffusion parameter

The diffusion parameter α sets the barrier of diffusion. If α is higher, the barrier for diffusion is higher. The particles are thus expected to be less mobile in the ice grid if α is increased. This parameter is varied from the standard simulation in simulation 1 and 2 in Table 4.3. For the standard $\alpha = 0.4$, three desorption peaks can be seen in the top row, left panel of Figure 4.5. The first is the multilayer desorption of methane at 35K. The second at 45K is the monolayer methane desorbing directly from the water ice. The third peak around 60K can be attributed to the creeping of the ice, which gradually allows methane particles to come to the surface. For $\alpha = 0.2$ (Simulation 1 from Table 4.3), the diffusion barrier is lower. In this simulation, the multilayer desorption peak is stronger, while the monolayer peak is not as visible. However, the total fraction of methane desorbed was comparable (57% vs. 50%), suggesting the lower diffusion barrier simply made it possible for most particles to find a suitable desorption site before higher temperatures had been reached. For $\alpha = 0.6$, the diffusion barrier is higher. Only the multilayer and monolayer desorption peaks are visible for this simulation; the creeping regime is not visible as the particles do not diffuse enough to allow methane molecules to move to the surface from where they can evaporate. No notable changes in the A/V ratio can be seen in the top row, right panel. Over the course of these simulations, no changes in the structure of the ice can thus be concluded.

Deposition temperature

In Figure 4.5, second row, left panel, the methane desorption for three different formation temperatures is shown. This is the standard simulation and simulation 3 and 4 in Table 4.3. For all three different formation temperatures, the same three peaks can be seen: the multilayer desorption around 35K, monolayer desorption at 45K and a third attributed to the creeping of the ice. For lower formation temperatures, these peaks become less pronounced. This is explained by the fact that at higher formation temperatures, some of the methane falling onto the ice crystal are placed at sites from which they can immediately desorb. Some of the methane is thus released before the ice has finished forming. The ice formed at 20K and 30K thus retains less methane during formation, and the desorption peaks are less high as a result. No notable changes in the A/V ratio can be seen in the second row, right panel. Over the course of these simulations, no changes in the structure of the ice can thus be concluded.

Methane concentration

In Figure 4.5, third row, left panel, the methane desorption for three different heating rates is shown. This is the standard simulation and simulation 5 and 6 in Table 4.3. Because the size of the grid was constant, the ice naturally accretes more methane if the ratio is increased. For this reason, the peaks during heating are also higher, as there is more methane to be released. Qualitatively, the three different methane to water ratios show the same desorption peaks. However, a larger fraction of the noble gas material is released the higher the noble gas to water ratio. As this ratio increases, more of the noble gas atoms are bound to other noble gas atoms, rather than to water. Less of the noble gas thus remains trapped in deeper layers of water ice. For the methane:water ratio of 1:1, the third row, right panel shows a decrease in the A/V ratio during the multilayer and monolayer desorption peaks.

Evidently, the ice which remains after the methane has desorbed is less porous than the initial ice structure.

Heating rate

In Figure 4.5, fourth row, left panel, the methane desorption for three different formation temperatures is shown. This is the standard simulation and simulation 7 and 8 in Table 4.3. For the different heating rates, the desorption peaks are qualitatively comparable. In addition, for the different heating rates, around 50% of the initial methane is released during heating. This is a useful finding, as will be discussed in section 5.2.3. Because the realistic astrophysical heating rates are too low to be simulated, consideration must be given to the effect of different heating rates. At this scale the influence of the heating rate is thus not yet visible. No notable changes in the A/V ratio can be seen in the fourth row, right panel. Over the course of these simulations, no changes in the structure of the ice can thus be concluded.

Grid size

In Figure 4.5, bottom row, left panel, the methane desorption for three different grid sizes is shown. This is the standard simulation and simulation 9 and 10 in Table 4.3. This parameter was varied to ensure that simulating the ices on a relatively small physical scale does not deviate too strongly from the realistic scale. As can be seen, the three desorption peaks are qualitatively very similar. The peaks are higher for the larger grids. Since the methane to water ratio was constant over these simulations, the larger grids have a larger number of methane molecules to desorb. The fraction of methane remaining at the end of these simulations is around 50% for each. This suggests that grid size does not influence the simulations in such a way that the inferences of the simulations cannot be assumed to hold to larger areas of ice. No notable changes in the A/V ratio can be seen in the bottom row, right panel. Over the course of these simulations, no changes in the structure of the ice can thus be concluded.

The results of these simulations replicate the desired desorption regimes. The approach is stable for different sets of input parameters. In addition, the changes in the desorption spectra as parameters are adjusted can be explained conceptually. This indicates the model may be used for the behaviour of more complex gas mixtures.

4.2.2. Desorption mechanics

The second component of validation is testing of the desorption mechanics. In the model, a species may be released if it is at the top layer of the ice. It could either have been deposited there initially, or have moved through the ice by diffusion. How quickly the atom moves through the ice, and thus becomes eligible for desorption, is dependent on the diffusion factor α and its attempt rate or pre-exponential factor, ν. Once it has reached the surface, the probability of desorption depends on ν as well as the binding energy E_b. From the top layer an atom may also move back into the ice if it is does not desorb rapidly enough. The eventual TPD spectra, which are produced by tracking the number of evaporated atoms of each species, are thus influenced by various input parameters. The binding energy and pre-exponential factor parameters are sourced from results of experiments.

Codeposited Ar, water

The conditions in the Ar trapping experiments of Bar-Nun et al. [5] were used to recreate the results in Figure 2.6. This figure is relabelled in Figure 4.6. These experiments revealed distinct regimes in which gases desorbs from amorphous water ice. Since these experiments heated the ice up to ~200K, not all regimes are relevant for ices heated up to 130K. In particular, the release of Ar when water itself begins to desorb around 160K is not relevant for this temperature range. For the purposes of this study, the Ar multilayer desorption and the monolayer desorption are most relevant, since these are expected to peak at around 35K and 50K respectively. The experiment in question used a codeposited water mixture saturated with Ar at a 1:1 ratio, heated at a rate of ~3K min^{-1}. The results of this simulation are shown in Figure 4.7. The total flux of evaporating Ar molecules has been split into those desorbing from Ar ice directly (multilayer desorption) and those desorbing from water (monolayer desorption).

The simulation results, shown in Figure 4.7, will be compared to the experimental results shown in Figure 4.6. The simulation was able to recreate the three key regimes of Ar desorption at temperatures below 100K. The first is the multilayer desorption of pure Ar ice, which begins shortly after deposition and peaks at 33K. It is labelled with an A in Figure 4.6 and 4.7. Ar atoms do not desorb from water ice at this temperature as they are too strongly bound. The second regime, labelled B, of monolayer Ar ice desorbing from water is smaller in absolute flux and has a broader peak between 45 and 47K. After these first two regimes, around 20% of the initially deposited Ar remains in the ice. The third regime, labelled C, is the creeping regime. This is not linked to a specific binding energy, but commences around 65K and declines as the remaining Ar in the ice is depleted. After this regime no Ar remains in the ice. In the experimental work, this regime lasted to higher temperatures as there was still Ar left in the ice. It is cautiously assumed that this regime would have continued had there been more Ar in the simulations; the rapid depletion is attributed to the small number of Ar atoms. This issue of scale is discussed in Section 6.2. The regime labelled D is the codesorption regime. This occurs simultaneously with the peak water flux. When the water begins to evaporate from the ice, previously trapped Ar atoms may now be at the surface of the ice, and able to desorb. The peak between the C and D regimes is due to the restructuring of the ice to a crystalline structure. Since this will not be simulated, this regime will not be discussed here. These labels of A, B, C and D will be used in the analysis of simulation results. For clarity, they are again listed here:

(A) Multilayer desorption

(B) Monolayer desorption

(C) Release due to creeping of the ice

(D) Codesorption when water begins to evaporate

Over the course of this simulation, around 5% of the deposited water desorbs. As was the case in the experiments of Bar-Nun et al. [5], the flux of water relative to Ar is limited over this temperature range.

Codeposited Kr, water

To capture as many regimes as possible, ice with a thickness of ~ 30Å of evenly mixed Kr and water were deposited at 45K. As was done for the laboratory results, presented in Section 3.4, the resulting TPD flux has been normalised with 1 taken as the peak water flux.

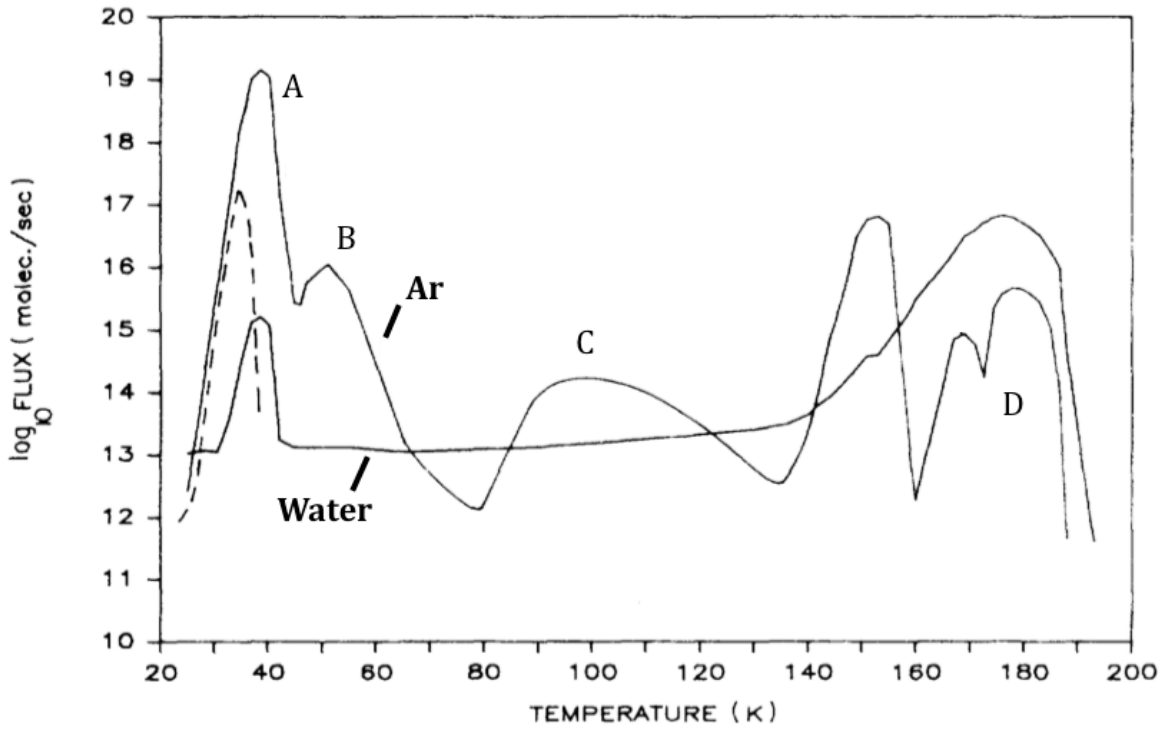

Figure 4.6: Different regimes of argon release from amorphous water ice. Original figure by Bar-Nun et al. [5] relabelled for the purpose of this study.

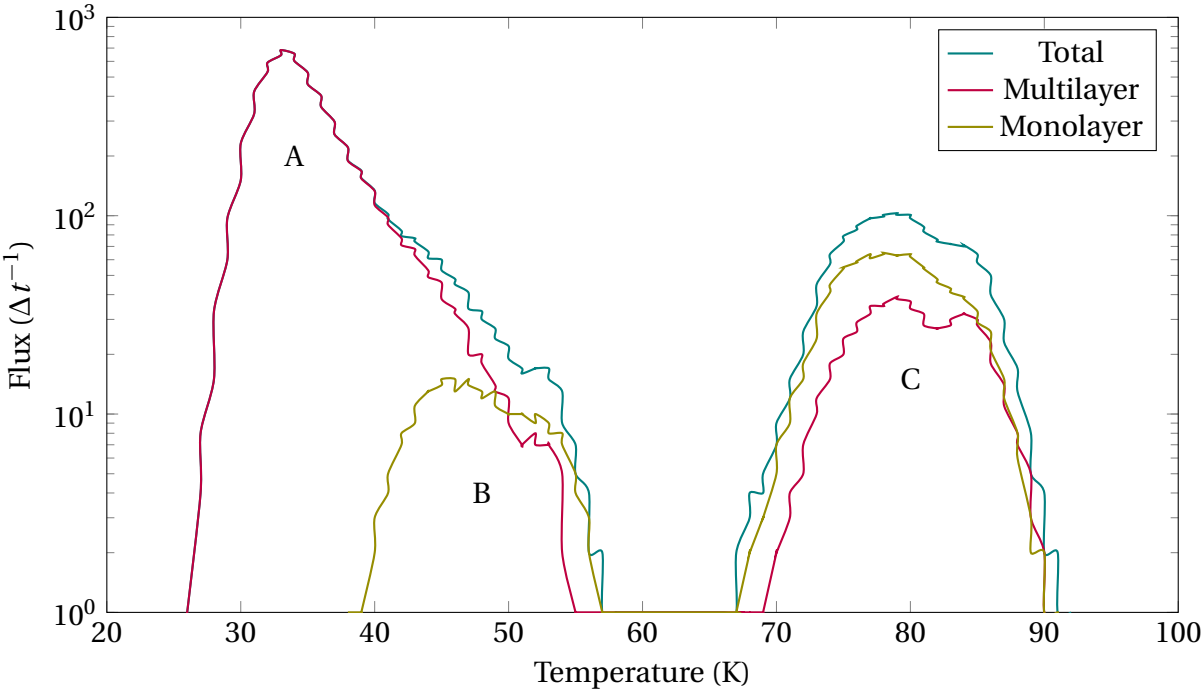

Figure 4.7: Desorption of Ar from amorphous water ice, accreted from an evenly mixed gas, heated at 3K min^{-1}. The regimes in order of appearance are marked with A, B and C.

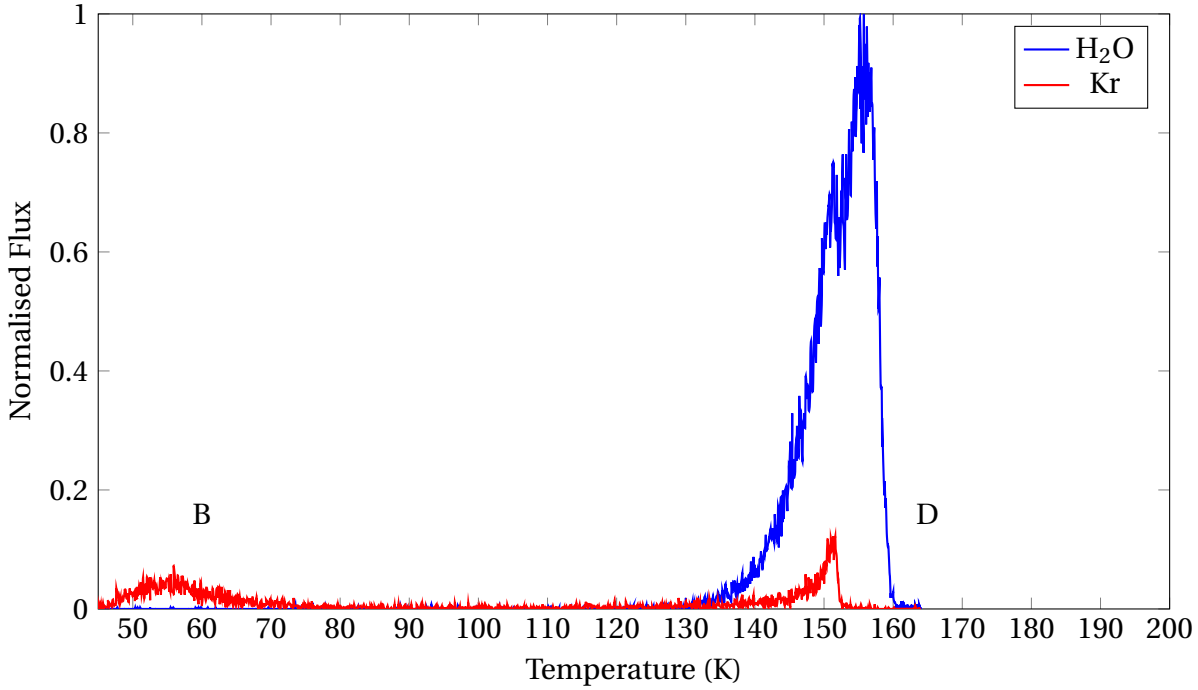

Figure 4.8: Experimental TPD of codeposited Kr and H_2O, with labelled monolayer (B) and codesorption (D) regimes.

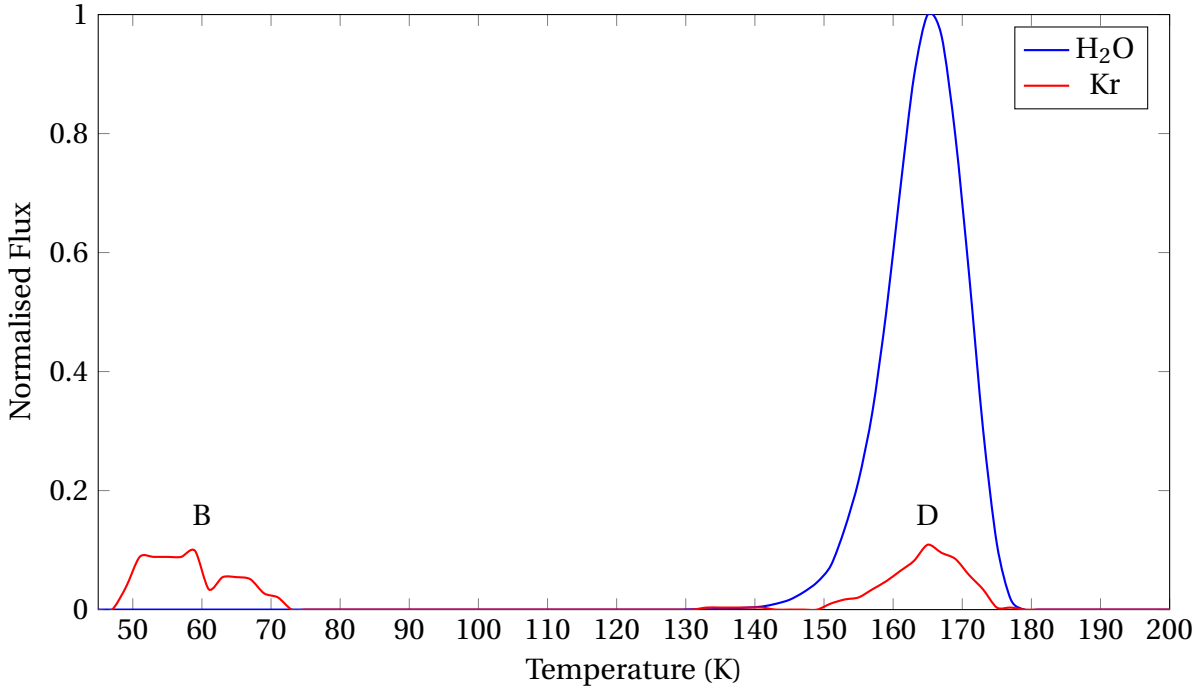

Figure 4.9: TPD of codeposited Kr and H_2O, with labelled monolayer (B) and codesorption (D) regimes.

The results are shown in Figure 4.9 and compared to the experimental results in Figure 4.8. In the temperature range 45K-60K the monolayer desorption regime is visible, labelled B consistent with previous regime labelling. As the water begins to desorb, a codesorption regime of Kr is seen which peaks around 165K. Kr atoms which were previously trapped in the water ice are now at the surface as the ice above them evaporates. This peak is labelled D. It is observed at a higher temperature than the 150K observed experimentally, as described in Section 3.4. This is attributed to the fact that the desorption parameters used (binding energy and pre-exponential factor) were translated from an observed zeroth order process to the first order approach that is applied in this model. This slight deviation is acceptable, as the water desorption temperature falls outside the temperature range of interest for the applications discussed in Chapter 5. For the lower temperatures studied in detail, the diffusion behaviour of the water molecules resemble observations sufficiently.

4.3. Summary

The numerical approach presented in this chapter has provided conceptual insights into the enrichment of amorphous water ice as it is moved from <30K formation zones to temperatures up to 100K. The agreement between desorption regimes observed in experiments and in these simulations means the model can be applied with confidence to other gas mixtures. These gas mixture with noble gases are introduced in the next chapter. The limitations which have been partially identified in this Chapter will be discussed in Section 6.2.

5

Astrophysical Application

5.1. Introduction

In this chapter, the model is applied in the context of the formation of planetary atmospheres. Icy grains forming at low (<30K) temperatures are simulated, and their composition is tracked during the heating which they would have undergone during their inward drift. The atmospheres of the giant planets Jupiter, Saturn, Uranus and Neptune will be studied. These planets consist of a small rocky core enveloped by a thick atmosphere of gas. This gas envelope consists both of gases accreted directly from the protoplanetary disk, as well as gases released from accreted solid material. The composition of this atmosphere can thus provide insights into how the atmosphere formed, and from what materials. The presence of noble gases in amorphous water ice will be simulated in this chapter. In Section 5.2 the parameters governing the different mechanisms driving the trapping and release of gases in ices are determined. These are based on the expected physical conditions during formation and heating of the icy grains, and the different measurements of release of noble gases. Consideration is given to the potential deviation of these parameters from the realistic astrophysical conditions. Based on this, the simulations performed to study planetary atmosphere composition is presented. In Section 5.3 the results of the simulations are presented in the form of desorption results as well as the enrichment ratios throughout the heating process. The results and their astrophysical implications are discussed in Section 5.4. This chapter is summarised in section 5.6.

5.2. Simulation parameters

In this section the simulation parameters are derived based on expected astrophysical conditions in the formation region of the ices, as well as during their inward drift. In order, the ice thickness, abundances of different species in the gas phase and temperature conditions will be discussed in the following subsections.

5.2.1. Ice thickness

In this section the possible ice thickness on a dusty grain will be computed. The protoplanetary disk is considered to be a mix of dust grains and gas. The gas phase consists predominantly of hydrogen H. Based on the work by Woitke et al. [4] displayed in Figure 2.5, the number density of H in the region of interest is $n_{\mathrm{H}} \approx 10^{10}$. The mass ratio of gas to

dust in the disk is approximately 100 [44]. A given spherical dust particle in the disk has a mass M_d of:

$$M_d = \frac{4}{3}\pi r^3 \rho_d \tag{5.1}$$

Where r is the grain radius and ρ_d is the dust density. The grain radius is taken to be 1 micron [44]. Assuming that H consitutes the bulk of the gas phase mass, the number density of the dust grains in grains per cm^3 is then:

$$n_{\text{dust}} = \frac{n_{\text{H}} m_{\text{H}}}{M_d} = 2.7 \times 10^{-11} \tag{5.2}$$

The number of H_2O vapour molecules available for this grain is then:

$$N_{\text{H}_2\text{O}} = \frac{f_{\text{H}_2\text{O}} n_{\text{H}}}{n_{\text{dust}}} \frac{n_{\text{H}_2\text{O,vapour}}}{n_{\text{H}_2\text{O,ice}} + n_{\text{H}_2\text{O,vapour}}} = 4.5 \times 10^5 \tag{5.3}$$

where f_{H_2O} is the number fraction of water in the disk reported in Table 2.1, and the second term is the fraction of H_2O in vapour form, with a value of $\approx 10^{-6}$ based on Figure 2.5 [4].

The number of available binding sites b on the dust grain is the surface area of the grain divided by the surface area occupied by each binding site:

$$b = \frac{4\pi r^2}{s^2} \tag{5.4}$$

where $s \approx 3$Å is the distance between binding sites. Assuming all of the available water molecules accrete onto the grain, the thickness Z in layers of ice is:

$$Z = \frac{N_{\text{H}_2\text{O}}}{b} \approx 27 \tag{5.5}$$

Assuming that the thickness of each layer is 3Å, this is an ice thickness of approximately 80Å. This value could be higher due to the influence of the mechanism discussed in Section 2.2.3, as the ice thickness scales with the number of available water molecules. A higher abundance of water vapour and thus thicker ice will also be considered in the discussion of the next sections.

For clarity, the following values are assumed:

Variable	Value	Source
r	1μm	[44]
ρ_d	2.5 g cm^{-3}	[44]
ρ_g/ρ_d	100	[44]
f_{H_2O}	5.78×10^{-4}	[11]
$n_{\text{H}_2\text{O,vapour}}$	10^{-10} cm^{-3}	[4]
$n_{\text{H}_2\text{O,ice}}$	10^{-4} cm^{-3}	[4]
s	3Å	[44]

Table 5.1: Values used to derive the ice thickness.

It is noted that the potential accretion of other abundant species, most notably CO, is disregarded in this calculation. CO is able to accrete at temperatures below 30K, so when the icy grains drift, CO sublimates. CO has an abundance comparable to H_2O. The presence of CO in an ice could lead to both a thicker ice as well as different desorption mechanics, since noble gases interact differently with a CO-enriched ice. However, the lack of applicable laboratory data means noble gas-CO interactions cannot be simulated at this point. This limitation is discussed in detail in Section 6.3.2.

5.2.2. Species ratios

Based on the work of Bar Nun et al. [5][45], the molar abundance of H_2O in an amorphous ice would be at least as large as the Ar itself, as at least one H_2O molecule is required to trap an Ar atom. A H_2O:Ar ratio higher than 100:1 is unlikely given their gas phase abundances (see also Table 2.1). The H_2O:Ar range considered is thus from 1 to 100. A numerical limitation presents itself in achieving the realistic astrophysical ratio between Ar and the other noble gases Kr and Xe. The ratio Ar:Kr and Ar:Xe is of order 10^3 and 10^4 respectively, as can be seen in Table 2.1. Considering that the number of particles which can be feasibly simulated is of the order 10^4, these ratios cannot be achieved numerically. However, the interest of this study is to determine the fraction that desorbs of each species, rather than the absolute amount. For that reason, a 1:1:1 Ar:Kr:Xe ratio is used in all simulations, so that the fraction of each species desorbed can be simulated.

The enrichment factors presented in Figure 2.3 [11] are relative to the abundance of each species in the Sun. In the accretion planetary model, the absolute abundance of species in Jupiter was determined by both pebble and gas-phase accretion mechanisms. The absolute abundance of the species in icy grains is thus not as relevant, as the final mass of material has been assembled through different means. As highlighted in Figure 2.3, the abundance of the species relative to each other, that is the ratio of their enrichment factors, is a better indicator of the delivery mechanisms responsible for the enrichment. As explained above, for computational reasons we use a 1:1:1 Ar:Kr:Xe ratio in the gas phase from which the grains accrete. To assess the consistency of results with the Galileo probe measurements, the enrichment of the grain relative to the gas phase abundances is computed. When referring to the Ar/Kr (or Ar/Xe, equivalently) ratio when presenting results or in discussion, this ratio is written:

$$\mathrm{Ar/Kr} \equiv \left(\frac{n_{\mathrm{Ar}}}{n_{\mathrm{Kr}}}\right)_{\mathrm{Grain}} \Big/ \left(\frac{n_{\mathrm{Ar}}}{n_{\mathrm{Kr}}}\right)_{\mathrm{Gas}} \tag{5.6}$$

Where n_i is the number of atoms of species i. For the 1:1 ratio used in the gas phase, the denominator of Equation 5.6 is 1. The Ar/Kr or Ar/Xe ratio is thus the ratio of the enrichment factors of these species. This same methodology was used to derive the ratios presented in Figure 2.3. The denominator in the astrophysical case is of the order 10^3-10^4 for Ar/Kr and Ar/Xe. For the rest of this work, the ratios simulated will be referred to by 1:1, 10:1 and 100:1. These ratios refer to a gas-phase abundance of H_2O:Ar:Kr:Xe of 1:1:1:1, 10:1:1:1, and 100:1:1:1 respectively.

5.2.3. Temperature conditions

Tanigawa et al. propose a temperature profile of $T(r) \approx 280/\sqrt{r}$ in the protoplanetary disk, where r is expressed in AU [46]. Based on current position, this equates to a temperature of

123K for Jupiter, 93K for Saturn, 64K for Uranus and 51K for Neptune. The upper limit of the relevant temperature range is thus around 150K. Ar accretes onto a grain at temperatures not exceeding 30K; at higher temperatures the Ar will desorb before a trapping layer of ice can form on top of it. Accretion temperatures below 30K are thus considered.

The heating rate of the icy grains in the present scenario is around 100K over a period of 10^3-10^4 years, or 0.1K per year at most. Simulating this length of time is not feasible due to computational constraints. As an indication, the heating of a grain to 150K at a rate of 0.3K per minute takes several days to simulate. In our simulations, the lowest heating rate used is 0.3K per minute.

The regime of gas desorption which was observed from 80K to 130K in Figure 2.6 is the result of the gradual creeping of the ice which sporadically opens up gaps for the trapped species to desorb from. By using a higher heating rate, the time allocated to this regime is by extent lower. The amount of noble gas species desorbing is thus limited compared to the astrophysical case. This regime is more duration dependent than the desorption of multilayer and monolayer desorption, since the timescale for a particle to desorb is the inverse of the desorption rate presented in Equation 4.5. This timescale is several orders of magnitude smaller than the simulation timescale. Even for the higher heating rates considered, the noble gas atoms have sufficient time to desorb from the mono- and multilayer regime. The multilayer and monolayer regimes are thus covered adequately, even for the higher heating rates used in simulation. From Figure 2.6 it can also be inferred that the total gas released in the creeping regime is several orders of magnitude smaller than the gas released in the pure and monolayer desorption regime at lower temperatures. Indeed, subsequent work by Bar-Nun et al. [45] revealed that the total Ar gas released by the multi- and monolayer desorption regimes was a factor $10^{2.5}$ larger than the gas released by the creeping of the ice, for an evenly mixed water-Ar ice. For a more complex gas-water mixture, this factor was $10^{1.5}$. Both results indicate that the dominant desorption regimes which determine the final composition of the icy grain are those of multilayer and monolayer desorption.

It is noted that these experiments were conducted with heating rates comparable to those simulated in this work. The expected effect of using a lower heating rate is discussed in Section 5.4.1. Specifically, the amount of noble gas released during this creeping regime will be compared for different heating rates and will be extrapolated to the amount of material released in the realistic astrophysical scenario.

5.3. Results

Based on the derivations in previous sections, the simulations conducted to study the enrichment patterns in different formation and heating conditions are summarised in Table 5.2. In our simulations, ices are warmed up until a temperature of 150K in order to mimic the temperature at Jupiter. All these simulations used an ice thickness of 75Å, and a grid size of 100x100 points. As indicated, the results will be displayed in three different sets, where one variable is adjusted in each set. The variables adjusted are the deposition temperature T_d, the water to noble gas ratio r and the heating rate h. The fraction of the initially trapped noble gas material remaining after heating to 150K, F is shown in the rightmost column of the table.

The first set of figures used to analyse the results will now be briefly introduced. These figures will also be referred to in Section 5.4.

The first interpretation of the data is by computing the Ar/Kr and Ar/Xe ratios from de-

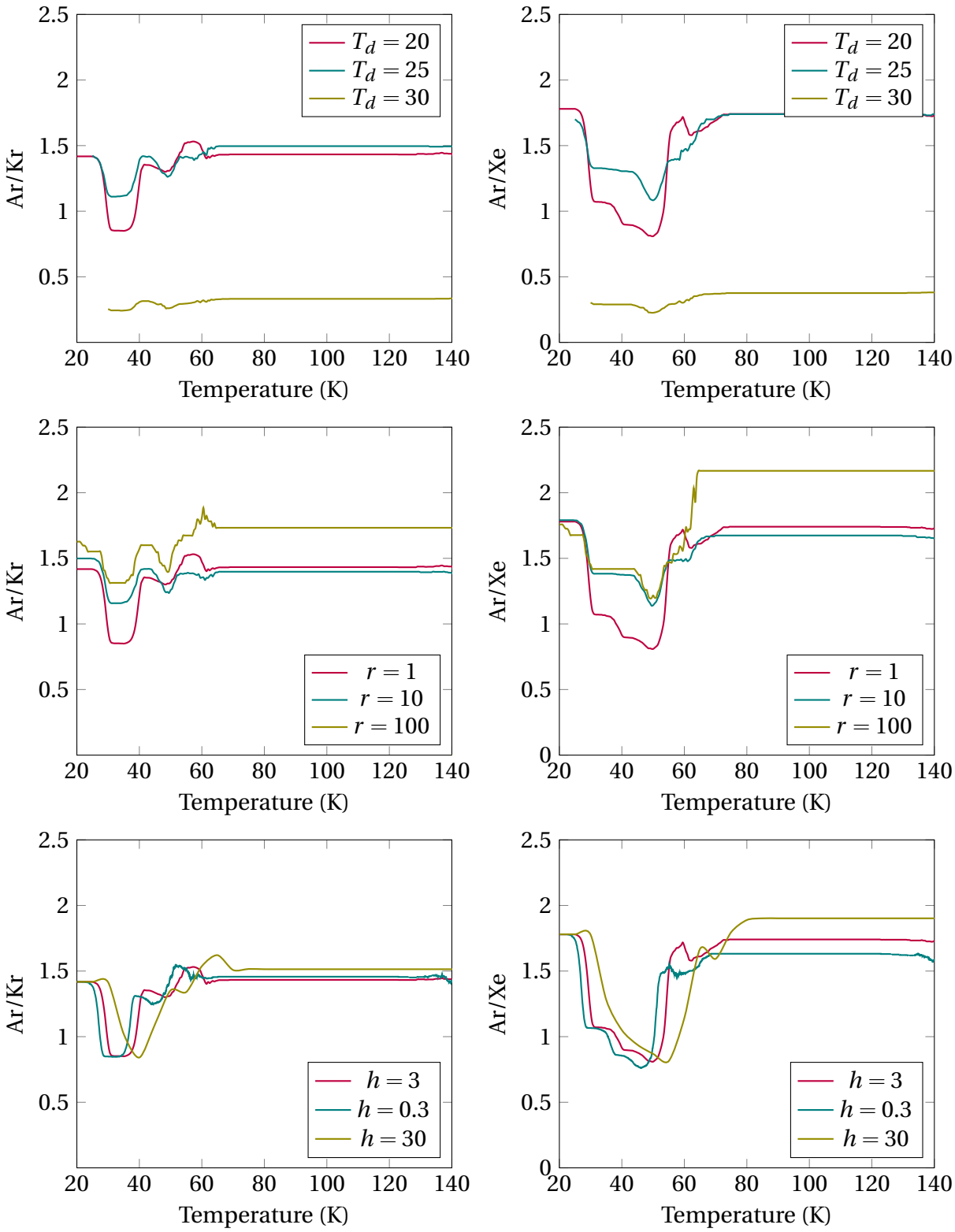

Figure 5.1: Evolution of the noble gas ratios as different ice samples are heated. Each row shows the results of adjusting one input parameter, as listed in Table 5.2. Top row: formation temperature [K], second row: water to noble gas ratio r, third row: heating rate h [K min^{-1}].

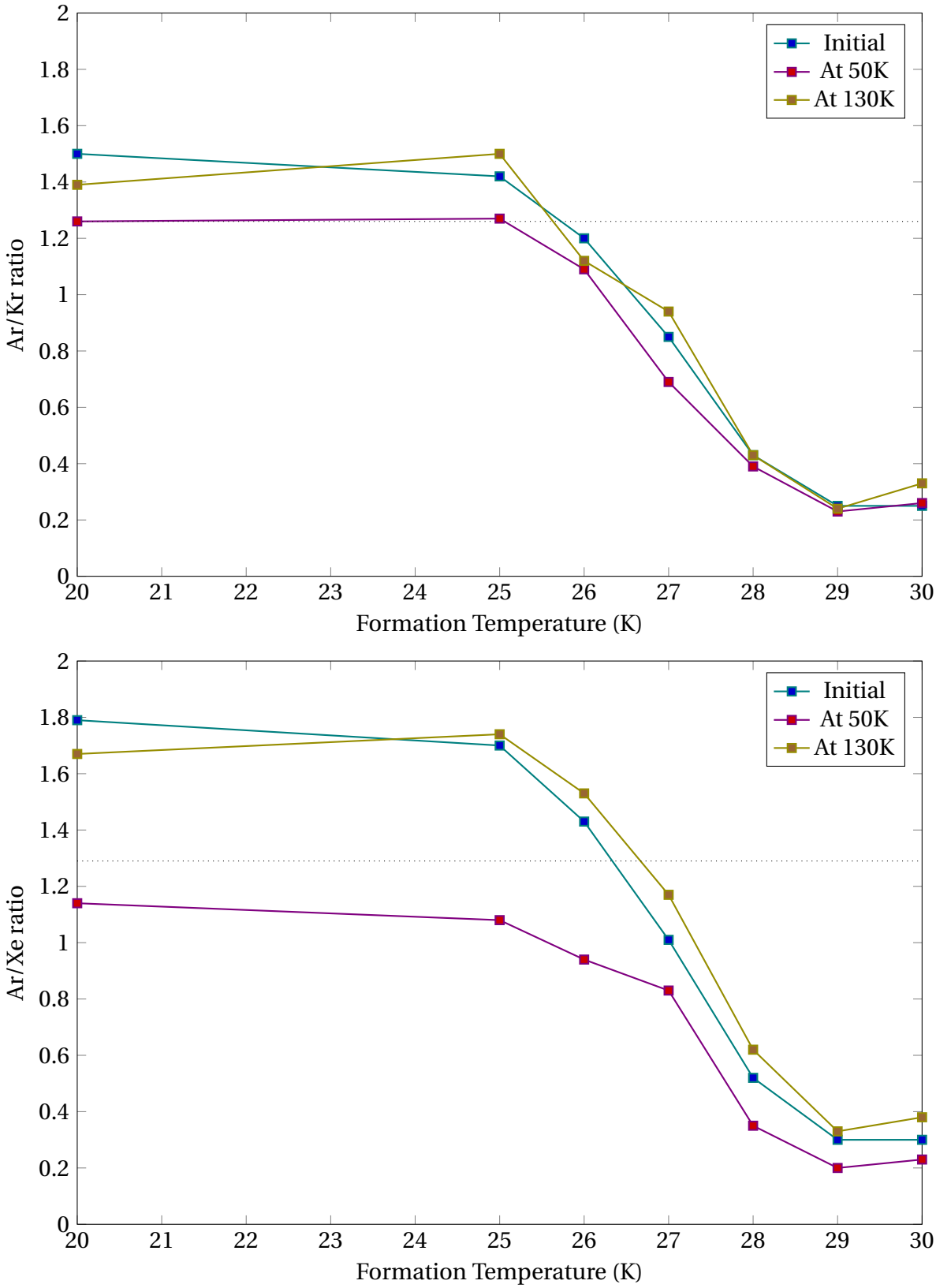

Figure 5.2: Noble gas ratios upon formation, at 50K (approximate temperature of Neptune formation) and at 130K (approximate temperature of Jupiter formation) for different ice formation temperatures. The values measured by Galileo on Jupiter is shown as a dotted line.

Table 5.2: List of simulations conducted to study planetary enrichment signatures.

Simulation	T_d [K]	r	h [K min^{-1}]	F
1	20	10	3	54%
2	**25**	10	3	21%
3	**26**	10	3	44%
4	**27**	10	3	20%
5	**28**	10	3	20%
6	**29**	10	3	32%
7	**30**	10	3	28%
8	20	**1**	3	41%
9	20	**100**	3	35%
10	20	10	**0.3**	30%
11	20	10	**30**	28%

position to the final temperature of 150K, shown in Figure 5.1. This is done for most of the simulations listed in Table 5.2. Simulations 1, 2 and 7 compare the different deposition temperatures T_d in the top row of Figure 5.1. For formation temperatures of 20K and 25K, all noble gas atoms stick to the ice. The initial Ar/Kr and Ar/Xe ratios are thus approximately equal to the ratios of the thermal velocities (1.45 and 1.81 respectively). This indicates the accretion process works as intended. As the formation temperature approaches 30K, some of the Ar already desorbs during formation, and both ratios are lower (<0.5) initially. For $T_d = 20$K and $T_d = 25$K, the Ar/Kr and Ar/Xe ratio is observed to decrease as the ice is heated. The minimum Ar/Kr occurs around 35K. At this temperature, the multilayer Ar has desorbed while both the multi- and monolayer Kr is still in the ice. As the Kr also begins to desorb around 35K, the Ar/Kr ratio returns to its initial value. The minimum Ar/Xe occurs around 50K. At this temperature, the multi- and monolayer of Ar has desorbed while both the multi- and monolayer Kr is still in the ice. As the Xe also begins to desorb around 50K, the Ar/Xe returns to its initial value. Because both ratios return to their initial values indicate that a comparable fraction of each noble gas species desorbed from the ice during the heating process.

Simulations 1, 8 and 9 to compare different water to noble gas ratios r in the second row of Figure 5.1. The deposition temperature for all these simulations was $T_d = 20$K. The initial Ar/Kr and Ar/Xe ratios are approximately equal to the ratios of their thermal velocities, as was also observed for $T_d = 20$K in the top row of Figure 5.1. The same minima of Ar/Kr and Ar/Xe at 35K and 50K respectively discussed for these results are also observed for the different r values used. The minima is more pronounced for a lower value of r. A low value r equates to a larger portion of the ice consisting of noble gas atoms. The noble gas atoms in deeper layers of the ice are thus less thoroughly trapped by water molecules, and can more easily desorb. A larger absolute amount of Ar desorbs between 30K and 50K for a lower r, but this is mirrored by a larger absolute amount of Kr and Xe desorbing at higher temperatures. The final ratios are thus comparable to their initial values, for both $r = 1$ and $r = 10$. For $r = 100$, the final Ar/Kr and Ar/Xe ratios are higher. In this simulation, relatively more Kr and Xe atoms desorbed. The number of noble gas atoms of each species simulated was of order 10^2. As a consequence, the resultant Ar/Kr and Ar/Xe ratios can change significantly with the desorption of each noble gas atom. The result of a single high r simulation

is not expected to provide binding indications of the final ice composition. This result is thus attributed not to a physical process, but rather to computational constraints.

Simulation 1, 10 and 11 to compare different heating rates h in the bottom row of Figure 5.1. The initial and final Ar/Kr and Ar/Xe ratios are comparable for all the heating rates considered. The minima of these ratios around 35K and at 50K are also observed for all the different heating rates. For the highest heating rate $h = 30$ K min^{-1}, these minima occur at a slightly higher temperature. This can be explained conceptually as follows. For a high heating rate, the noble gas atoms have less time to desorb in each temperature step, as less time is spent in this step before the temperature is increased. The minima are thus 'delayed' until a later time, and by extent a higher temperature.

The Ar/Kr and Ar/Xe ratios show a notable dip around 50K for ices accreted at 20-25K. To visualise this decrease, the ratios are shown at different temperatures in the simulation in Figure 5.2. This is done for each of the formation temperatures considered, shown on the horizontal axis. The ice thickness and heating rate of each of these simulations was 75Å and 3 K min^{-1} respectively. The ratios at the formation temperature are shown in blue. Below 25K, all noble gas atoms stick to the ice. The Ar/Kr and Ar/Xe ratios are thus approximately equal to the ratios of the thermal velocities. As the formation temperature approaches 30K, some of the Ar already desorbs during formation, and both ratios decrease as a result. The ratios at 50K are shown in violet. Between 30K and 50K some of the Ar has desorbed, while some of the Kr, and most of the Xe is still in the ice. The Ar/Xe in particular is thus lower. The ratios at 130K are shown in yellow. At this temperature, Kr and Xe has also desorbed from the ice. The ratios are thus comparable to their initial values.

5.4. Extension to solar system conditions

In this section, the results will be discussed from an astrophysical perspective. This section is structured as follows. First, the effect of the heating rate on the desorption is studied in Section 5.4.1. As discussed in Section 5.2.3, the heating rate used in simulations is lower than the astrophysical heating rates. The effect of this deviation is discussed. Next, the effect of ice thickness on the ice composition during heating is studied in Section 5.4.2. Then, based on Figure 5.1, two temperature ranges will be discussed. The first is the composition ratios at a temperature of 130K, at which Jupiter is located. The implications for Jupiter are presented in Section 5.4.3. The Ar/Kr and Ar/Xe ratios can be compared to the Galileo probe measurements. This provides insight into the conditions the ices that enriched Jupiter formed. Based on the results for different ice properties, an estimate is made of the ice mass needed to yield the current Jupiter enrichment. In Section 5.4.4, a second temperature range from 50K to 100K is discussed. This range is relevant to the planets Saturn, Uranus and Neptune. As can be seen in Figure 5.1, the Ar/Kr and Ar/Xe ratios may vary at lower temperatures which could lead to different atmospheric signatures on Neptune in particular.

5.4.1. Heating rate

In this section, consideration is given to the effect of the use of a relatively high heating rate. As discussed in Section 5.2.3, the potential effect of the creeping regime is diminished when it occurs over a shorter time period. To adjust for this effect we consider the simulated release of noble gas during this regime specifically, between 80K and 130K. These

limits are the point at which the monolayer desorption of all the noble gas species (namely Xe) has taken place, and the temperature at which Jupiter is located. For a heating rate of 0.3, 3 and 30K per minute, the number of noble gas atoms c released in the creeping regime is respectively 8, 3 and 0. These data points are visualised below in Figure 5.8. Several relations between heating rate h and c can be justified. For the purposes of this work, it must be reasonably concluded that using a heating rate lower than the astrophysical case does not invalidate the conclusions drawn from the simulation results. More specifically, the amount of particles expected to desorb from the ice in the creeping regime in the astrophysical case should not be so large as to fully deplete the ice of its noble gas.

In Figure 5.3, the amount of particles c desorbed in the creeping regime is shown for different heating rates. This refers to Simulation 1, 10 and 11 in Table 5.2.

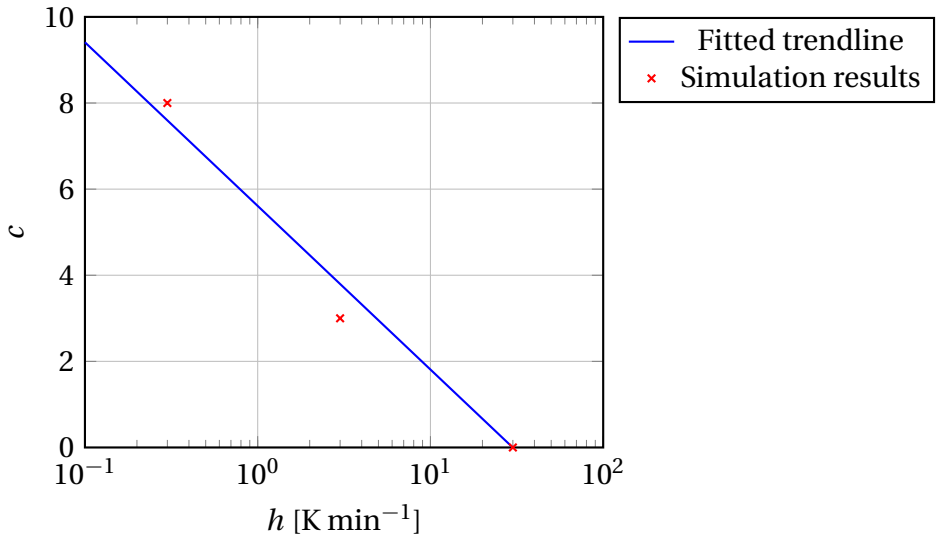

Figure 5.3: Evaluation of the effect of the heating rate h in K min^{-1} on the number of particles desorbed in the creeping regime c.

A trend of form $c = A + B\log(h)$ is evaluated here. This equates to the number of particles c desorbing in the regime increasing by an amount B for every factor 10 decrease in h. This is justified as follows. Desorption during the creeping regime is the result of noble gas atoms reaching the surface through diffusion. Recalling that the diffusion rate $\sim \nu$ from Equation 4.2, it is argued that a factor 10 decrease in h gives the noble gas atoms a factor 10 more time to diffuse through the ice. Since the direction of diffusion can be seen as a random walk across the grid, an increase in duration makes it more likely that noble gas atom deeper in the ice reach the surface. Based on the simulation results, it is thus inferred that a factor 10 decrease in h allows B more noble gas atoms to reach the surface.

The function is fitted using the intersection with the c axis as reference. That is, for $h = 30$ K min^{-1}, $c = 0$.

$$A = -B\log(30) \rightarrow c = B(\log(h) - \log(30)) \tag{5.7}$$

A least-squares fit of Equation 5.7 to the datapoints yields $B = 3.8$. The expression for c is then:

$$c = 5.6 - 3.8\log(h/30) \tag{5.8}$$

Evaluating Equation 5.8 for heating rates of 0.1 to 0.01K per year yields that $\approx 30-35$ atoms would have been released in this regime in for the expected astrophysical heating rates. This is considering an ice thickness of 75Å. These absolute values are expected to apply both to the ice thickness simulated and thicker ices, as the creeping affects mostly the atoms near the surface of the ice. Given that the initial number of trapped noble gas atoms in the ice is of order 10^3, the effect of the lower heating rate is thus acceptable.

The conclusions regarding the effect of the heating rate are thus twofold. First, the number of particles released in the creeping regime increases as the heating rate decreases. Second, the identified trend suggests that at the realistic astrophysical heating rates, the number of particles desorbed in the regime is significantly smaller than the number of noble gas molecules initially deposited in the ice.

5.4.2. Ice thickness

For both scientific and computational purposes the effect of a thicker ice on the desorption of noble gas is reviewed. To reduce the computational load, simulations are only performed with ice thicknesses of up to $\sim$ 250Å. However, the actual ice could be thicker depending on the budget of water vapour, as is explained in Section 5.2.1. A larger fraction of the trapped material is expected to be released from a thin ice, as the probability of a trapped atom coming to the surface is higher. This distinction is visualised in Figure 5.4. Extrapolating the results of thin ice simulations to thicker ices is done as follows.

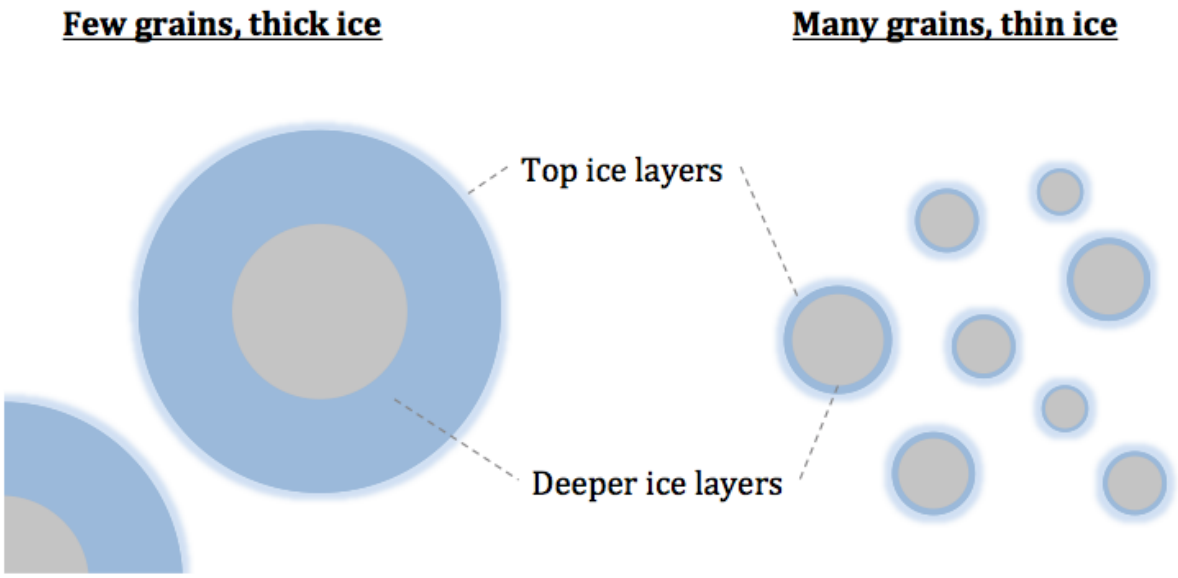

Figure 5.4: Different cases of particle size and ice thickness .

Suppose it is measured that from unit of thickness a fraction a of the initially deposited species desorbs. Then if two of those units were stacked, we would expect this same fraction a to desorb from the top unit, while a fraction βa diffuses upward into the first unit. β is a scaling factor to be determined based on simulation results. Of this diffused material, a fraction βa would then also desorb. In other words, a fraction $(\beta a)^2$ of the material contained in the second unit desorbs. Suppose n units are stacked on top of each other. By the same reasoning a fraction of $(\beta a)^n$ would desorb from the nth unit if stacked on top of

each other. Assuming each of the n units contains $1/n$ of the initially deposited species, the total fraction desorbed F is then:

$$F = \frac{1}{n}\left(a + \sum_{i=2}^{n}(\beta a)^i\right) = \frac{1}{n}\left(a + \sum_{i=0}^{n-1}(\beta a)^i - (\beta a)^0 - (\beta a) + (\beta a)^n\right) \tag{5.9}$$

Assuming $\beta a < 1$, a standard summation may be applied to the right hand side:

$$F = \frac{1}{n}\left(a + \frac{1-(\beta a)^n}{1-\beta a} - 1 - \beta a + (\beta a)^n\right) = \frac{1}{n}\left(a + \frac{(\beta a)^2 - (\beta a)^{n+1}}{1-\beta a}\right) \tag{5.10}$$

The parameter β is derived by fitting to a set of results. To derive an indicative value of β, a 1:10 Ar:H_2O mixture was deposited for a thickness of 1, 5 and 10 units. A unit in these simulations is equivalent to $\sim$ 25Å of ice thickness. After the pure ice desorption peak at around 30K, around 33% of the Ar has desorbed from the 1 unit thick ice, which provides the value of a. The parameter β is computed using a least-squares fit of the results for 5 units (12.1%) and 10 units (5.8%). The optimal β value is approximately 1.2. The fitted function and the simulation results are shown below.

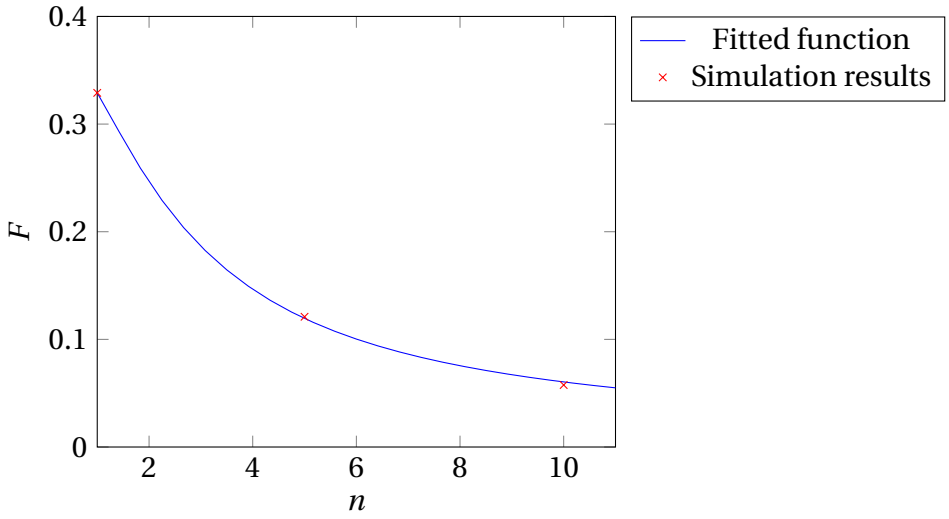

Figure 5.5: Fraction of Ar desorbed F as a function of the numbers of layers n, fitted with a least-squares fit.

The simulations will be performed with ice thickness of 75Å, whereas the ice could also be thicker, as is discussed in Section 5.2.1. The above methodology allows the simulation results to be applied to such scenarios.

The Ar/Kr and Ar/Xe ratios at a temperature of 50K are relevant for the planetary applications discussed in Section 5.4.4. In Figure 5.6, the extrapolated ratios at 50K are shown for thicker ices of 750Å, 3000Å and 6000Å. The simulated results of 75Å are shown, as well as the ratios at formation. As the thickness increases, the ratios approach their initial values, since desorption occurs mostly from the top layers of the ice. For a thin ice, this desorption thus has a larger effect on the average composition of the ice during heating.

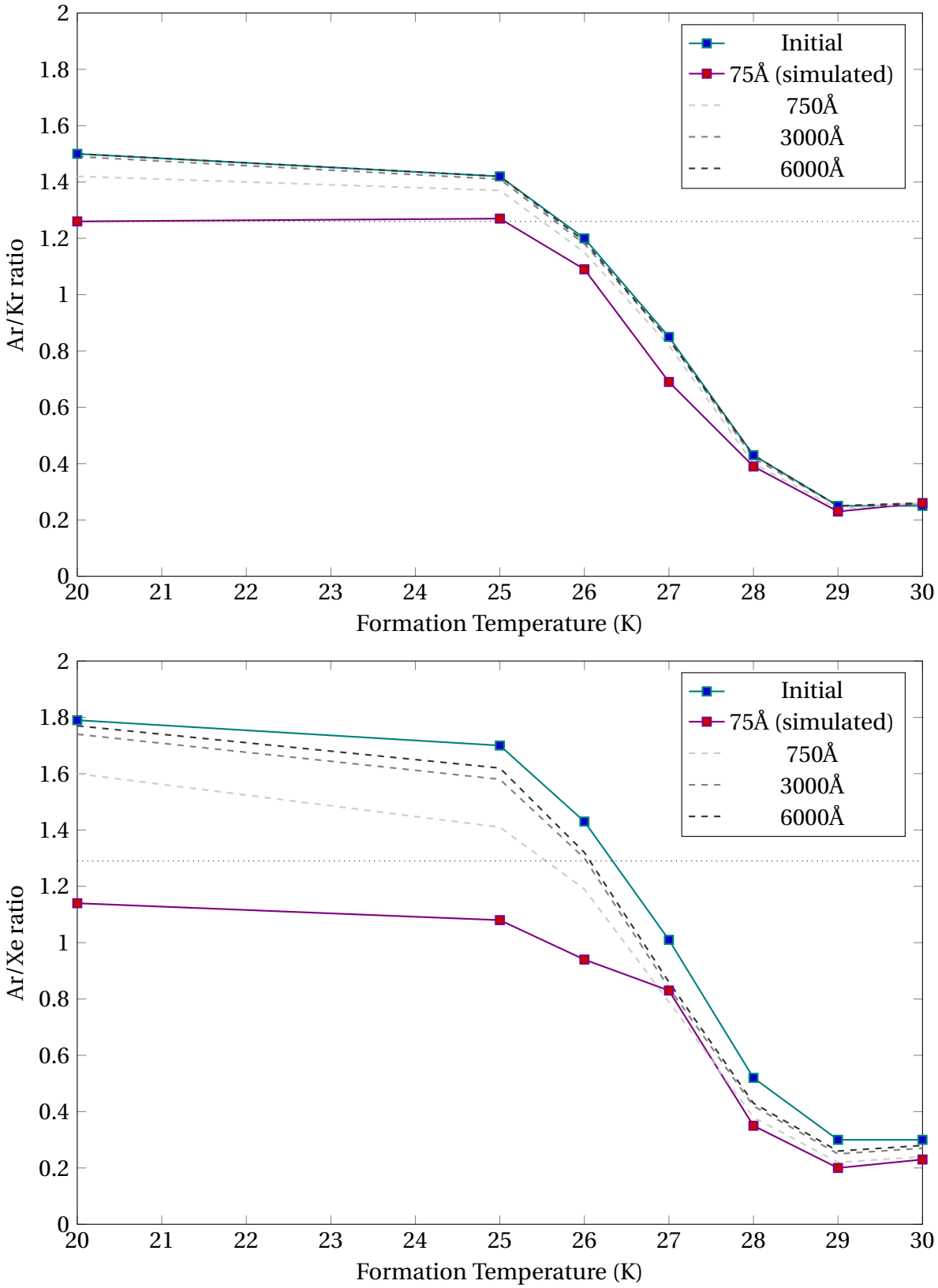

Figure 5.6: Noble gas ratios at 50K for the simulated 75Å ice (red line). The initial composition is shown by the blue line. The composition of thicker ices at 50K is extrapolated and shown with dashed lines. The values measured by Galileo on Jupiter is shown as a dotted line.

5.4.3. Jupiter

Atmospheric noble gas signatures

In terms of the enrichment of Jupiter, various ice formation conditions are consistent with the Ar/Kr and Ar/Xe ratio of 1.26 and 1.29 respectively measured by Galileo. At different formation temperatures, the accretion and desorption rates of each species differ. The accretion rate scales with $\sqrt{T}$ for all species, but the mass dependence of the thermal velocity by $\sqrt{m}$ means the accretion rate of Ar to Kr and Ar to Xe is 1.45 and 1.81 respectively.

At temperatures below 25K, none of the species readily desorb from the ice. The Ar/Kr and Ar/Xe enrichment ratios are thus near equal to the ratio of their thermal velocities. Ar begins to readily desorb from the ice during formation as the formation temperature approaches 30K. the Ar/Kr and Ar/Xe thus decreases, as can also be seen in the blue line in Figure 5.2.

The ratios measured on Jupiter correspond to a formation temperature of 25K-27K, as can be inferred from Figure 5.2. The ratios during heating for a formation temperature of 25K and 27K is shown in more detail in Figure 5.7. At the Jupiter temperature, the Galileo measurement for both ratios sits between what was observed in these two simulations. The formation of the ices is expected to have occurred in a region spanning a temperature range of 25K to 30K. The possibility of a wider temperature range cannot be dismissed. If the material was sourced from both low temperature regions, where Ar/Xe$\sim$1.8 and higher (above 30K) temperatures, where Ar/Xe$<$ 1, the average composition of the reservoir can still be consistent with the Galileo measurements. The thickness of the ice does not influence the conclusions drawn for Jupiter. The enrichment ratios are representative of the equilibrium between the accretion and desorption processes of each species during formation. As the rates of these processes are constant during the formation of the ice, the enrichment ratios of the ice are constant during the formation process.

From the results of simulations 1, 10 and 11 listed in Table 5.2, no apparent relation between the heating rate h and the fraction of material retained F can be deduced. The conclusions are thus assumed to hold for different heating rates. In addition, the creeping regime discussed in detail in Section 5.4.1 is not expected to influence the final enrichment ratios of the ice. The reason for this is that in the creeping regime, the desorption rate is comparable between the noble gas species. Any noble gas atoms that reach the surface of the ice in this temperature range immediately desorbs. Since this regime is driven by the diffusion of water molecules, there is no preference for the release of any particular noble gas species. The relative final abundances of the different noble gases is thus not expected to be impacted by a lower heating rate, and by extent a more prominent creeping regime.

Mass needed for enrichment

As is summarised in Table 5.2, less than 50% of the initially accreted noble gas material is released up to the expected Jupiter temperature of 130K for an ice thickness of 75Å. This implies that if the ice that delivered the noble gases to Jupiter behaved similarly, the initial accreted noble gas mass was more than a factor 2 as much as is found on Jupiter now.

Jupiter consists predominantly of hydrogen and helium, with those two elements accounting for 75% and 24% of its mass respectively. The total amount of hydrogen by weight is approximately 1.9×10^{27} kg, which translates to 1.9×10^{30} mol of H atoms.

Mahaffy et al. [26] reported an Ar abundance of 9.10×10^{-6} atoms per H atom on Jupiter, compared to 2.75×10^{-6} in the solar nebula. The Ar enrichment of Jupiter is thus approximately 1 Ar atom per 157×10^3 H atoms. Jupiter thus carries an excess 1.2×10^{25} mol of

Ar, which at a mass of 40 g per mol equates to 4.821×10^{23} kg or $0.08 m_\oplus$ of Ar. Examining Table 2.1, it can be seen that in the solar nebula, the molar ratio Ar/Kr$\approx 2 \times 10^3$ and Ar/Xe$\approx 2 \times 10^4$. The Ar:Kr:Xe ratio can thus be approximated by $2 \times 10^4 : 10 : 1$. If the enrichment is uniform, the enrichment in terms of number of moles of Kr and Xe is thus smaller by this factor. In the rest of this analysis, we disregard the mass contribution of Kr and Xe, by invoking the approximation:

$$(2 \times 10^4) m_{\mathrm{Ar}} + 10 m_{\mathrm{Kr}} + m_{\mathrm{Xe}} \approx (2 \times 10^4) m_{\mathrm{Ar}} \tag{5.11}$$

Where m_i is the molar mass of species i. The water needed to trap the noble gases, with a molar weight of 18 g, does however contribute to the mass of material needed. The molar abundance of H_2O would be at least as large as that of Ar. An H_2O:Ar ratio of 1:1, 10:1 and 100:1 increases the mass of the delivered material to 0.11, 0.44 and $3.70 m_\oplus$ respectively. A higher H_2O:Ar is considered unlikely given the abundances presented in Table 2.1. For the ice thickness simulated, the initial mass is thus between $0.53 m_\oplus$ and $8.31 m_\oplus$ for a gas:water ratio of 1:1 and 100:1 respectively. Using the derivations of Section 5.4.2, a thicker ice of 6000Å would release significantly less of the initially trapped noble gas, as is summarised below in Table 5.3. This thus reduces the initial mass required, to between $0.13 m_\oplus$ and $3.82 m_\oplus$ for an H_2O:Ar ratio of 1:1 and 10:1 respectively. The mass required for a combination of thinner and thicker ices would naturally fall in these two ranges. The ice masses computed are summarised in Table 5.3. Along the top row the different water to noble gas ratios considered are shown. The mass required for each ratio, assuming no noble gas desorbs from the ice between formation and deposition, is shown in the second row. Using the simulations results, the mass needed for an ice thickness of 75Å is shown in the third row. The masses computed for 750Å, 3000Å and 6000Å are computed by extropolating what fraction of the noble gas would be desorbed for this thickness, using the methodology of Section 5.4.2. For a given H_2O:Ar ratio, the mass required decreases for a higher average ice thickness. For a thicker ice, relatively less of the initially trapped noble gas desorbs, and a lower mass is thus required to provide the Jupiter enrichment. The masses computed are consistent with pebble accretion scenarios, which suggest the accretion of 1 to 10 Earth masses of pebbles [30]. The mass required for the amorphous ice delivery mechanism to deliver the measured enrichment cannot be higher than this upper limit of 10 $m_\oplus$. Only in the case of a thin ice and a high water to Ar ratio does the suggested mass approach this upper limit. Most scenarios presented in Table 5.3 suggest the measured Jupiter enrichment could have been delivered by less than $1 m_\oplus$ of amorphous water ice.

The effect of the heating rate is not considered in this analysis. The reasoning for this is as follows. As discussed in Section 5.4.1, the lower heating rate in the astrophysical scenario is expected to affect the creeping regime in particular. In the same section an estimate was made of the number of particles that would desorb in this regime for a realistic astrophysical heating rate. This number was of the order 10^2, while the total number of noble gas atoms initially trapped in the ice was of the order 10^4. The desorption during the creeping regime does not have a substantial effect on the noble gas abundance in the ice. This can also be inferred from the experimental results shown in Figure 4.6, which shows the desorption flux in the creeping regime is several orders of magnitude smaller than the desorption flux of the multi- and monolayer regimes. The masses presented in Table 5.3 are thus not adjusted for the potential effect of a lower heating rate.

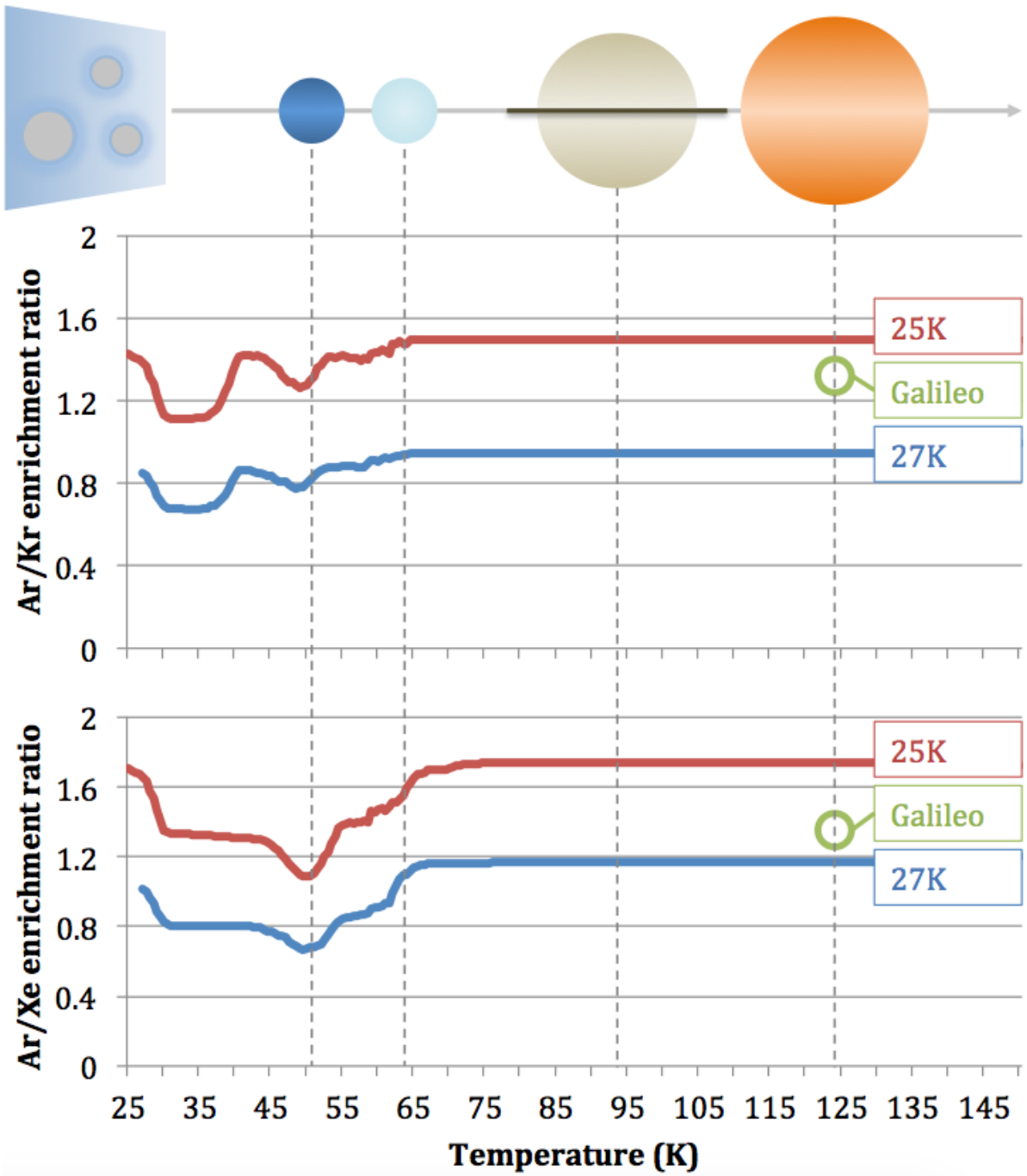

Figure 5.7: Evolution of the Ar/Kr (top) and Ar/Xe (bottom) ratio during heating of an ice formed at 25K (red line) and 27K (blue line). The formation temperatures of Neptune, Uranus, Saturn and Jupiter are indicated. The Galileo probe measurement at Jupiter is circled in green.

Table 5.3: Computed mass (in $m_\oplus$) of icy material needed for the observed Jupiter enrichment, for different water abundances and average ice thicknesses, in $m_\oplus$.

Ratio H_2O:Ar	1:1	10:1	100:1
Mass required (no desorption, $m_\oplus$)	0.11	0.44	3.70
75Å (simulated)	0.53	0.95	8.31
750Å	0.48	0.54	6.70
3000Å	0.15	0.46	3.95
6000Å	0.13	0.45	3.82

5.4.4. Saturn, Uranus and Neptune

Atmospheric noble gas signatures

As the temperature of the ice increases, Ar is first to desorb, followed by Kr and Xe. This order applies to all the ices, regardless of formation temperature or heating rate. In the low temperature range up to 50K, the ice is thus depleted of Ar compared to its initial composition. At 50K both multilayer Ar ice as well as monolayer of Ar on the water crystal has desorbed, while Kr and Xe remain frozen. This leads to the distinct dip in Ar/Kr and Ar/Xe as can be seen in Figure 5.1.

The feature is highlighted in more detail in Figure 5.2, where the Ar/Kr and Ar/Xe ratio at 50K is compared to the initial ratio and the ratio upon reaching Jupiter temperature. The initial ratios (blue line) obtained when ices form between 20K and 30K are compared to the ratio obtained when the ices are heated up to 50K (violet line) and up to 130K (yellow line). For Saturn, which was located at a temperature of ≈100K, the dip in Ar/Kr and Ar/Xe is not relevant. The atmospheric Ar/Kr and Ar/Xe signatures on Saturn are expected to be comparable to those measured on Jupiter. For the ice giants, and Neptune in particular, different atmospheric signatures could be expected, as is shown in Figure 5.7.

Figure 5.7 shows the temperature of the giant planets. The top and bottom panel respectively show the Ar/Kr and Ar/Xe during the heating that icy pebbles experience during their drift in the solar system after forming in cold regions (shown in the blue box on the top left). The highlighted results are of Simulation 2 and 4 in Table 5.2, which used a deposition temperature of 25K and 27K respectively. For the Neptune temperature of 50K [46], simulations show that the Ar/Xe ratio could be as low as 0.7 compared to the 1.3 observed on Jupiter. In that same simulation the Ar/Kr ratio is around 0.8 at 50K. This Ar depletion is not as apparent for Uranus. The atmospheric signatures in Saturn are expected to be the same as that of Jupiter. Its temperature around 100K is higher than the 80K up to which the ratios undergo notable change.

Effect of ice thickness

The inferences of the previous section apply to the ices simulated. The actual thickness of the ice could have been higher than what was simulated, as is discussed in Section 5.2.1. For thicker ices, the higher volatility of Ar would have less effect on the bulk composition of the ice. This is because for a thick ice, atoms trapped in deeper layers of the ice have a smaller chance of reaching the surface from where they can desorb. This distinction was visualised in Figure 5.4, which shows the cases of few particles with thick ice and many particles with thinner ices.

The volatile species desorb primarily from the top layers of the ice. For a thin ice, this

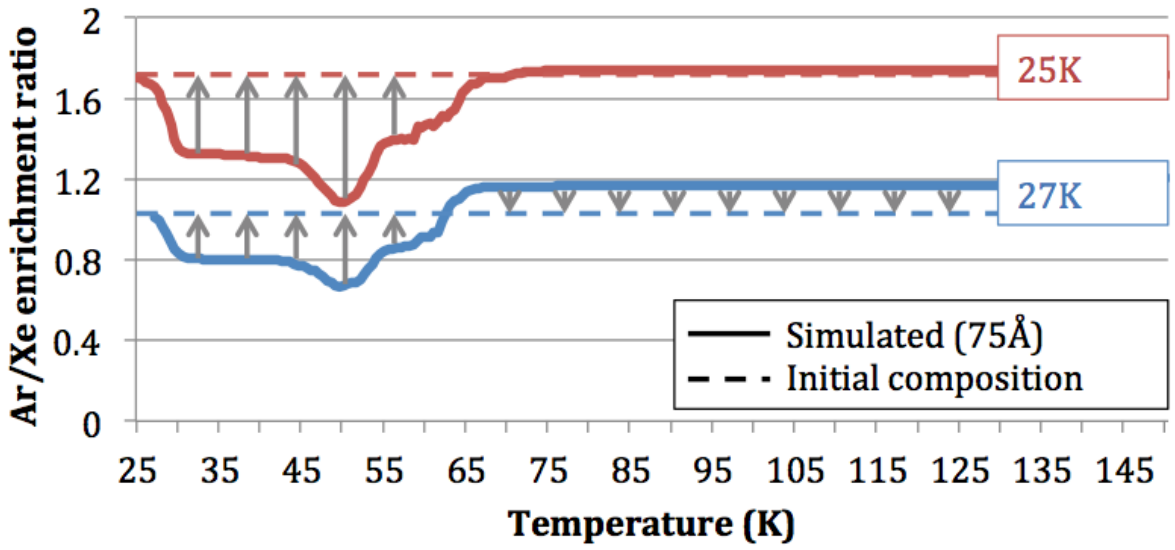

Figure 5.8: Evolution of the Ar/Xe ratio during heating of an ice formed at 25K (red line) and 27K (blue line). The evolution is compared to the initial ratio, shown as a dashed line. The grey arrows indicate the dampening of the features as the ice thickness is increased.

desorption thus has a larger effect on the average composition of the ice. For a thick ice, the average composition is affected less. This is visualised in Figure 5.6, where the Ar/Kr and Ar/Xe ratio are extrapolated for different ice thicknesses. As the thickness increases, the ratios approach their initial values at formation. The atmospheric signatures on Neptune and Uranus are thus expected to be comparable to their initial ratios for thicker ices. To illustrate this, the Ar/Xe ratio shown in Figure 5.6 is compared to the initial ratio in Figure 5.8. The initial ratio is shown as a dashed line. If the ice thickness is increased, the Ar/Xe will be roughly constant during the heating. The dashed line is thus indicative of the limit of an 'infinitely thick' ice, the composition of which would be unaffected by the heating process. The dampening of the Ar/Xe dip as the thickness is increased is shown by the grey arrows. The same dampening of features is expected for the Ar/Kr ratio. The enrichment signatures of planetary atmospheres thus depends not only on how much enriched ice was accreted by the planet, but also how thick the ice was on average.

5.5. Contribution to body of knowledge

In this section, the findings of our simulation results will be compared to previous works on amorphous water ice as an enrichment mechanism. The atmospheric composition of Uranus and Neptune is an active field of study. A lack of in-situ measurements means the atmospheric composition of these planets remains largely unknown, but have been proposed as a priority for future missions [47][8].

In Figure 5.9, the expected enrichment pattern delivered to Uranus and Neptune by amorphous water ice is compared for other mechanisms, as reported by Atreya et al. [8]. The amorphous water ice enrichment pattern in the pebble accretion model is shown by the red line. Amorphous ice is suggested to deliver a uniform enrichment of the noble gas species listed on the horizontal axis. This pattern is based on the assumption the uniform capture of the species listed. This requires an ice formation temperature of <30K [29], as was also considered in the present work. The results presented in Section 5.4 showed that

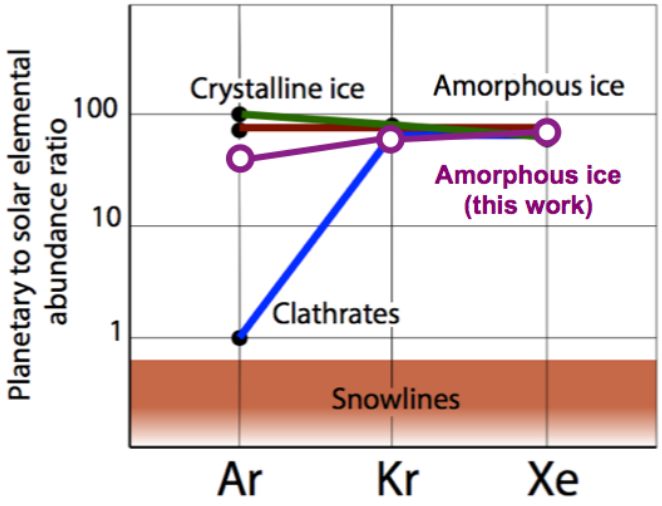

Figure 5.9: Enrichment patterns expected for different delivery mechanisms. Original figure by Atreya et al. [8]; purple enrichment pattern has been added based on the findings of this work.

the noble gas signatures can be non-uniform. The different accretion rates of the different species means the initial Ar/Kr and Ar/Xe will be roughly equal to the ratio of their thermal velocities (1.45 and 1.81, respectively) for formation temperatures <25K, as was shown in Figure 5.2. In addition, the enrichment patterns can change during the heating which the ice would undergo during inward drift. In particular, Ar desorbs readily from the ices in the 30K to 50K temperature range, while Kr and Xe are less volatile. The change in the ratios during heating is highlighted in Figure 5.7. A notable highlight is the possible Ar/Xe ratio of 0.7 at a temperature of 50K. An indicative atmospheric signature provided by amorphous water ice based on the results of the present work is shown in purple. This is representative of the ice with formation temperature 27K heated to 50K, the results of which are shown in, among others, Figure 5.8. The enrichment ratios Ar/Kr and Ar/Xe of 0.7 and 0.8 respectively (and by extent, Kr/Xe of $\sim$ 0.9) are applied to the absolute enrichment of Xe proposed in the original figure. As can be seen, this enrichment pattern differs from the uniform composition currently expected from amorphous water ice.

An Ar/Xe ratio <1 is also expected for the clathrate delivery mechanism, as shown by the blue line in Figure 5.9. Ar is trapped less effectively in clathrates than Kr and Xe [48], and would thus be underrepresented by this mechanism. The stability of clathrates in PSN is, however, still a topic of debate. In these environments molecular diffusion is near-zero preventing the formation of cage structures. Until recently there was no report of clathrate existence in conditions of relevance to space [49]. However, it has since been argued that the detection of infrared patterns attributed to clathrates could also be attributed to amorphous water ice [50]. Clathrates would also have delivered a water enrichment to the planets, which translates to an excess of oxygen (O) in their atmospheres. This water enrichment was not explicitly addressed in this work. Also not studied in this work is the enrichment patterns of Carbon (C/CO) and Nitrogen (N). The volatility of these species in the temperature ranges simulated suggest these species could also leave distinct signatures in planetary atmospheres. This is discussed in more detail in Section 6.3.2.

The present work has highlighted the non-uniformity and temperature-dependency

of the noble gas enrichment patterns that amorphous water ice could have delivered to the gas giant planets. This is an addition to current understanding, which simplifies the formation and desorption processes that affect the composition of amorphous ice in the protoplanetary disk. Our results have shown that the enrichment signatures delivered by amorphous water ice are dependent on a variety of factors. The formation temperature determines how much of each noble gas is trapped initially. The average ice thickness influences how much of the trapped noble gas desorbs during heating, and by extent the ice composition's sensitivity to this heating. The temperature to which the ice is heated, particularly in the 30K to 50K temperature range, can alter the Ar/Kr and Ar/Xe atmospheric signatures deposited in the planets. These observations must be taken into consideration in the review of eventual probe measurements of Uranus or Neptune.

5.6. Summary

In this chapter, a Monte Carlo approach has been applied to the simulation of amorphous water ice. The results showed consistency with the measured Galileo probe findings, suggesting a low temperature origin of the amorphous water ice that could have enriched Jupiter. The results were then applied to other giant gas planets. The scientific conclusions from these findings are summarised below.

Under several formation conditions, the simulations replicate the Ar/Kr and Ar/Xe ratios measured by the Galileo probe. A formation temperature between 25K and 27K best fits the Jupiter results. In this temperature range, virtually all the Kr and Xe accreted by the ice is retained, while some of the Ar desorbs before it can be trapped.

As the ice is heated to the temperatures at which Jupiter is located ($\sim$ 130K), the noble gases may desorb from the ice. Desorption occurs largely from the top layers of the ice. The composition of the deeper layers of the ice is not affected by the heating. For thicker ices, the effect of heating on the composition of the ice is thus less. For thicker ices, the initial composition of the ice is roughly maintained over the course of heating. Because a comparable fraction of each species desorbs during the heating to 130K, the final Ar/Kr and Ar/Xe ratios are the same as at the point of formation, regardless of the thickness of the ice.

For thin ice layers (<100Å), the different desorption temperatures of the noble gas species can have a notable effect on the composition of the ice. As the ice is heated, the Ar will be first to desorb. At higher temperatures, Kr and Xe also desorb. The planets Neptune, Uranus and Saturn are located at lower temperatures than Jupiter. Saturn has a temperature at which the composition of the delivered enriched ice is expected to be the same as those delivered to Jupiter, regardless of the ice formation conditions. Neptune and Uranus are different cases, due to their lower temperatures of $\sim$ 50K and $\sim$70K respectively. At Neptune temperatures, Ar will have desorbed from the ice, while Kr and in particular Xe is still retained. The Ar/Xe ratio could thus be significantly lower on Neptune if the enriched ice was delivered in thin layers. A note is made here regarding the different desorption mechanisms presented in Figure 2.2. The delivery of enriched clathrates, which trap Ar relatively poorly, could also lead to the observation of a lower Ar/Xe ratio. The delivery of thin amorphous water ices would thus not be the only explanation for an Ar/Xe ratio <1 on Neptune.

The scientific conclusions can thus be summarised in two key points. First, the simulations show that the delivery of amorphous water ice, under different formation conditions, could have provided the observed enrichment of Jupiter with noble gases. Second, for thin

ices, the Ar/Xe can be notably lower (0.7) at the Neptune temperature, while the Ar/Kr ratio is slightly higher ($\approx$ 08). This finding can be considered during the interpretation of future probe measurements of the ice giant planets, and Neptune in particular. If the Ar/Kr and Ar/Xe ratios are indeed lower than on Jupiter, the delivery of enriched amorphous ice remains a possible delivery mechanism. If amorphous water ice was the carrier, it must have formed in thin layers of less than 100Å.

6

Recommendations

6.1. Introduction

This chapter is a critical reflection of the work undertaken in this report. During this work, several issues and possible extensions of the chosen approach were identified. The limitations of the numerical method used are discussed in Section 6.2. Based on these limitations, a handful of suggestions for future work are made in 6.3. This includes both an experimental approach, as well as suggestions for improving the Monte Carlo method.

6.2. Limitations

This chapter is concluded with a critical review of the limitations of the numerical approach taken to study noble gas entrapment and retention. Because the physical processes which are modelled here occur on an atomic scale, the required input parameters are measured through complex experimental methods. The input parameters often have an interdependence, which can be difficult or impossible to discern from only desorption flux. For example, the binding energy and the pre-exponential factor are both components of the desorption flux, but only the actual flux can be measured. This flux, in terms of number of atoms detected, is in turn several orders of magnitude larger than what can feasibly be modelled in this study. Thus, while the benchmarking of the model was thorough and largely replicated experimental results, the numerical approach presented in this chapter carries inherent limitations. These limitations and their scientific implications are discussed below.

From a scientific perspective, the limitations regard the assumptions which must be made regarding the movement of particles onto, within, and from the ice. The likelihood of a particle being trapped in an amorphous water ice depends on both how long an accreted particle resides on the surface and how quickly the trapping layer forms on top of it. The residence time of an atom on the ice is dependent on a multitude of factors including its volatility, its physical size, the interactions with the dangling OH-bonds of the water, as well as its mass [37]. Through the binding energy and the pre-exponential factor these different factors are captured, but it is noted that these two parameters are constant and might be too simplified in a numerical approach. In addition, assumptions are needed to describe the binding energy of noble gas atoms to other species of noble gas, as no experimental data is available on this. The movement of particles within the ice is perhaps oversimplified by the rigid grid which is imposed on the particles. Off-lattice Monte Carlo simulations have

also been performed, in which the particle locations are determined explicitly, rather than set at the beginning of the simulation [51]. The presence of foreign species or temperature changes are not able to alter the tetrahedral structure of the surrounding ices. Given that water ice has been observed to undergo structural changes [5] as well as form clathrates around certain species [31], this rigidity could lead to a deviation from actual trapping ability. Enabling the re-ordering of molecules lies outside the scope of this work.

From a computational perspective, a numerical approach imposes limitations on how closely astrophysical conditions can be replicated. The simulation of each additional particle's movements increase the computational load. For each particle, the probability of movement or desorption is computed. In the case of movement, all possible directions are considered, each requiring the calculation of the binding energy at that destination. Considering that the pre-exponential parameter or attempt rate of all the species considered is of order 10^{11}-10^{14} per second, even simulations of just a few particles over a short time scale requires a large number of calculations. For this reason, the number of particles considered is just a fraction of what would be used in a modest experimental setup. The simulations work with a number of particles to the order of 10^4, with a surface area of just $\sim 10^5$Å^2. For the same reasons longer time scales are difficult to simulate. In the simulations presented the heating rates of the ice are of order 1K min^{-1} whereas the drifting enriched ice particles would be heated at a rate of around 1K per thousand years. Since the number of calculations required scales linearly with simulation time, such lengths are not attainable. This limitation is partially compensated for by the studying of the influence of different heating rates as discussed in Section 5.4.3.

6.3. Future work

To conclude this chapter, several topics for future study are addressed. These suggestions are consistent with the limitations identified in Section 6.2. In Section 6.3.1, an experimental approach to verify the conceptual findings of this study is presented. Sections 6.3.2 and 6.3.3 introduce two scientific additions to the model which can widen the range of possible astrophysical applications.

6.3.1. Experimental approach

As part of this thesis, experiments were planned to be conducted at the laboratory of University Cergy-Pontoise using the FORMOLISM (FORmation of MOLecules in the ISM) apparatus. The experiments study the interaction between water ice and noble gases, as well as other relevant species, in extreme low temperature and pressure conditions. More specifically, the competition between different species for binding sites in the accretion phase is to be tested. In addition the formation of clathrates around noble gases could be experimentally tested. This cage-like structure could not be simulated. The following experimental procedure for noble gas mixture trapping will be taken:

1. Formation of gas mixtures: gas mixtures with different abundances of noble gases as well as other volatiles (C, CO, N) will be created. The composition of these gas mixtures could resemble those simulated in this work, i.e. Ar:Kr:Xe ratios of 1:1:1.

2. Each gas mixture is tested under different temperatures, in the range of 30-90K. The substrate will be cooled to the desired temperature, after which the gas is admitted. The pressure of the chamber is then lowered to a low pressure, down to $\sim 10^{-10}$ mbar.

3. After a period of 12 hours the excess gas in the chamber is evacuated. The formed ice is then rested for 12 hours, with IR measurements around the wavelengths of the noble gases taken every hour. This is to test for the signatures of gas trapped in amorphous ice, and potential clathrate formation, as has been reported by Gosh et al. [49]

4. After the resting period, the ice is heated at 1K/min to 200K. During this time the flux of water and each noble gas will be measured. In addition, IR measurements are taken to test for clathrates as often as possible, ideally every minute.

The sample holder is gold-coated, and mounted onto a closed-cycle He cryostat. The infrared measurements are conducted using a Fourier Transform InfraRed Spectrometer (FTIRS), and a quadrupole mass spectrometer (QMS) will be used to measure the flux of the different noble gases during heating. The full setup of the FORMOLISM apparatus is shown in Figiure 6.1 [9].

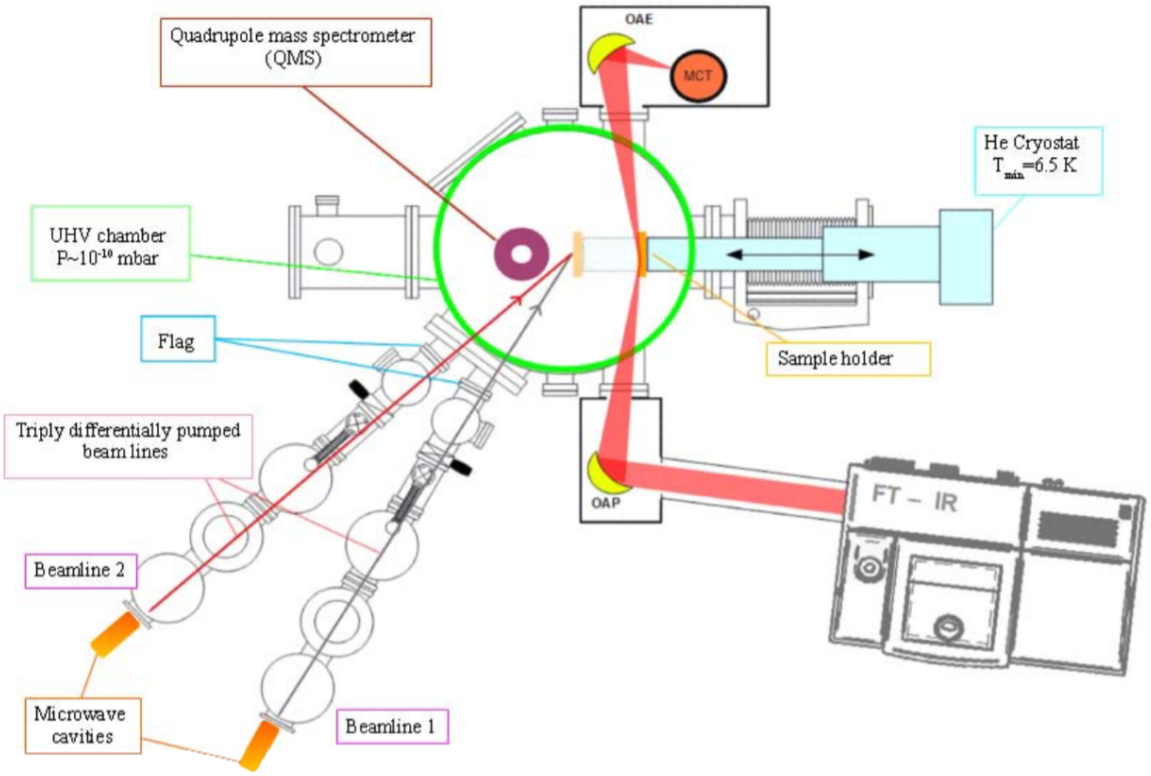

Figure 6.1: Schematic of the FORMOLISM apparatus [9].

6.3.2. Inclusion of CO

In this work, the noble gas species Ar, Kr and Xe were considered in an amorphous water ice structure without any impurities. These species were selected based on their low reactivity, and the availability of an in-situ measurement of their abundances on Jupiter. As can be inferred from Table 2.1, the accreted ice layer is likely to have contained many other species. These impurities could affect the retention and subsequent release of the noble gas atoms from the ice.

A species that is of particular interest is CO, which is relatively abundant in the nebula gas phase. The accretion of a significant portion of the CO reservoir could thus materially alter the composition of the ice. In addition, the CO competes with the noble gas species for suitable binding sites, as observed in experimental work [5]. The desorption energy of CO in CO and oxygen ices has been estimated to be around 850K [52], suggesting an accretion and desorption temperature scale comparable to Ar. The noble gases would thus have to compete with CO for binding sites at the formation temperatures considered in this work. The composition of the ice crystal could thus be affected, even before it is heated during its inward migration.

CO is thus recommended as a focus for future work. By using a gas mixture including both CO and noble gases, the effect of this species can be tested. If CO competes for binding sites with noble gases, the noble gases would tend to weaker binding sites. Their release from the ice would thus occur at lower temperatures. This could influence the composition of the ice, particularly in the 50K-70K temperature range discussed in Section 5.4.4. The study of CO is recommended in favour of the noble gas Neon, which would be a natural extent of this noble gas study. Neon is more readily influenced by atmospheric processes [27]. The abundance of Neon in an atmosphere thus provides less indication of the source material.

6.3.3. Isotopic differentiation of noble gases

In this work, only the most common isotope of each noble gas was considered. The atomic mass was thus constant for any particular species. In reality, the noble gases occur in different isotopes, with different masses and sizes. The different isotopes can be detected with a mass spectrometer flux measurement, as was proposed in the experimental approach in this Chapter. Including different isotopes in the numerical and experimental approach would allow for further benchmarking of the model, as well as widen the possible astrophysical applications. These improvements are discussed below.

In Section 6.2 the limitations of the model with regards to the accretion process were discussed. In the current setup, the accretion process captures only the species atomic mass, and by extent its thermal velocity. Different isotopes of the same element would thus have slightly differing accretion rates, and all else being equal have differing abundances in the resultant ice crystal. The residence time of a species in an amorphous ice pore can be affected by a variety of factors, of which the species mass is one. Factors such as atom size and reactivity are not currently considered during the accretion process. These factors affect the residence time, and by extent the trapping probability, of a species in a pore. Between different noble gas species, properties such as mass and atom size differ greatly. Whether the model accurately captures the influence of these factors is thus difficult to conclude based on only the results of different species. Between different isotopes however, these differences are more nuanced, with mass and size differing by only a few percent. If the different accretion and release rates can be accurately replicated on an isotopic scale, the robustness and the applicability of the model improve notably.

Isotopic composition is of interest to the study of solar system comets. The 2014 ESA mission to comet 67P by the Rosetta spacecraft provided substantial insight into the comet's origins. Flyby's through the comet's coma allowed for spectrometry measurements, during which isotopes of Ar, Kr and Xe were detected. A recent study by Rubin et al. [10] of this measurement data revealed that the isotopic abundances of Ar and Kr in the coma resem-

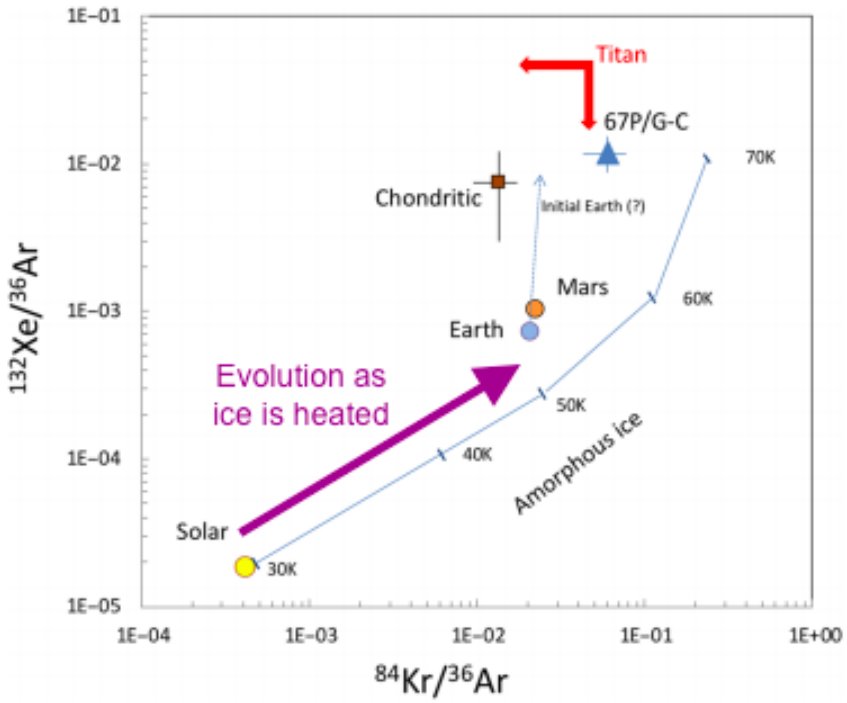

Figure 6.2: Isotopic composition of different solar system bodies [10]. The purple arrow has been added to the original by Rubin et al.

bled solar values, while the Xe isotopic composition notably differed. In addition to the relative abundance of the species themselves, their isotopic distribution thus provides even further indications of the material's origin. As is noted in the same study, the release of volatile species over long time scales could alter the (isotopic) composition of the material. These insights are summarised in Figure 6.2. The blue line indicates the isotopic composition of amorphous water ice formed at different temperatures. However, it has been shown in the present work that this composition need not be constant. The purple arrow has been added to illustrate the findings of the present work: the change in composition as the ice is heated. It is noted that the composition of the ice could not be simulated on the scale of the ratios shown here, due to computational constraints. Measurements of the release rates of the different isotopes, both through simulation and experiments, would thus be useful for explaining enrichment or depletion of a specific isotope in a solar system body.

In addition, the work discusses the potential contribution of amorphous water ice to different solar system bodies. The key parameter driving the noble gas composition of this amorphous ice considered is formation temperature. As has been shown in this work, heating of ices formed at low temperatures can alter their noble gas composition. The ratios at which different (isotopes of) noble gases are found in a body could not indicate only at which temperature the contributing material formed, but also to which temperature it was heated. This in turn would provide insight into the distance from the Sun at which the material was captured.

7

Conclusions

In this work, the role of amorphous water ice in the noble gas enrichment of Jupiter, and its implications for other giant gas planets, was studied. Using a Monte Carlo approach, the behaviour of noble gases in amorphous water ice was simulated, and applied to the topic of atmosphere formation. To conclude the report, the key findings are summarised below.

The current body of research was addressed in Chapter 2. This began with a fundamental understanding of the formation of planets from a disk of grains and gas. The formation of enriched water ices in the outer region of the disk was discussed, and introduced as a potential mechanism for delivering volatile species to the forming planets. The delivery of these enriched grains would leave behind signatures in the atmospheres of the planets. A high level of noble gases was measured on Jupiter by the Galileo probe. Due to the different volatilities of the noble gas species, they are released from the ice at different temperatures. Given that the grains could be heated up to 130K between formation and deposition on Jupiter, the composition of the grains could change between formation and deposition. This change in amorphous ice composition, and its implications for planetary atmospheres, was identified as a knowledge gap for study in this report.

Chapter 3 provided several experimental datasets of amorphous water ice and noble gases deposited at temperatures below 30K. These results were used to validate the Monte Carlo approach introducted in Chapter 4. By replicating experimental conditions, the effectiveness of the model was tested. Experiments have shown that volatile species desorb from amorphous water ice in different regimes. The accretion site of a volatile species influences if and at what temperature the species would be released from the ice. Three regimes were of particular interest: the desorption of noble gas atoms bound to other noble gas atoms, the release of noble gas bound to water ice, and the release of noble gases due to the gradual creeping of the water ice. The validation simulations replicated these three regimes for the different noble gas species. In addition, the different species each desorbed from the ice at the temperatures expected from experimental results.

The approach was applied to the topic of planetary atmospheres in Chapter 5. The conclusions from these planetary applications will be summarised here as they pertain to the research questions identified at the end of Chapter 2.

Our simulations show that the composition of an amorphous water ice is dependent on the formation temperature of the ice. For temperatures below 25K, the ratios Ar/Kr and Ar/Xe are equal to the ratio of their accretion rates. As the formation temperature

increases, Ar begins to desorb during formation. Both ratios thus decrease as the formation temperature increases between 25K and 30K. As the ice is heated after formation to 130K, the noble gas species are observed to desorb from the ice. This desorption occurs mostly from the top layers of the ice; the effect of desorption on the ice composition is thus less for thicker ices. A higher ratio of water to noble gas means the noble gas will be better trapped in the ice, but increases the mass of enriched material needed to deliver the enrichment measured by Galileo to Jupiter.

As the ice is heated to 130K, all species of noble gas are observed to desorb from the ice. The fraction of the initially trapped noble gas that desorbs is approximately equal between the different species Ar, Kr and Xe. The final composition of the ice in terms of Ar:Kr:Xe is thus comparable to the composition at formation. However, the temperatures at which the desorption of each species peaks differs, as was also observed in previous experimental work. Ar is the most volatile species and readily desorbs between 30K to 50K. Kr and Xe are less volatile and largely remain in the ice in this temperature range. The Ar/Kr ratio and, more notably, the Ar/Xe ratio thus show a dip at 50K.

The simulations show that the delivery of amorphous water ice, under different formation conditions, could have provided the observed noble gas enrichment ratios of Jupiter. For several scenarios of average ice thickness and water to noble gas ratios, the suggested mass of enriched icy material required is computed to be less than $1 m_{\oplus}$. Similar Ar/Kr and Ar/Xe ratios are expected to be observed on Saturn and Uranus, which were located at temperatures of $\sim$ 95K and $\sim$ 70K respectively. If the enrichment was delivered in amorphous water ices with thickness $<$ 100Å, an Ar/Xe atmospheric signature lower than the one observed on Jupiter is expected for Neptune, which was located at a temperature of 50K. This finding can be considered during the interpretation of future probe measurements of the ice giant planets, and Neptune in particular. If the Ar/Xe ratio is measured to be lower than on Jupiter, the delivery of enriched amorphous ice is a very possible scenario for the delivery of noble gases in gas giants planets. A lower Ar/Xe ratio could also be explained by the delivery of enriched clathrates. Clathrates trap Ar relatively poorly, as was discussed in the final sections of Chapter 5. Such a signature is thus not be an indicator of thin amorphous water ice delivery exclusively.

In Chapter 6, thorough consideration was given to the limitations of the approach used in this work. The numerical approach used was, in certain respects, a simplification of the processes that occur in amorphous water ices. In addition, the number of particles that could feasibly be simulated was less than the number of particles that would cover an icy grain. The incorporation of CO and different isotopes of noble gas were identified as possible extensions of the numerical approach. In addition, an experimental method was proposed, which would address the simplified approach to ice formation used in this work.

Bibliography

[1] Thomas Henning and Dmitry Semenov. Chemistry in protoplanetary disks. *Chemical Reviews*, 113(12):9016–9042, 2013.

[2] Nikhil Monga and Steven Desch. External photoevaporation of the solar nebula: Jupiter's noble gas enrichments. *The Astrophysical Journal*, 798(1):9, 2014.

[3] Michael L Allen. Astr450 life in the universe. http://astro.wsu.edu/allen/courses/astr450/Assignments/a6_f05.html, 2005.

[4] Peter Woitke, Inga Kamp, and W-F Thi. Radiation thermo-chemical models of protoplanetary disks-i. hydrostatic disk structure and inner rim. *Astronomy & Astrophysics*, 501(1):383–406, 2009.

[5] A Bar-Nun, J Dror, E Kochavi, and D Laufer. Amorphous water ice and its ability to trap gases. *Physical Review B*, 35(5):2427, 1987.

[6] R Scott Smith, R Alan May, and Bruce D Kay. Desorption kinetics of ar, kr, xe, n2, o2, co, methane, ethane, and propane from graphene and amorphous solid water surfaces. *The Journal of Physical Chemistry B*, 120(8):1979–1987, 2016.

[7] S Cazaux, J-B Bossa, H Linnartz, and AGGM Tielens. Pore evolution in interstellar ice analogues-simulating the effects of temperature increase. *Astronomy & Astrophysics*, 573:A16, 2015.

[8] Sushil K Atreya, Mark H Hofstadter, Joong Hyun In, Olivier Mousis, Kim Reh, and Michael H Wong. Deep atmosphere composition, structure, origin, and exploration, with particular focus on critical in situ science at the icy giants. *Space Science Reviews*, 216(1):18, 2020.

[9] Marco Minissale. *Physics and chemistry on the surface of interstellar dust grains: the effect of O-atom diffusion and chemical desorption on the HCNO reaction network*. PhD thesis, 2014.

[10] Martin Rubin, Kathrin Altwegg, Hans Balsiger, Akiva Bar-Nun, Jean-Jacques Berthelier, Christelle Briois, Ursina Calmonte, Michael Combi, Johan De Keyser, Björn Fiethe, et al. Krypton isotopes and noble gas abundances in the coma of comet 67p/churyumov-gerasimenko. *Science advances*, 4(7):eaar6297, 2018.

[11] Olivier Mousis, Yann Alibert, Daniel Hestroffer, Ulysse Marboeuf, Christophe Dumas, Benoit Carry, Jonathan Horner, and Franck Selsis. Origin of volatiles in the main belt. *Monthly Notices of the Royal Astronomical Society*, 383(3):1269–1280, 2008.

[12] Katharina Lodders. Solar system abundances and condensation temperatures of the elements. *The Astrophysical Journal*, 591(2):1220, 2003.

[13] Takuya Matsuda, Humitaka Satō, and Hidenori Takeda. Cooling of pre-galactic gas clouds by hydrogen molecule. *Progress of Theoretical Physics*, 42(2):219–233, 1969.

[14] Frank H Shu, Fred C Adams, and Susana Lizano. Star formation in molecular clouds: observation and theory. *Annual review of astronomy and astrophysics*, 25(1):23–81, 1987.

[15] J. Liessauer and I. de Pater. *Fundamental Planetary Science.* Cambridge University Press, 2013.

[16] RK Friesen, J Di Francesco, PC Myers, A Belloche, Yancy L Shirley, TL Bourke, and P André. The initial conditions of clustered star formation. iii. the deuterium fractionation of the ophiuchus b2 core. *The Astrophysical Journal*, 718(2):666, 2010.

[17] N. Monga and S. Desch. External photoevaporation of the solar nebula: Jupiter's noble gas enrichments. 2015.

[18] James B Pollack, Olenka Hubickyj, Peter Bodenheimer, Jack J Lissauer, Morris Podolak, and Yuval Greenzweig. Formation of the giant planets by concurrent accretion of solids and gas. *icarus*, 124(1):62–85, 1996.

[19] T. Guillot and R. Hueso. The composition of jupiter: sign of a (relatively) late formation in a chemically evolved protosolar disc. *Monthly Notices of the Royal Astronomical Society: Letters*, 367:L47–L51, 2006.

[20] Gregory Laughlin, Adriane Steinacker, and Fred C Adams. Type i planetary migration with mhd turbulence. *The Astrophysical Journal*, 608(1):489, 2004.

[21] Jack J Lissauer. Timescales for planetary accretion and the structure of the protoplanetary disk. *Icarus*, 69(2):249–265, 1987.

[22] Chris W Ormel. An atmospheric structure equation for grain growth. *The Astrophysical Journal Letters*, 789(1):L18, 2014.

[23] Michiel Lambrechts, Anders Johansen, and Alessandro Morbidelli. Separating gas-giant and ice-giant planets by halting pebble accretion. *Astronomy & Astrophysics*, 572:A35, 2014.

[24] Katharina Lodders. The solar argon abundance. *The Astrophysical Journal*, 674(1):607, 2008.

[25] T Kleine, Klaus Mezger, C Münker, H Palme, and A Bischoff. 182hf-182w isotope systematics of chondrites, eucrites, and martian meteorites: Chronology of core formation and early mantle differentiation in vesta and mars. *Geochimica et Cosmochimica Acta*, 68(13):2935–2946, 2004.

[26] PR Mahaffy, HB Niemann, A Alpert, SK Atreya, J Demick, TM Donahue, DN Harpold, and TC Owen. Noble gas abundance and isotope ratios in the atmosphere of jupiter from the galileo probe mass spectrometer. *Journal of Geophysical Research: Planets*, 105(E6):15061–15071, 2000.

[27] MS Roulston and DJ Stevenson. Prediction of neon depletion in jupiter's atmosphere. *Eos*, 76:343, 1995.

[28] Nigel J Mason, Anita Dawes, Philip D Holtom, Robin J Mukerji, Michael P Davis, Bhalamurugan Sivaraman, Ralf I Kaiser, Søren V Hoffmann, and David A Shaw. Vuv spectroscopy and photo-processing of astrochemical ices: an experimental study. *Faraday discussions*, 133:311–329, 2006.

[29] Tobias Owen, Paul Mahaffy, HB Niemann, Sushil Atreya, Thomas Donahue, Akiva Bar-Nun, and Imke de Pater. A low-temperature origin for the planetesimals that formed jupiter. *Nature*, 402(6759):269, 1999.

[30] Bertram Bitsch, Alessandro Morbidelli, Anders Johansen, Elena Lega, Michiel Lambrechts, and Aurélien Crida. Pebble-isolation mass: Scaling law and implications for the formation of super-earths and gas giants. *Astronomy & Astrophysics*, 612:A30, 2018.

[31] David Blake, Louis Allamandola, Scott Sandford, Doug Hudgins, and Friedemann Freund. Clathrate hydrate formation in amorphous cometary ice analogs in vacuo. *Science*, 254(5031):548–551, 1991.

[32] C Thomas, O Mousis, V Ballenegger, and S Picaud. Clathrate hydrates as a sink of noble gases in titan's atmosphere. *Astronomy & Astrophysics*, 474(2):L17–L20, 2007.

[33] Tobias Owen, Akiva Bar-Nun, and Idit Kleinfeld. Possible cometary origin of heavy noble gases in the atmospheres of venus, earth and mars. *Nature*, 358(6381):43, 1992.

[34] MÁ Satorre, M Domingo, C Millán, R Luna, R Vilaplana, and C Santonja. Density of ch4, n2 and co2 ices at different temperatures of deposition. *Planetary and Space Science*, 56(13):1748–1752, 2008.

[35] Guillermo M Muñoz Caro and Rafael Escribano. *Laboratory Astrophysics*, volume 451. Springer, 2018.

[36] Jean-Baptiste Bossa, Belén Maté, Coen Fransen, Stéphanie Cazaux, Sergio Pilling, Will Robson Monteiro Rocha, Juan Ortigoso, and Harold Linnartz. Porosity and band-strength measurements of multi-phase composite ices. *The Astrophysical Journal*, 814(1):47, 2015.

[37] G Notesco, D Laufer, A Bar-Nun, and T Owen. An experimental study of the isotopic enrichment in ar, kr, and xe when trapped in water ice. *Icarus*, 142(1):298–300, 1999.

[38] Ronen Jacovi and Akiva Bar-Nun. Removal of titan's noble gases by their trapping in its haze. *Icarus*, 196(1):302–304, 2008.

[39] Vijay K Veeraghattam, Katie Manrodt, Steven P Lewis, and PC Stancil. The sticking of atomic hydrogen on amorphous water ice. *The Astrophysical Journal*, 790(1):4, 2014.

[40] Valentine Wakelam, Emeric Bron, Stephanie Cazaux, Francois Dulieu, Cécile Gry, Pierre Guillard, Emilie Habart, Liv Hornekær, Sabine Morisset, Gunnar Nyman, et al. H2 formation on interstellar dust grains: The viewpoints of theory, experiments, models and observations. *Molecular Astrophysics*, 9:1–36, 2017.

[41] Jiao He, SM Emtiaz, and Gianfranco Vidali. Measurements of diffusion of volatiles in amorphous solid water: application to interstellar medium environments. *The Astrophysical Journal*, 863(2):156, 2018.

[42] Ramón Luna, Ramón Luna-Ferrándiz, Carlos Millán, Manuel Domingo, Guillermo M Muñoz Caro, Carmina Santonja, and Miguel Á Satorre. A fast, direct procedure to estimate the desorption energy for various molecular ices of astrophysical interest. *The Astrophysical Journal*, 842(1):51, 2017.

[43] Helen J Fraser, Mark P Collings, Martin RS McCoustra, and David A Williams. Thermal desorption of water ice in the interstellar medium. *Monthly Notices of the Royal Astronomical Society*, 327(4):1165–1172, 2001.

[44] Miwa Goto, Jeffrey D Bailey, Seyit Hocuk, Paola Caselli, Gisela B Esplugues, Stephanie Cazaux, and Marco Spaans. The first frost in the pipe nebula. *Astronomy & Astrophysics*, 610:A9, 2018.

[45] Akiva Bar-Nun, Idit Kleinfeld, and E Kochavi. Trapping of gas mixtures by amorphous water ice. *Physical Review B*, 38(11):7749, 1988.

[46] Takayuki Tanigawa and Masahiro Ikoma. A systematic study of the final masses of gas giant planets. *The Astrophysical Journal*, 667(1):557, 2007.

[47] Olivier Mousis, Artyom Aguichine, David H Atkinson, Sushil K Atreya, Thibault Cavalié, Jonathan I Lunine, Kathy E Mandt, and Thomas Ronnet. Key atmospheric signatures for identifying the source reservoirs of volatiles in uranus and neptune. *Space Science Reviews*, 216(5):1–19, 2020.

[48] E Dendy Sloan and Carolyn A Koh. Clathrate hydrates of natural gases third edition. *CHEMICAL INDUSTRIES-NEW YORK THEN BOCA RATON-MARCEL DEKKER THEN CRC PRESS-*, 119, 2008.

[49] Jyotirmoy Ghosh, Rabin Rajan J Methikkalam, Radha Gobinda Bhuin, Gopi Ragupathy, Nilesh Choudhary, Rajnish Kumar, and Thalappil Pradeep. Clathrate hydrates in interstellar environment. *Proceedings of the National Academy of Sciences*, 116(5):1526–1531, 2019.

[50] Jyotirmoy Ghosh, Rabin Rajan J Methikkalam, Radha Gobinda Bhuin, Gopi Ragupathy, Nilesh Choudhary, Rajnish Kumar, and Thalappil Pradeep. Reply to choukroun et al.: Ir and tpd data suggest the formation of clathrate hydrates in laboratory experiments simulating ism. *Proceedings of the National Academy of Sciences*, 116(29):14409–14410, 2019.

[51] Robin T Garrod. Three-dimensional, off-lattice monte carlo kinetics simulations of interstellar grain chemistry and ice structure. *The Astrophysical Journal*, 778(2):158, 2013.

[52] K Acharyya, GW Fuchs, HJ Fraser, EF Van Dishoeck, and H Linnartz. Desorption of co and o2 interstellar ice analogs. *Astronomy & Astrophysics*, 466(3):1005–1012, 2007.